

CONSTRUCTION MATERIAL MONITORING WITH «OPTICAL HAIR» HYGROMETERS

THÈSE N° 2673 (2002)

PRÉSENTÉE À LA FACULTÉ ENVIRONNEMENT NATUREL, ARCHITECTURAL ET CONSTRUIT

SECTION DE GÉNIE CIVIL

ÉCOLE POLYTECHNIQUE FÉDÉRALE DE LAUSANNE

POUR L'OBTENTION DU GRADE DE DOCTEUR ÈS SCIENCES TECHNIQUES

PAR

Pascal KRONENBERG

ingénieur civil diplômé EPF
de nationalité suisse et originaire de Horw (LU) et Lucerne

acceptée sur proposition du jury:

Prof. I. Smith, directeur de thèse
Prof. B. Culshaw, rapporteur
Dr D. Inaudi, rapporteur
Dr H. G. Limberger, rapporteur
Dr P. Rastogi, rapporteur
Prof. K. Scrivener, rapporteur

Lausanne, EPFL
2003

Outline

Acknowledgments	iii
Abstract.....	v
Version abrégée.....	vi
Zusammenfassung.....	vii
Riassunto.....	viii
Table of contents	ix
1. Introduction.....	1
2. State of the art	7
3. Sensor behaviour models.....	27
4. Sensor designs and characterisation	61
5. Moisture monitoring in construction materials	97
6. Future work.....	105
7. Conclusions.....	109
References.....	111
Annexe.....	117
Notations	119
Curriculum Vitae	121

Acknowledgments

The research presented in this thesis would not have been possible without the contributions of many people. I would especially like to express my gratitude to Prof. Ian Smith who gave me the opportunity to do this research, to Dr Pramod Rastogi for his encouragements and great faith in this work and to Dr Daniele Inaudi (Smartec SA) for having introduced me in fibre optic sensing technology and for his perceptive comments on various practical aspects of the sensors. My sincere gratitude goes to the former head of the IMAC laboratory, Prof. Leopold Pflug, for his unconditional faith in the potential of fibre optic monitoring in civil engineering and for his kind words at the public presentation.

I would like to express my sincere gratitude to Dr Hans Limberger and Dr Philippe Giaccari from the Laboratory of Applied Optics (IOA) at EPFL for the uncountable constructive discussions we had. A particular thank to Philippe Giaccari for the fabrication of the fibre Bragg gratings and for having helped in the post-processing of the measurement data and in the MATLAB-implementation of the diffusion model. IOA also kindly lent us the tunable laser demodulation system and the fibre recoater.

My thanks go to Prof. Karen Scrivener (LMC / EPFL) for having accepted to judge this work from a material scientific point of view, and to Prof. Brian Culshaw (Optoelectronics laboratory, University of Strathclyde) for having given me the opportunity to spend an extraordinary year abroad in his laboratory at the University of Strathclyde and for having agreed to take part in the jury.

I would like to express my gratitude to Prof. Eugen Brühwiler (MCS / EPFL) for his earlier advice on the orientation of this thesis and for his encouragement to focus, regarding moisture profile monitoring, on short gauge sensors, and to Dr Samuel Vurpillot (DeCérenville Géotéchnique) for his constructive comments on the application part. My thanks also go to Dr Blaise Rebora (LSC / EPFL) for his assistance in the development of the three-dimensional mechanical model, to Dr Yanzhou Zhou (IMAC / EPFL) for his contribution to the MATLAB-implementation of the cylindrical diffusion model, and to Dr Benny Raphael (IMAC / EPFL) for the coding of various data processing routines.

My thanks go to Giancarlo Tirabassi (Rotronic SA) for lending us the reference RH / T gauges and for his interest in this work, and to Dr Giovanni Martinola (IBWK / ETHZ) who provided us with testing equipment for the mortar desiccation experiment.

Special thanks go to Dr Hans Limberger, Dr Pramod Rastogi, Dr Pierino Lestuzzi and Prof. Ian Smith for their critical feedback on this thesis, and to Prakash Mathur and Tim Schumacher for their proof reading. I would also like to thank Prakash Mathur

for his contribution in the experimental part and I wish him well for his own PhD thesis.

J'aimerais remercier tous les (ex-)IMACiens et -iennes qui ont apporté des coups de mains à la réalisation de ce travail et qui ont contribué par leur présence à l'ambiance chaleureuse et familiale de l'IMAC. Je tiens tout particulièrement à remercier Dr Etienne Fest, mon colocataire du bureau G0 567 (mieux connu comme « NASA Research Lab »), qui était toujours prêt à donner son avis critique sur mes inspirations et qui m'a aidé plus qu'une fois à « dégermaniser » mon français. Je tiens à remercier Dr Samuel Vurpillot pour m'avoir initié à la surveillance des ouvrages par fibre optique et pour sa compagnie agréable lors des nombreuses expéditions proches et lointaines. J'aimerais exprimer ma reconnaissance à Dr Branko Glisic, Dr Michel Cherbuliez, Yvan Robert-Nicoud, Bernd Dömer, Francine Laferrière et Marco Viviani pour leur serviabilité et leur amitié.

J'aimerais remercier les mécaniciens Raymond Délez, Manuel Pascual et Patrice Gallay pour leur serviabilité quand il fallait « vite fabriquer une petite pièce », Alain Herzog pour ses clichés sublimes (et surtout pour avoir réussi à me transformer en pin-up EPFLien...) et Jean-Louis Guignard pour ses conseils graphiques. Je tiens à remercier Charles Gilliard pour ses conseils électro-informatiques compétents et sa serviabilité en tout moment.

Schliesslich möchte ich meinen Eltern danken, dass sie mich stets ermutigt haben, meinen Weg zu gehen und mir dabei immer unterstützend zur Seite standen.

E ultima, ma non meno importante, voglio ringraziare il mio amore Lilly per la traduzione del riassunto e, soprattutto, per essermi stata vicina nei momenti felici e meno felici.

Abstract

Moisture is an essential parameter in the behaviour of capillary-porous construction materials such as timber and concrete. It affects liquid and gas transport phenomena, chemical and biological degradation processes, mechanical properties and, in the case of concrete, hydration. From a scientific point of view, moisture monitoring is essential in order to improve the understanding of material behaviour. Moisture measurements may increase the predictive accuracy of established material behaviour models. In practice, the increased knowledge of material behaviour improves structural maintenance planning.

The main objective of this work is to propose a measurement method for non-destructive, in-depth moisture monitoring of construction materials. In this context, an intrinsic point and an averaging fibre optic relative humidity sensor have been developed and tested. The sensors are based on optical fibres that are coated with a hygroscopically swelling transducer polymer. When wet, the swelling of the coating strains the fibre (analogy with the hair hygrometer). The induced strain is assessed with conventional fibre optic strain sensing techniques such as fibre Bragg gratings and Michelson interferometry.

Theoretical and experimental studies lead to a detailed understanding of the influence of humidity and temperature on the steady and transient state sensor behaviour. The sensors have an accurate, linear, reversible and reproducible response to relative humidity between 5 and 95 %RH and between 13 and 60 °C, at least. The sensor response time is in the order of 20 minutes. However, when packaged, the sensor responds slower. The temperature cross-sensitivity of the fibre Bragg grating sensor may be compensated with an additional non-hygroscopic grating, while the Michelson interferometric sensor provides an auto-compensation of temperature effects.

Tests in mortar and timber samples demonstrate that the sensors preserve their sensing ability when embedded. These tests have also clarified the multiplexing potential of fibre Bragg gratings for forming a multi-point RH sensor. Multi-point sensors are particularly useful for profile measurements.

Keywords: construction material, moisture, humidity, monitoring, measurement, fibre optic, sensor, Bragg grating, SOFO.

Version abrégée

Le comportement des matériaux de construction capillaire-poreux, tels le bois et le béton, est très sensible à leur teneur en eau. Les phénomènes de transport des gaz et des liquides, les processus de dégradation chimique et biologique, les propriétés mécaniques et, dans le cas du béton, l'hydratation, sont principalement concernés. De fait, la mesure de la teneur en eau permet de mieux comprendre le comportement de ces matériaux. Les prédictions des modèles peuvent être améliorées en intégrant la teneur en eau comme paramètre connu. En pratique, le comportement à long terme d'une structure est plus prévisible et contribue ainsi à une meilleure planification de la maintenance structurale.

L'objectif principal de ce travail est de proposer une méthode de mesure non-destructive permettant de surveiller en continu la teneur en eau au sein des matériaux. Dans ce contexte, deux capteurs d'humidité relative à fibre optique ont été développés et testés, l'un étant un capteur « point » et l'autre un capteur « moyennant », à base de mesure longue. Les capteurs dépendent d'une fibre optique enrobée d'un polymère transducteur hygroscopique. Au contact de l'eau, ce polymère gonfle et étire ainsi la fibre (analogie de l'hygromètre à cheveux). La déformation de la fibre est ensuite analysée par des techniques classiques de mesure de déformation par fibre optique, tels que les réseaux de Bragg ou l'interférométrie Michelson.

Une étude théorique et expérimentale a permis d'acquérir une connaissance détaillée de l'influence de l'humidité et de la température sur le comportement stationnaire et transitoire des capteurs. La réponse des capteurs à une humidité relative variant de 5 à 95 %HR est précise, linéaire, réversible et reproductible pour une température comprise entre 13 et 60 °C au moins. Le temps de réponse est de l'ordre de grandeur de la vingtaine de minutes. Cependant, le conditionnement du capteur dans un emballage protecteur tend à prolonger son temps de réponse. La sensibilité à la température du capteur à réseau de Bragg peut être compensé moyennant un réseau supplémentaire non-hygroscopique, alors que le capteur Michelson peut autocompenser les effets de température.

Des essais dans le mortier et dans le bois ont montré que les capteurs préservent leur habilité de mesure quand ils sont placés au sein du matériau. Ces essais ont aussi confirmé que les capteurs à réseau de Bragg peuvent facilement être multiplexés pour former un capteur d'humidité multi-point. Ce dernier est idéal pour la mesure d'un profil d'humidité.

Mots clés: matériaux de construction, teneur en eau, humidité, mesure, fibre optique, capteur, réseau de Bragg, SOFO.

Zusammenfassung

Das Verhalten kapillar-poröser Baustoffe wie Holz und Beton hängt in bedeutendem Masse von deren Feuchtegehalt ab. Dieser beeinflusst Gas- und Flüssigkeitstransport, chemische und biologische Zerfallprozesse, mechanische Eigenschaften und, im Fall von Beton, die Hydratation. Für ein besseres Verständnis des Baustoffverhaltens ist die Überwachung der Feuchte notwendig. Feuchtemessungen ermöglichen auch, die Vorhersagegenauigkeit von Materialmodellen zu steigern. In der Praxis erlaubt die bessere Kenntnis des Baustoffverhaltens die Planung von Bauwerksunterhaltungsmassnahmen zu optimieren.

Ziel dieser Arbeit ist, eine Messmethode zur zerstörungsfreien und tiefenauflösenden Baustofffeuchteüberwachung zu entwerfen. Diesbezüglich wurden zwei intrinsische faseroptische relative Feuchtigkeits-Sensortypen entwickelt und getestet. Der eine Sensortyp eignet sich für Punktmessungen, während der andere über die Messdistanz gemittelte Messungen ermöglicht. Die Sensoren bestehen aus einer optischen Faser, die in einer hygroskopisch anschwellenden Polymer-Ummantelung eingefasst ist. Bei Wasserkontakt schwillt die Ummantelung und dehnt die Faser (Analogie mit Haarhygrometer). Diese Dehnung kann mit herkömmlichen faseroptischen Dehnungsmesstechniken wie Bragg Gitter (Punktsensor) oder Michelson Interferometer (mittlerer Sensor) erfasst werden.

Theoretische und experimentelle Untersuchungen führten zu einem detaillierten Verständnis des Einflusses von Feuchtigkeit und Temperatur auf das stationäre und dynamische Sensorantwortverhalten. Die Sensoren zeichnen sich durch eine genaue, lineare, umkehrbare und reproduzierbare Antwort auf relative Feuchtigkeiten zwischen 5 und 95 %rF bei Temperaturen zwischen mindestens 13 und 60 °C aus. Die Zeitkonstante der Sensorfasern liegt im Bereich von 20 Minuten. Die Sensorhülle, welche unter gewissen Umständen zur mechanischen Abschirmung der Fasern vom Baustoff benötigt wird, erhöht die Zeitkonstante. Die Temperaturabhängigkeit des Bragg Gitter Sensors kann mit einem zusätzlichen nicht-hygroskopischen Gitter kompensiert werden, während der Michelson interferometrische Sensor eine Autokompensation der Temperatur ermöglicht.

Messversuche in Mörtel- und Holzproben haben gezeigt, dass die eingebetteten Sensoren ihre Messfähigkeit beibehalten. Ferner wurde das Multiplexingpotential der Bragg Gitter zur Bildung eines Mehrpunkt-Feuchtigkeitssensors bestätigt. Mehrpunktsensoren eignen sich hervorragend für Profilmessungen.

Schlüsselwörter: Baustoff, Feuchte, Feuchtigkeit, Überwachung, Messung, optische Faser, Sensor, Bragg Gitter, SOFO.

Riassunto

Il tenore d'acqua è un parametro essenziale nei materiali da costruzione capillaro-porosi quali il legno ed il calcestruzzo. Esso influisce sui fenomeni di trasporto di gas e di liquidi, sui processi di degradazione chimica e biologica e, nel caso del calcestruzzo, sull'idratazione. Da un punto di vista scientifico, il controllo del tenore d'acqua è essenziale al fine di comprendere il comportamento di tali materiali. Il valore predittivo dei modelli di comportamento esistenti può significativamente migliorare qualora il tenore d'acqua sia inserito come parametro noto. In pratica, una maggiore conoscenza del comportamento del materiale contribuisce ad una migliore pianificazione della manutenzione della struttura.

Lo scopo principale di questo lavoro è di proporre un metodo di misura non-distruttivo, in grado di monitorare in continuo il tenore d'acqua all'interno dei materiali. In tale contesto due sensori d'umidità relativa, basati sulla tecnologia delle fibre ottiche, sono stati concepiti, sviluppati e testati. Il primo sensore è progettato per rilevare puntualmente l'umidità, mentre il secondo è concepito per monitorare ampie zone nel materiale. Entrambi i sensori si basano su di un polimero-trasduttore igroscopico che ricopre una fibra ottica. A contatto con l'acqua tale polimero si espande, allungando la fibra (analogia con l'igrometro a capelli). Poiché il trasduttore è installato sulla fibra ottica appartenente ad un sensore di deformazione di tipo Bragg o Michelson, le deformazioni provocate dall'espansione sono misurabili e registrabili in continuo.

Studi teorici e sperimentali hanno portato ad una conoscenza dettagliata dell'influenza dell'umidità e della temperatura sul comportamento stazionario e transitorio dei sensori. La risposta dei sensori ad un tasso d'umidità relativa che va dal 5 al 95 %UR è precisa, lineare, reversibile e riproducibile, per l'intervallo di temperatura studiato durante lo svolgimento della ricerca (13-60 °C). Il tempo di risposta è all'incirca di venti minuti, con tendenza ad aumentare qualora il sensore, per usi specifici, sia protetto da un rivestimento. La sensibilità alla temperatura del sensore basato sulla tecnologia dei reticoli di Bragg, può essere compensata accoppiando al sensore d'umidità un secondo reticolo che non abbia il trasduttore igroscopico. I sensori di tipo Michelson essendo auto-compensati per gli effetti della temperatura non presentano problemi di sensibilità termica.

Test condotti su malta e legno hanno dimostrato che i sensori conservano la loro capacità di misura una volta inseriti nel materiale. Tali test hanno mostrato che i sensori a reticolo di Bragg si prestano alla realizzazione di sensori "multi-punto", particolarmente adatti alle misure di un profilo d'umidità.

Parole chiave: materiali da costruzione, tenore d'acqua, umidità, monitoraggio, fibre ottiche, sensore d'umidità, reticoli di Bragg, SOFO.

Table of contents

1. Introduction	1
1.1 Context	1
1.2 Motivations.....	3
1.3 Objectives	3
1.4 Tasks and contributions	4
1.5 Scope	5
1.6 Structure of work	5
2. State of the art	7
2.1 Introduction	7
2.2 Moisture in construction materials	7
2.2.1 Definition	7
2.2.2 Moisture transport	8
2.2.3 Concrete	9
2.2.4 Timber	11
2.3 Moisture measurement in construction materials.....	13
2.3.1 Destructive testing methods	13
2.3.2 Non-destructive testing methods.....	15
2.4 Fibre optic sensors.....	19
2.4.1 Structural monitoring	19
2.4.2 Fibre optic humidity sensors	21
2.4.3 Fibre optic absorption hygrometer	24
2.5 Concluding remarks	25
3. Sensor behaviour models	27
3.1 Introduction	27
3.2 Strain and temperature dependence of a bare optical fibre	27
3.3 Steady state behaviour of the coated optical fibre.....	31
3.3.1 Optical response	31
3.3.2 Mechanical behaviour	33
3.3.2.1 Analytical 1-D model.....	33
3.3.2.2 Analytical 3-D model.....	34
3.3.2.3 Numerical model.....	38
3.3.2.4 Discussion of mechanical models	39
3.3.3 Discussion of optical response	42
3.4 Transient state behaviour of the coated optical fibre.....	45
3.4.1 Plane layer with steady state boundary conditions	45
3.4.2 Cylindrical layer with steady state boundary conditions	47
3.4.3 Cylindrical layer with concentration dependent diffusivity and nonsteady state boundary conditions	48

3.4.4 Discussion of diffusion models.....	52
3.5 Fibre Bragg grating humidity sensor.....	55
3.6 Michelson interferometric fibre optic humidity sensor.....	56
3.7 Concluding remarks	59
4. Sensor designs and characterisation	61
4.1 Requirements.....	61
4.2 Transducer coating	62
4.3 FBG sensor.....	63
4.3.1 Sensor operation and interrogation	63
4.3.2 Sensor design	66
4.3.2.1 Grating fabrication.....	66
4.3.2.2 Recoating	68
4.4 SOFO sensor.....	69
4.4.1 Sensor operation and interrogation	69
4.4.2 Sensor design	71
4.5 Steady state sensor response.....	73
4.5.1 FBG sensor.....	73
4.5.1.1 Experimental setup.....	73
4.5.1.2 Response behaviour	74
4.5.2 SOFO sensor	79
4.5.2.1 Experimental setup.....	79
4.5.2.2 Response behaviour	80
4.6 Transient state sensor response (FBG).....	81
4.6.1 Experimental setup.....	81
4.6.2 Response behaviour	82
4.7 Temperature compensation	86
4.8 Discussion	88
4.9 Sensor packaging.....	91
4.10 Concluding remarks	94
5. Moisture monitoring in construction materials	97
5.1 Mortar hydration.....	97
5.1.1 Experimental setup and sensor installation	97
5.1.2 Measurements and discussion	100
5.2 Water suction in timber	101
5.2.1 Experimental setup and sensor installation	101
5.2.2 Measurements and discussion	103
5.3 Concluding remarks	104
6. Future work	105
6.1 Sensor	105
6.2 Packaging	106
6.3 Applications.....	106

<u>7. Conclusions</u>	<u>109</u>
<u>References</u>	<u>111</u>
<u>Annexe</u>	<u>117</u>
<u>Notations</u>	<u>119</u>

1. Introduction

1.1 Context

It is recognised within the construction community that quantitative monitoring may increase the knowledge of the real behaviour of structures. From a scientific point of view, monitoring is essential in order to understand the mechanical and physico-chemical processes occurring in structures and their materials. If a new behaviour model is proposed, comparison of the theoretical behaviour with experimentally assessed data is necessary to validate the model. Even well established models require measured values of input parameters on which their calculations depend in order to make reliable behaviour predictions. Recently, increasingly complex behaviour models have been developed, often using approaches which combine chemical, physical and mechanical processes. They are based on a large number of parameters, which may vary as a function of their position in the material and evolve over time. Such models may model very accurately the processes involved, but they may also, if some of the input parameters are inaccurate, lead to less accurate predictions (see Figure 1.1). It is only by having more measurement data available to fit the model onto that the potential of more complex models can be exploited [1].

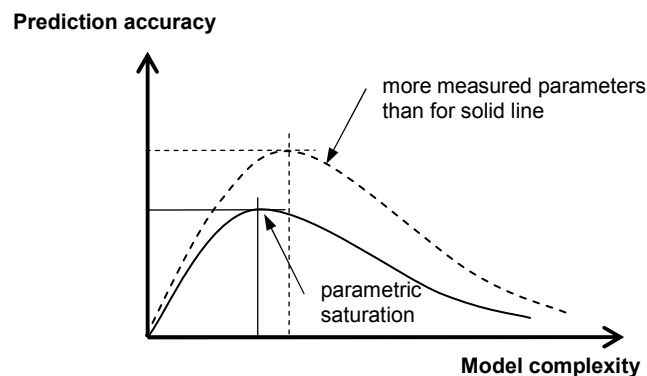


Figure 1.1 The solid curve schemes the prediction accuracy as a function of the complexity of a behaviour model for a given number of measured parameters. Increasing the model complexity beyond the parametric saturation point leads to a decrease in the prediction accuracy. The dashed curve shows the same relationship with more measured parameters. In this second situation more complex models can improve the prediction accuracy (from [1]).

From a practical point of view, the knowledge of the real behaviour of structures and their materials supports structural maintenance. Having a detailed and continuous

image of the structure's health state, repair works can be performed when and where they are appropriate. Furthermore, the risk of discovering structural damage at a late stage, when either repair is no longer possible or costs are excessive, is reduced. The principal goal of structural monitoring is to reduce, despite additional costs of monitoring, the life-cycle cost of a structure. Other uses of monitoring are secondary to this goal. For example, few structures need to be monitored as part of a collapse warning system. Comparing the overall maintenance costs (including indirect costs to the user due to restricted usability of the structure during repair works) with the costs of a monitoring system, the money saved by even a small improvement in maintenance efficiency usually compensates for the added cost of monitoring. Despite this, it remains a difficult task to convince owners of structures to invest in monitoring. The costs of a monitoring system generally occur immediately at construction (sensor acquisition and installation), while the potential savings are gradually accumulated over the structure's life-span. This delay in return-on-investment, combined with the short-term perspectives that are common to owners and operators, may explain such behaviour.

Monitoring of a structure can be grouped into three categories [2]: macro-, meso- and microlevel monitoring. Macrolevel monitoring investigates the global movements of the entire structure as to external references. Typical phenomena assessed are sway movements, thermally induced movements and movements due to load, creep and foundation settlements. Mesolevel monitoring assesses relative movements and deformations of structural components and foundations, and microlevel monitoring determines local phenomena in construction materials, such as stresses, cracking, and physico-chemical parameters. Macro- and mesolevel monitoring measure geometrical properties on a structural scale. Therefore, they may be referred to as structural monitoring. Microlevel monitoring focuses on local, mainly material related phenomena and thus may be referred to as material monitoring.

Especially for health monitoring, material monitoring constitutes an important complement to structural monitoring. As signs of structural degradation often only are symptoms of a failure on material level, structural monitoring is able to indicate that something is wrong but it will not reveal the phenomenon which is at the origin of this irregularity. Here material monitoring can provide more detailed information about the health state of the construction material, allowing the engineer responsible for the maintenance to better identify the real causes of the degradation and intervene appropriately. In many cases (i.e., when slowly progressing chemical or biological degradation processes are involved, such as rebar corrosion, carbonation and alkali-silica reactions in concrete or biodegradation of timber), material monitoring makes it even possible to identify harmful processes months if not years before first signs of structural degradation would appear. This early warning can help to optimise

maintenance interventions such as to prevent the structure from structural degradation before it even starts.

This work is concerned with non-destructive monitoring of humidity in porous construction materials, such as timber and concrete. In these materials, humidity is a parameter which influences many durability and mechanical performance related phenomena. In timber, humidity is known to affect durability as well as mechanical and geometrical properties. In concrete, many degradation phenomena such as cracking due to drying shrinkage, depassivation, rebar corrosion, carbonation, alkali-silica reactions and freeze-thaw damage depend on humidity, even if the presence of water does not directly impair the concrete's performance and durability.

1.2 Motivations

This work is motivated by several factors:

- a) Need to improve the understanding of the influence of humidity on mechanical properties and on chemical and biological degradation processes in construction materials.
- b) Emergence of increasingly complex material behaviour models, requiring the measurement of additional parameters, such as humidity, to justify exploitation of their enhanced potential.
- c) Need to identify as early as possible forthcoming structural degradation in order to optimise maintenance plans.
- d) Gaps in application of fibre optic sensing technology for in-situ humidity monitoring of construction materials.

Items a) and b) are material science related motivations, c) is a practical civil engineering based motivation, and motivation d) is influenced by metrology.

1.3 Objectives

The principal objective of this thesis is to assist in the understanding of the real behaviour of capillary-porous construction materials by proposing a reliable measurement method for non-destructive in-depth moisture monitoring. This objective includes

- Proposal of a short and a long gauge sensor design that complies with non-destructive in-depth moisture monitoring of construction materials,
- Theoretical study of the steady and transient state response behaviours of the sensors,
- Experimental evaluation of the sensor response in a controlled environment,
- Investigation of the sensor behaviour when embedded in construction materials.

1.4 Tasks and contributions

The following tasks have been carried out:

- Critical evaluation of existing moisture assessment methods for construction materials and fibre optic humidity sensors.
- Sensor design
- Modelling of sensor behaviour
- Experimental tests under controlled climate.
- Embedding of the sensor in mortar and timber, followed by measurements to demonstrate feasibility.

The successful completion of these tasks has led to the following contributions:

- Insight into the interaction of humidity with the steady and transient state behaviour of the sensor and its components (i.e., optical fibre, hygroscopic transducer coating, sensor packaging).
- Realisation of a short and a long gauge sensor, using established fibre optic sensing techniques (Bragg gratings for short gauge, Michelson interferometer for long gauge).
- Understanding of temperature cross-sensitivity and proposition of compensation methods.
- Proposition of a point multiplexed sensor for profile measurements.
- Demonstration of the sensor's operation when embedded in material used in construction.

This work has an interdisciplinary character, incorporating elements from fields such as material science, mechanics, optics and polymer physics.

1.5 Scope

The scientific scope of this work is to support advances in the understanding of humidity related processes in construction materials by offering a convenient and versatile tool for humidity monitoring. Humidity measurements may be used as additional control tests to determine validity of complex material behaviour models.

From a practical point of view, this work aims to contribute to the field of non-destructive structural health monitoring. Since fibre optic sensor systems are already successfully implemented for structural deformation and temperature monitoring, the proposed humidity sensor may easily be integrated into existing sensor networks.

1.6 Structure of work

This work is divided into five parts:

- Chapter 2: Review of the influence of moisture on the behaviour of concrete and timber. Evaluation of moisture assessment methods and existing fibre optic humidity sensors. Revelation of the originality of this work.
- Chapters 3 + 4: Theoretical and experimental investigation of a point and a long gauge fibre optic relative humidity sensor.
- Chapter 5: Moisture measurement experiments in two common construction materials.
- Chapters 6: Future work
- Chapters 7: Conclusions

2. State of the art

2.1 Introduction

Moisture is an essential parameter in capillary-porous construction materials, such as concrete and timber. It affects mechanical properties, most material degradation processes and, for concrete, the curing behaviour. For these materials, moisture may be considered as the parameter with the most wide ranging influence on various phenomena, processes and characteristics.

2.2 Moisture in construction materials

2.2.1 Definition

Moisture is the physically bound and the free water in construction materials. Chemically and physical-chemically bound water is not considered. Moisture can be quantified by means of the moisture content, ρ_w ,

$$\rho_w = \frac{m_w}{V} \quad [\text{kg/m}^3], \quad (2.1)$$

which is defined as the mass of the evaporatable water, m_w , per volume of material, V . Often, the moisture content is expressed as the weight percentage of water per dry material,

$$u = \frac{m_w}{m_{m0}} 100 \quad [\text{wt}\%], \quad (2.2)$$

where $m_{m0} = V\rho_{m0}$ is the mass of the volume of dry material and ρ_{m0} is the specific weight of dry material.

The moisture content may also be expressed as a function of the relative humidity in material voids (e.g., air filled pores). Relative humidity, RH , is the percentage of partial vapour pressure, p , per water saturation pressure at equal temperature, p_0 ,

$$RH = \frac{p}{p_0} 100 \quad [\%RH]. \quad (2.3)$$

Porous materials sorb or desorb water from the surrounding air so as to be in equilibrium with the air humidity. Sorption and desorption processes are controlled by the sorption isotherms, which are material and temperature dependent. Beyond the hygroscopic range of a material, $RH = 100\%RH$.

The moisture content, u , remains the universal parameter to quantify moisture in construction materials. However, Nilsson [3] suggested using relative humidity instead of moisture content to characterise moisture in concrete, because relative humidity expresses in a far better way the state of moisture. And it is the state of moisture which is of interest in most cases.

2.2.2 Moisture transport

Moisture transport in porous-capillary construction materials takes place as [4]

- Capillary suction of liquid water in air-filled pores with the surface tension as driving force, which is expressed as

$$\frac{m_w}{A} = K\sqrt{t}, \quad (2.4)$$

where A is the wet surface area of the volume of material containing the mass of capillary sucked water, m_w . K is the capillary sorption coefficient and t is the exposure time to water of the initially dry material. K depends on the surface tension of water in the capillaries.

- Water vapour diffusion in air-filled pores with the vapour pressure gradient as driving force, which is expressed with Fick's 2nd law,

$$\frac{\partial u}{\partial t} = \nabla(D(u)\nabla u), \quad (2.5)$$

where $D(u)$ is the moisture dependent diffusivity. The moisture flux (i.e., the flow rate per unit area at which moisture moves) is a function of moisture gradient and diffusivity.

- Permeation of liquid water in water-filled pores with a pressure gradient as driving force, which is expressed with Darcy's law,

$$v = ki, \quad (2.6)$$

where v is the flow speed of water in a material with a permeability k and subjected to a hydraulic gradient $i = \nabla h$, where h is the hydraulic load.

Capillary suction and vapour diffusion are the most important moisture transport phenomena and normally occur simultaneously.

2.2.3 Concrete

Moisture is introduced into concrete during fabrication and later as a consequence of wet climate (rain, mist, ambient air humidity), standing (waters, ground water level) and sprayed water (traffic, waves).

Moisture transport coefficients of cement paste may depend on several parameters, such as temperature, moisture content, drying or wetting, composition, and age [5][6][7].

Moisture influences concrete curing and most concrete deterioration processes. Even if the sole presence of moisture does not directly impair the mechanical properties of concrete, it is the main parameter controlling physico-chemical processes. Physico-chemical processes in concrete are highly coupled, i.e., the evolution of most processes influences other processes. Modelling of coupled processes requires complex models which depend on a large number of parameters, e.g., [8]. Influencing most individual processes, moisture constitutes an important parameter of multi-process models.

The following properties and processes are considered to depend on moisture [9]:

- Cement hydration rate and porosity of cement paste matrix
- Carbonation rate
- Chloride ingress
- Reinforcing steel corrosion rate
- Freeze-thaw damage
- Alkali-silica reactions

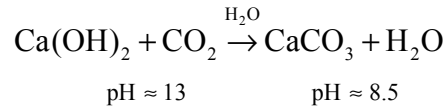
Cement hydration rate and porosity of the cement paste matrix

Cement hydration is the chemical fixation of water to the cement in form of hydrate water and hydroxide. The hydration process is a sequence of chemical reactions, transforming the anhydrous constituents of cement in the presence of water into calcium silicate hydrates (C-S-H gel) and calcium hydroxides ($\text{Ca}(\text{OH})_2$). Under endogenous conditions, the cement paste dries during hydration (chemical binding of water).

Patel et al. [10] have shown, that the hydration rate of an ordinary Portland cement paste decreases as the relative humidity of the curing environment drops below 95 %RH. Below 80 %RH, the hydration rate is very low [11]. Patel et al. also indicated that curing below 80 %RH produces a coarsened porosity of the cement paste matrix.

Carbonation rate

When carbon dioxide diffuses into concrete, it reacts with calcium hydroxide (a cement constituent) to form calcium carbonate. As a result, the alkaline pH of concrete is reduced to below 10 [12].



Once the carbonation front reaches the reinforcement, the steel surface will be depassivated and corrosion can start. Moreover, carbon dioxide reacts with the major components of hydrated cement (aluminates and C-S-H gel) and may even set free chemically bound chloride ions, which on their turn participate to chloride induced reinforcement corrosion.

While the penetration of carbon dioxide in concrete is a gaseous diffusion process and hence requires a relatively dry concrete, the carbonation reaction can only take place in the presence of water. The carbon dioxide penetration rate strongly depends on the moisture level, being higher the dryer the concrete is (i.e., gas diffusivity is moisture dependent, see Figure 2.1). Relative humidity values between approximately 40 and 95 %RH allow for the carbonation to happen.

Chloride ingress

Free chloride ions can weaken the reinforcement corrosion inhibiting properties of the alkaline cement paste pore solution [13]. Chloride ions diffuse in the liquid phase or are transported into concrete by capillary suction. The ion diffusivity depends on the moisture content as illustrated in Figure 2.1. Below 50 %RH ionic diffusion is inhibited while it is highest in water saturated concrete. Alternating humidity conditions (wetting – drying) particularly facilitate chloride penetration.

Reinforcing steel corrosion rate

Reinforcing steel corrosion starts once the steel surface is depassivated. Depassivation is caused by a reduction of the (initially alkaline) pore water pH due to carbonation or when a certain chloride ion threshold concentration is reached. This threshold depends on the concrete composition and on environmental parameters, such as humidity and temperature [14]. The corrosion process requires the presence of an electrolyte (water) and oxygen. For this reason a relative humidity of at least 60 %RH is needed. In absence of oxygen corrosion does not take place.

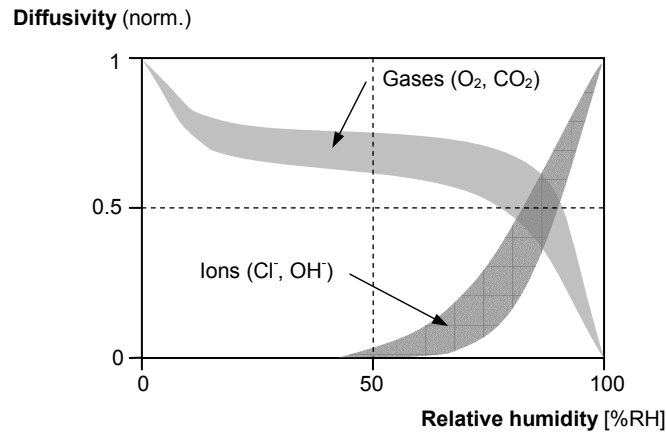


Figure 2.1 Humidity dependence of the gaseous and ionic diffusivity in concrete (from [4]).

Freeze-thaw damage

Freeze-thaw damage is the mechanical deterioration of concrete under the action of cyclic freezing and thawing of capillary water. For frost damage to develop, the capillaries must be saturated to a high degree, with moisture contents usually beyond the hygroscopic range. The hygroscopic range describes moisture contents with $RH < 100\%RH$.

Alkali-silica reaction

Reactive (i.e., partially crystallised) silica (SiO_2) contained in the aggregate can be dissolved by the hydroxide ions of the pore solution. Alkali-silica reaction is the reaction of this dissolved silica with the alkaline and calcium ions of the pore solution. The product of this reaction swells and deteriorates concrete by micro-cracking. The alkali-silica reaction takes only place in humid environments, with relative humidities typically above $80\%RH$ [15].

2.2.4 Timber

Moisture is introduced into timber by hygroscopic absorption of water vapour through the timber cell membranes, by capillary suction in the cell cavities, and by contact with pressurised water. The moisture is due to the inherent presence of water in living wood and due to direct and indirect contact of the timber with climatic (ambient air humidity, mist, and rain), standing (waters, ground water level) and sprayed water (traffic, waves).

Timber being an anisotropic material, moisture transport depends on its direction. Vapour diffusion is predominant in radial and tangential direction, whereas capillary

suction occurs longitudinally, i.e., in the direction of the wood fibres. Capillary moisture transport exhibits the highest rate, followed by tangential diffusion and radial diffusion, which is the slowest. Considering these transport phenomena, two moisture content domains can be defined [16]:

- The **hygroscopic domain**: moisture content inferior to the moisture saturation level of the fibres ($u < 28$ wt%). This moisture is controlled by the ambient air humidity.
- The **capillary domain**: moisture content superior to the moisture saturation level of the fibres ($u > 28$ wt%). In the capillary domain, capillary suction fills the cavities with water.

Moisture influences mechanical as well geometrical properties, and it is a major parameter of biological degradation processes. The following properties and processes are considered to depend on moisture [16]:

Strength

The mechanical strength of timber, mainly in compression, is a function of hygroscopic moisture. For unprotected timber in wet environments, the allowable (compressive) stress must be reduced by up to a third.

Modulus

The elastic modulus of timber decreases as the hygroscopic moisture content increases. The longitudinal elastic modulus of saturated timber is typically 20% inferior to the modulus of dry material.

Swelling and shrinkage

Timber swells proportionally to the hygroscopic moisture content. Swelling occurs predominantly in tangential and radial direction, reaching up to 12% for certain resins. The maximum swelling is reached at fibre saturation. Capillary moisture does not induce additional swelling.

Swelling (and shrinkage) is a major concern for the geometrical compatibility of structural elements. Parasite stresses may appear as a consequence of changing moisture conditions.

Biological degradation

Untreated timber may suffer from fungous attack, which can weaken its mechanical strength. Biological attack usually initiates at moisture contents close to saturation, although some fungi even grow at lower levels.

2.3 Moisture measurement in construction materials

We have seen in 2.2 that moisture is a determining parameter of material properties and degradation processes in concrete and timber. In this context, assessment of the moisture content is an important instrument to improve the understanding of the influence of moisture on these phenomena. Once behaviour models are established, moisture assessment may also aid prediction of degradation processes and evaluation of the health state of structures. Especially complex multi-process models require more measured input parameters in order to make accurate predictions, as illustrated in Figure 1.1. In this context polypotent input parameters such as moisture and temperature are particularly interesting.

A critical review of existing moisture measurement methods for porous construction materials is presented in the following section, classified by their impact on the tested material, i.e., destructive testing (DT) and non-destructive testing (NDT). DT describes testing methods where the host deteriorates mechanically or chemically each time a measurement is made. NDT may be distinguished as invasive and non-invasive. Invasive methods require a sensor to be introduced in the host material while non-invasive methods use sensors which are applied externally. In this work, the term monitoring is used for continuously working measurement systems, where sensors are built into the structure allowing permanent recording of measurands. As a consequence, only NDT methods allow for monitoring.

The present information is compiled from several sources treating moisture measurement in construction materials, such as [17], [18] and [19]. Table 2.1 summarises the methods and their main metrological characteristics.

2.3.1 Destructive testing methods

Gravimetric method

The gravimetric method is the standard destructive testing method for moisture assessment in construction materials. Core samples are extracted from the material, weighed, oven dried and weighed again. The weight difference divided by the dry weight (mass of dry material) is the moisture content, u (as seen in Eq. (2.2)). The drying temperature is chosen such that only physically-capillary bound (i.e., with low binding energy) water escapes (typically 105 °C). Vacuum and convection drying are alternative drying methods. The moisture content obtained with this method is a local value, averaged over the depth of the core.

Strengths and drawbacks

Due to the core extraction, this method deteriorates the integrity of the material and may disturb the natural moisture equilibrium in the material. The gravimetric moisture assessment can not be done in-situ.

The measurement accuracy depends strongly on the moisture loss during the core extraction due to the heating and the evaporation or hygroscopic water absorption during the transport of the sample. When executed carefully, gravimetric methods may achieve an accuracy of ± 0.5 wt%.

Gravimetric methods are neither sensitive to electromagnetic interference nor to corrosive, alkaline and acid environments. Moreover, they do not need calibration.

The gravimetric method is not adapted for either monitoring or for profile measurements.

Chemical method

Chemical methods are appreciated in civil structural testing since the result may be obtained directly on site. Being a destructive testing method (the impact is however less important than for the gravimetric method), a small sample of material (5 to 20 g, depending on the moisture content) is extracted, powdered, and mixed with calcium carbide (CaC_2) in a pressure vessel. The water reacts with CaC_2 and produces acetylene gas (C_2H_2), whose quantity is proportional to the moisture content of the sample.

With this method, only physically-capillary bound water is assessed.

Strengths and drawbacks

Being destructive, this method deteriorates the structural integrity each time a measurement is made. Hence it is not suitable for monitoring purposes. Furthermore, no two test samples can be extracted at the same location, which may lead to inconsistent information.

The achieved measurement accuracy is mean (± 3 wt%), as moisture escapes easily during the powdering process.

As with gravimetric methods, chemical methods are insensitive to hazardous environments, they are not temperature dependent and do not require calibration.

The measurement can be rapidly performed on site; testing in laboratory is not necessary.

2.3.2 Non-destructive testing methods

Hygrometric method

Based on the relative humidity of air enclosed in a cavity, the moisture content can be determined using the sorption isotherms. This method is considered to be non-destructive, since, once installed, the relative humidity may be measured continuously without further impact on the host. The relative humidity obtained with this method is a local value, located around the measurement cavity. Only moisture contents in the hygroscopic range are assessed [20].

Hygrometry has been successfully applied to quantify concrete moisture in laboratory applications as well as in-situ [3][9][21][22].

Strengths and drawbacks

Being non-destructive, hygrometric methods allow monitoring of construction materials.

However, electrical RH gauges are impaired by electromagnetic interference and corrosive environments. If the moisture content is investigated, material calibration is required (the sorption isotherms are temperature and material dependent and show hysteresis). The measurement delay depends on the rate at which the RH of the measurement cavity equilibrates with the RH of the surrounding concrete and on the time constant of the RH sensor. Smaller cavities tend to decrease the time-lag effect.

Electrical method

Electrical methods use the dependence of electrical properties (e.g., dielectric constant) on moisture content. At low frequencies (< 100 MHz), the dielectric constant can be expressed as a function of electrical capacity and conductivity (resistivity), both being highly sensitive to a change in moisture. While the electrical capacity is measured using a condenser configuration, the electrical conductivity is usually measured with electrodes. Thanks to its simple and robust working principle, this method is widely used, e.g., [23] and [24]. A multiplexed sensor configuration which allows for in-depth resolved measurements has been proposed by Schiessl et al. [25].

Strengths and drawbacks

Electrical methods are considered to be minimally invasive.

A major drawback is the influence of temperature and ionic concentration on the dielectric constant. Electromagnetic interference, local electro-chemical phenomena near the electrodes and the influence of transition resistivity and capacity between the

electrodes and the material may represent other potential sources of error. In any case, material calibration is required.

The response of electrical methods is immediate, allowing real time monitoring.

Microwave method

The microwave method may be considered as an extension of the electrical methods in the frequency range above 1 GHz (microwave band). It is based on the proportional dependence of the attenuation of electromagnetic energy on the moisture content [26]. The microwave method may be applied for in-depth profile measurements by moving the antenna(s) inside the inspection hole(s), e.g., [27].

Strengths and drawbacks

Material inhomogeneities, such as grains, voids and materials discontinuities, are likely to disturb microwave measurements.

The microwave method has an immediate response (real time). The effect of salt solution conductivity on the dielectric properties of the tested material is minimized at microwave frequencies.

Thermometric method

The thermometric method uses the change in thermal conductivity of a porous material as a function of moisture content. A resistivity wire is introduced into the structure and electrically heated. The moisture content is assessed by means of the calorific power supplied and the temperature in the close neighbourhood of the heating wire [28]. Using several temperature gauges, this configuration may be applied for in-depth distributed measurements. Only physically-capillary bound water is quantified.

Strengths and drawbacks

The thermometric method is suitable for monitoring.

Heating wires and temperature gauges are considered to be insensitive to hazardous environments (electromagnetic interference, corrosive environments). A calibration is necessary in order to define the relationship between moisture content and thermal resistivity of a material. Heating may however influence chemical processes and induce thermal stress in the material such that the thermometric method can not be considered as non-destructive.

The measurements are easily and quickly performed and the response is immediate, allowing real time measurements.

The major drawback of the thermometric method is that it only operates reliably at low moisture contents.

Acoustic method

Acoustic methods use the change of acoustic properties (impedance, resonance) at audible and ultrasonic frequencies of a porous material as a function of the moisture content [29]. Acoustic methods may be applied non-invasively.

Strengths and drawbacks

Since the resonance frequency and quality strongly depend on the measured material, these methods are only used in simple situations. Calibration is essential.

Acoustic methods have an immediate response (real time).

Nuclear methods

Passed through capillary-porous materials, nuclear rays (X, gamma, neutron) experience an energy loss, depending on the dry material and its moisture content. Nuclear methods have a good spatial resolution. Using neutron rays the physically-capillary bound (i.e., with low binding energy) water as well as the chemical and physical-chemical bound water is quantified [30].

Strengths and drawbacks

Resistant to hazardous environments (electromagnetic interference, salts) and temperature independent, nuclear methods allow very accurate measurements. However, an extended material calibration is required.

Results can be obtained in real time.

Nuclear test equipment requires security precautions to prevent the measurement staff from being irradiated. The use of radioactive test equipment requires in most countries an official permission.

Nuclear test equipment is mobile, but often very bulky and heavy and therefore not very practical on site.

Method	Measured quantity	Measurement range (moisture)	Uncertainty (typical)	Spatial resolution	Cross-sensitivity	Potential sources of error
Gravimetric (DT) <i>Reference testing method</i>	Moisture mass	full	± 0.5 wt%	point / averaged	μ : none	Water evaporation / absorption during excavation and transport
Chemical (DT)	Gas pressure	full	± 3 wt%	in-depth, point	μ : none	Water evaporation during powdering
Hygrometric (NDT)	Relative humidity	Hygroscopic domain (0-100 %RH)	± 4 %RH	in-depth, point	RH : none μ : material, temperature, wetting / drying)	Electromagnetic interference (for electrical RH gauges)
Electrical (NDT)	Electrical resistivity, dielectric permittivity, impedance	full	± 2 vol%	in-depth, point / averaged	ρ_w : material, temperature, ions	Electromagnetic interference, polarisation of electrodes, parasite resistivity / capacity between sensor and host
Microwave (NDT)	Dielectric permittivity	full	± 2 vol%	in-depth, point / averaged	ρ_w : material, temperature	Electromagnetic interference
Thermometric (DT)	Thermal conductivity	Low moisture contents	medium	in-depth, point / averaged	μ : material	
Acoustic (NDT)	Resonance, impedance	full	high (qualitative)	in-depth, point / averaged		
Nuclear (NDT)	Volumetric water content (physically-capillary and chemically bound water)	full	low	in-depth, point / averaged	μ : material	

Table 2.1 Summary of common testing methods for moisture assessment in construction materials (DT: destructive testing, NDT: non-destructive testing).

For concrete, the most common methods for in-depth moisture assessment are the gravimetric, electrical and hygrometric methods.

For timber, mainly the gravimetric and the electrical methods are currently applied. This may be due to the predominance of the moisture content as moisture quantifying parameter in timber industry.

In summary, moisture monitoring of construction materials is generally performed electrically by measuring the change of the electrical properties of the material as a function of moisture, or hygrometrically by measuring the relative humidity in a cavity in the material. Currently, electrical sensors are used for both methods. These, however, are often bulky and therefore not adequate for non-destructive testing. Moreover, the single point sensor head of the electrical RH-gauge does not make it possible to perform averaging moisture measurements over a large zone or point multiplexed profile measurements. For in-situ applications the sensitivity of electrical sensors to electromagnetic interference is a reliability issue which should not be underestimated.

2.4 Fibre optic sensors

2.4.1 Structural monitoring

The use of fibre optics for structural monitoring is closely related with the smart structure concept which emerged in the early 1990s. Smart structures describe mechanical and civil engineering structures that integrate a sensing system. This sensing system may help to identify structural wear, damage or deterioration [32]. Smart structures may be enhanced by actuation and control systems, endowing a structure with the ability to react to its environment.

Due to their versatility, robustness and ease of integration, fibre optic sensors have rapidly been recognised as an ideal sensing tool for smart structures [33]. In Europe, the fibre optic smart structure concept appeared around the same period as part of a BRITE-EURAM project named OSTIC (Optical Sensing Technologies for Intelligent Composites) [34]. One of the first practical demonstrations of fibre optic strain and temperature sensing in civil structures was performed during the BRITE-EURAM II project, which started in 1992 under the acronym OSMOS (Optical Fibre Sensing Systems for Monitoring of Structures) [35].

Compared to conventional electrical sensors, fibre optic sensor technology features the following advantages:

- Immune to electromagnetic interference (e.g., sparks, railways, high voltage lines)
- Chemically inert (does not corrode)
- Long term reliability
- Small size
- Easy to multiplex to form multi-point and multi-parameter sensor networks
- Resistant to nuclear and ionising radiations
- Being dielectric, the optical fibre is intrinsically safe to use in explosive environments

Chemical inertia and long term reliability refer to the core component of a fibre optic sensor: the silica fibre. The robustness and reliability of the entire sensor depends of course also on the auxiliary sensor components, such as coating and packaging.

The first five advantages justify the use of fibre optic sensors in harsh civil engineering environments. Fibre optic sensors are, due to their small size and generally permanent integration in the structure, considered to be a non-destructive, minimally invasive testing tool.

Fibre optic sensors may be distinguished as either intrinsic or extrinsic. In an intrinsic sensor, the measurand modulates the transmission properties of the optical fibre while in an extrinsic sensor, the modulation of the light happens outside the fibre and the fibre serves only as a carrier of the measurement information, i.e., it guides the light to the sensor and from the sensor to the reading unit. The measurand induced modulation of the light can be a change in optical delay, a spectral change, an intensity change, a change in polarisation state and a frequency change [36].

In civil engineering, fibre optic sensors have in the past mainly been used to monitor mechanical parameters, such as strain, deformation and pressure, and temperature [37]. Hocker's demonstration that optical fibres can be used to measure strain and temperature intrinsically [38] has certainly played an important role regarding this specialisation.

Sensor concepts for fibre optic strain sensing include Michelson interferometers [39], Fabry-Perot interferometers [40], fibre Bragg gratings [41], and stimulated Brillouin scattering [42].

The fibre optic Michelson interferometer is a long gauge length sensor integrating the strain of a structure between the sensor anchorage points, which are often several meters apart. Inaudi et al. [43] have successfully implemented a Michelson interferometric measurement system (SOFO system) which is compatible with the harsh environment typically found on construction sites. The SOFO system is based

on a low-coherence tandem Michelson interferometer configuration (for more details see 4.4). As both sensor interferometer arms are located side-by-side inside the structure, the temperature effect on the sensor is auto-compensated. The SOFO system is currently the furthest developed fibre optic strain sensing system for structural monitoring.

Fabry-Perot interferometric and fibre Bragg grating sensors are short gauge length (point) sensors, i.e., they are ideal candidates for local strain sensing. Fabry-Perot interferometers (FPIs) are based on the interference between light reflected from two closely spaced surfaces, located in-line with the fibre. FPIs exist in intrinsic, extrinsic and hybrid (in-fibre etalon) configurations. Habel et al. [44] have shown on various occasions that FPI sensors may be successfully applied to structural strain monitoring. Fibre Bragg gratings (FBGs) are periodically index-varying structures in the fibre core reflecting the spectral component of incident light which satisfies the resonance condition of the grating (for more details see 4.3). FBG sensors have been successfully implemented by different researchers as fibre optic strain gauges [45][46][47].

Stimulated Brillouin scattering based sensors represent an elegant way to measure distributed strain. The Brillouin interaction causes the coupling between optical and acoustical waves when a resonance condition is fulfilled. The resonance condition is strain and temperature dependent. Thévenaz et al. [48] have demonstrated successful laboratory and in-situ applications of this technique for distributed strain and temperature monitoring.

2.4.2 Fibre optic humidity sensors

The application of fibre optics for the measurement of humidity has in the past been the subject of only a few research projects. A reason for this may be the transducing of the measurand to a light modulation, which is intrinsically more difficult than for mechanical sensors. In addition, long-term response stability of the sensor, its temperature sensitivity and cross-sensitivity to other (chemical) parameters are more difficult to deal with.

For humidity sensing with fibre optics, several concepts have been reported. They are mainly based on one of the following phenomena (in order of their historical appearance):

- Colorimetric dyes that change colour as a function of humidity; this phenomenon modulates the spectrum and the intensity of light.
- Fluorescent dyes whose emission intensity and lifetime change as a function of humidity.

- Change of end tip reflectivity as a function of humidity; this phenomenon modulates the light intensity.
- Change of refractive index as a function of humidity; this phenomenon modulates the light intensity.
- Change of size as a function of humidity (hygroscopic swelling); this phenomenon may modulate the optical delay or the backscattered signal.

In 1985, Russell et al. [49] were the first to propose a humidity sensor using fibre optics. In their intrinsic point sensor, a colorimetric gelatine film (cobalt chloride), whose absorption spectrum shifts as a function of humidity, is applied as a film on a de-cladded fibre. The spectrum and intensity of the transmitted light is modulated by evanescent field interaction with the gelatine film. This sensor showed a satisfactory response behaviour between 40 and 80 %RH.

In order to overcome the limited relative humidity range of Russell's sensor, Shahriari et al. [50] suggested a modified sensor design with which relative humidities over the whole range could be assessed. Their sensor is based on the cobalt chloride dye being entrapped in the pores of a porous optical fibre (treated borosilicate glass fibre), hence resulting in in-line optical absorption. With this configuration, the RH region, where the sensor is sensitive, can be adapted by varying the dye concentration.

A point multiplexed version of Russell's sensor was proposed by Kharaz et al. [51]. At several locations on an optical fibre the cladding is locally removed and replaced by the colorimetric gelatine films. The humidity induced light attenuation at these sensitive spots is demodulated by optical time-domain reflectometry.

Zhu et al. [52] reported on an extrinsic fibre optic humidity point sensor where a fluorescent instead of an absorbent dye serves as humidity indicator. The dye is immobilised in a polymer matrix on the tip of an optical fibre. Humidity modulates the fluorescence intensity and lifetime.

Potential problems with dye-based sensors are washing out and bleaching of the dye, temperature cross-sensitivity and a restrained sensing range. Moreover, intensity interrogated sensors are sensitive to losses in the optical fibre, introduced by macrobends and dirty connectors for example.

Stuart et al. [53] have chosen a fundamentally different approach. In their extrinsic point sensor, the humidity sensitive reflectivity of metal-coated optical fibre tips modulates the reflected light intensity as relative humidity varies. The sensor features a rapid response, but the reflectivity is temperature dependent and degrades with time.

Mitschke [54] proposed an alternative version of Stuart's concept by replacing the metal coating with a thin-film Fabry-Perot resonator. Sorbed water changes the index of the thin films which are deposited on the tip of the optical fibre. Hence the

reflectivity of the interferometer changes, resulting in a modulation of the intensity of the reflected light.

A similar concept has been adopted by Arregui et al. [55], who proposed an extrinsic point sensor based on a multilayer nano Fabry-Perot cavity deposited on the tip of the fibre. The reflectivity of the Fabry-Perot cavity varies as a function of humidity due to the humidity dependence of the index of the layer materials.

An intrinsic point sensor based on the humidity dependence of the index of an agarose gel coating has been proposed by Bariáin et al. [56]. The intensity of transmitted light is modulated by the evanescent field interaction with the gel, which is located on a tapered region of the fibre.

Sensors based on refractive index variation exhibit intrinsic temperature dependence and the modulated intensity is affected by losses in the optical fibre. Arregui's sensor is interesting for sensing application with a rapidly varying relative humidity (response time less than 1.5 s).

A unique concept for a point multiplexed extrinsic humidity sensor is McMurtry's interferometric sensor [57]. The sensing points are set up as Fizeau interferometers. One mirror of the Fizeau cavity is the fibre collimator and the other one is a mirrored hygroscopic polymer layer, which swells as a function of humidity and thus modulates the cavity length. A low coherence tandem interferometer setup serves for demodulation. The sensor can be temperature compensated by means of a colocated reference cavity without polymer. Compared to the other fibre optic sensors, Fizeau interferometric sensors are rather bulky.

An interesting solution for truly distributed humidity sensing is the microbend sensor proposed by Michie et al. [58]. A hygroscopic polymer (polyurethaneurea hydrogel) rod is attached side-by-side to an optical fibre by means of a helical Kevlar thread. In contact with water, the hydrogel swells and introduces periodic microbends in the fibre. The microbend induced attenuation of the backscattered signal is measured by optical time-domain reflectometry. Relative humidity above 70 %RH and water ingress points have been quantified and localised with a spatial resolution of as small as 0.5 m for sensor lengths exceeding 100 m. This sensor is intended for qualitative assessment and localisation of moisture rather than for measuring relative humidity. The microbend sensor is currently the only fibre optic sensor that has been applied for in-situ moisture monitoring [59].

2.4.3 Fibre optic absorption hygrometer

The humidity sensor proposed in this work makes use of the dependency of the swelling of a hygroscopic material on relative humidity. This concept, called



Figure 2.2 Early example of a Saussure hygrometer (by J.J. Miranda, Coimbra).

absorption hygrometry, is based on the discovery made by Boyle and Goval in the 15th century, who noticed that the length of a cord changes as a function of the surrounding humidity level. In 1783, Horace-Bénédict de Saussure, a Genevean scientist, built the first hygrometer by coupling a human hair under tension with a dial (see Figure 2.2). Natural and synthetic hairs were (and still are) the preferred sensitive elements in mechanical absorption hygrometers, mainly because they are rather stable with respect to temperature variations and reliable over long time periods, compared with other hygroscopic materials.

To our knowledge this work proposes for the first time an absorption hygrometer based on optical fibres.

Preliminary investigations concerning a long gauge fibre optic humidity sensor based on absorption hygrometry were conducted during a visiting stay of the doctoral candidate at the Optoelectronics Division (Prof. Brian Culshaw) of the University of Strathclyde, Glasgow, UK. Inspired by their hydrogel based distributed microbend moisture sensor [58], a Michelson interferometric humidity sensor using a hydrogel coated sensing fibre was realised [60]. However, due to the difficulties in transferring the strain from the swollen hydrogel to the fibre (hydrogel becomes gelatinous and loses its mechanical adhesion to the fibre when wet over long periods), other hygroscopic coating materials have been investigated.

2.5 Concluding remarks

Moisture is a key parameter of liquid and gas transport processes, of chemical and biological degradation processes and of mechanical properties of capillary-porous construction materials. In order to improve the understanding of these phenomena and hence of the material behaviour, moisture monitoring is crucial.

Non-destructive moisture monitoring of construction materials is generally performed electrically by measuring the change of the electrical properties of the material as a function of moisture, or hygrometrically by measuring the relative humidity in a cavity in the material. Currently, electrical sensors are used for both methods. These, however, are often bulky and therefore not adequate for non-destructive testing. Moreover, the single point sensor head of the electrical RH-gauge does not make it possible to perform averaging moisture measurements over a large zone or point multiplexed profile measurements. For in-situ applications the sensitivity of electrical sensors to electromagnetic interference is a reliability issue which should not be underestimated.

Fibre optic sensors have the potential to overcome the mentioned drawbacks of electrical sensors, because they are small, easy to multiplex, immune to electromagnetic interference and their gauge lengths can easily be varied, making it possible to implement point as well as averaging humidity sensors. Several concepts for fibre optic humidity sensors exist, but none has been applied for quantitative moisture assessment in construction materials. The sensors investigated in this work exploit an original concept based on absorption hygrometry.

3. Sensor behaviour models

3.1 Introduction

Analogous to the hair in the mechanical absorption hygrometer (see 2.4.3), the fibre optic absorption hygrometer relies on the swelling of a hygroscopic polymer. The polymer, applied as a transducer coating on the optical fibre, swells as water molecules migrate into it. Since the coating is tightly attached to the fibre, its swelling strains the fibre. This strain may be determined using current optical strain sensing techniques such as fibre Bragg gratings and interferometry. The relative humidity is expressed as a function of the sensor optical path length using appropriate response behaviour models. The use of fibre optic sensor techniques that are already established in structural monitoring allows the sensor to be integrated in existing structural monitoring systems to form multi-point and multi-parameter sensor networks.

This chapter describes the theoretical steady and transient state behaviour of a hygroscopically coated optical fibre that is subjected to relative humidity and temperature variations. The developed models are then applied to describe the response behaviour of a fibre Bragg grating and a Michelson interferometric humidity sensor.

3.2 Strain and temperature dependence of a bare optical fibre

The fundamental parameter, upon which the response of the fibre optic humidity sensor is based, is the optical path length of the sensing section of the optical fibre. Under uniform conditions, the sensor optical path length,

$$\zeta_L \equiv nL \quad (3.1)$$

is the product of

- n , the index of refraction, and
- L , the physical length of the sensing section of the optical fibre.

As n and L depend on strain and temperature, the sensor optical path length also varies as a function of strain and temperature applied to the fibre [38]. Assuming a purely linear dependence, axial fibre strain and temperature changes therefore modulate the sensor optical path length by

$$\Delta\zeta_L = \left[\frac{\partial\zeta_L}{\partial\varepsilon_z} \right]_T \Delta\varepsilon_z + \left[\frac{\partial\zeta_L}{\partial T} \right]_\varepsilon \Delta T, \quad (3.2)$$

where

- $\Delta\zeta_L = \zeta_L - \zeta_{L0}$ is the change of the sensor optical path length from a reference value, ζ_{L0} ,
- $\Delta\varepsilon_z = \varepsilon_z - \varepsilon_{z0}$ is the change of the axial fibre strain from a reference strain state, ε_{z0} , and
- $\Delta T = T - T_0$ is the temperature change from a reference temperature, T_0 .

The expressions in the brackets are the derivatives of ζ_L with respect to ε_z and T , at $\varepsilon_z = \varepsilon_{z0}$ and $T = T_0$, assuming T and ε_z (bracket subscripts) constant, respectively.

Introducing Eq. (3.1) in Eq. (3.2), we obtain

$$\Delta\zeta_L = \left(\underbrace{n \left[\frac{\partial L}{\partial\varepsilon_z} \right]_T}_{\text{elasto-mechanical}} + \underbrace{L \left[\frac{\partial n}{\partial\varepsilon_z} \right]_T}_{\text{strain-optic}} \right) \Delta\varepsilon_z + \left(\underbrace{n \left[\frac{\partial L}{\partial T} \right]_\varepsilon}_{\text{thermo-mechanical}} + \underbrace{L \left[\frac{\partial n}{\partial T} \right]_\varepsilon}_{\text{thermo-optic}} \right) \Delta T, \quad (3.3)$$

where the first term in the first parentheses is the elasto-mechanical effect followed by the strain-optic effect, whereas the first term in the second parentheses is the thermo-mechanical effect followed by the thermo-optic effect.

Knowing that the axial fibre strain is the elastic relative length change of the fibre,

$$\varepsilon_z = \frac{\Delta L}{L} \Rightarrow \left[\frac{\partial L}{\partial\varepsilon_z} \right]_T = \left[\frac{\partial(\Delta L)}{\partial\varepsilon_z} \right]_T = L, \quad (3.4)$$

and defining the effective photoelastic coefficient of the fibre as

$$\hat{p}_e \equiv -\frac{1}{n} \left[\frac{\partial n}{\partial\varepsilon_z} \right]_T, \quad (3.5)$$

the thermal expansion coefficient of the fibre as

$$\alpha_f \equiv \frac{1}{L} \left[\frac{\partial L}{\partial T} \right]_\varepsilon, \quad (3.6)$$

and the thermo-optic coefficient of the fibre core as

$$\xi \equiv \frac{1}{n} \left[\frac{\partial n}{\partial T} \right]_\varepsilon, \quad (3.7)$$

then Eq. (3.3) can be written as

$$\frac{\Delta\zeta_L}{\zeta_L} = (1 - \hat{p}_e)\Delta\varepsilon_z + (\alpha_f + \xi)\Delta T. \quad (3.8)$$

Figure 3.1 illustrates the mechanical and photonic dependence of the sensor optical path length on temperature and axial strain.

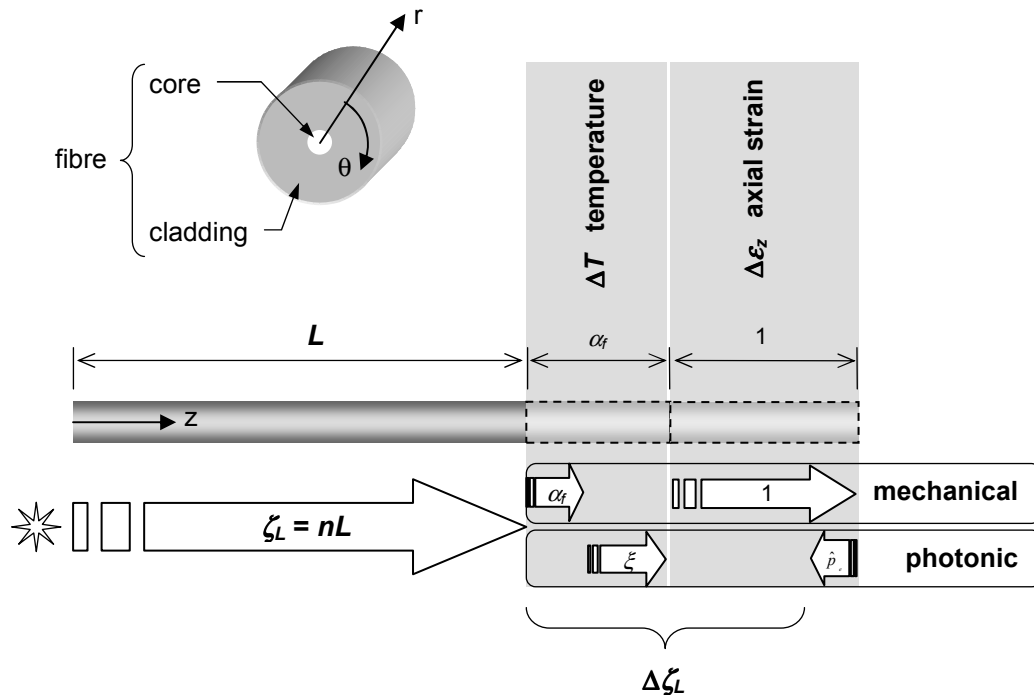


Figure 3.1 Influence of temperature and axial strain on the sensor optical path length of a bare optical fibre (not to scale).

Elasto-mechanical effect

The elasto-mechanical effect, i.e., the variation of the sensor optical path length due to the physical elongation or shortening of the fibre, is the major strain-induced contribution.

Strain-optic effect

The strain-optic effect accounts for the strain dependence of the light velocity. In most cases, it is opposed to the elasto-mechanical effect, i.e., light travels quicker in a strained fibre, thus impeding the mechanically induced elongation of the sensor optical path.

The effective photoelastic coefficient, \hat{p}_e , varies for a given fibre as a function of the radial-to-axial strain ratio. For an isotropic, homogeneous and unshered optical fibre,

\hat{p}_e is expressed as a function of material properties and the applied strain field using the strain-optic theory [61]

$$\hat{p}_e = \frac{n^2}{2} \left(p_{12} + \frac{\varepsilon_r}{\varepsilon_z} (p_{11} + p_{12}) \right), \quad (3.9)$$

where

- p_{11} and p_{12} are coefficients of the strain-optic tensor, and
- ε_r is the radial fibre strain.

Under stationary load a variation of the load intensity does not influence the ratio of the strain components due to the linear load-dependence of the strain field. In the particular case of solely axial loading at constant temperature, $\varepsilon_r/\varepsilon_z = -\nu$, where ν is Poisson's ratio of the fibre material.

Thermo-mechanical effect

The thermo-mechanical effect represents the variation of the sensor optical path length due to the thermal expansion / contraction of the fibre.

The thermal expansion coefficient of silica, α_{SiO_2} , may be assumed to be strain and temperature independent, at least in the temperature range characteristic for civil engineering applications. Nevertheless, GeO₂ doping increases the thermal expansion coefficient [62]. Since for common single-mode fibres the cross-section area of the doped core is less than 1% of the total fibre cross-section area, we can assume that $\alpha_f = \alpha_{SiO_2}$. Being a mechanical property, α_f is wavelength independent.

Thermo-optic effect

The thermo-optic effect accounts for the temperature dependence of the light velocity. It is responsible for more than 90% of the thermally induced variation of the sensor optical path length.

Regarding ξ , various works, such as Takahashi et al. [62], have reported a dependence of the temperature coefficient of the refractive index, $\partial n/\partial T$, on wavelength, temperature and core doping. Since there is no general model relating ξ to these parameters, ξ is best determined experimentally.

Table 3.1 lists the representative values of n ($\approx n_g$), p_{11} , p_{12} , α_f and ξ of a standard telecom single mode fibre (SMF-28 type) at room temperature, as reported in literature. Since the coefficients of the strain- and thermo-optic effects are wavelength dependent, the parameters are shown for the wavelengths of $\lambda = 1310$ nm and $\lambda = 1550$ nm, which are the common operating wavelengths in the near-infrared band.

Parameter	$\lambda = 1310 \text{ nm}$	Ref.	$\lambda = 1550 \text{ nm}$	Ref.
Group index of refraction, n_g	1.450		1.468	
Strain-optic coeff., p_{11}	0.121	[63]	0.121	[38]
Strain-optic coeff., p_{12}	0.270	[63]	0.270	[38]
Thermal exp. coeff., $\alpha_f [\text{K}^{-1}]$	$5 \cdot 10^{-7}$	[38]	$5 \cdot 10^{-7}$	[38]
Thermo-optic coeff., $\xi [\text{K}^{-1}]$	$61.7 \cdot 10^{-7}$	[45]	$(55 \pm 4.8) \cdot 10^{-7}$	[64]

Table 3.1 Representative parameters of a SMF-28 type single-mode fibre (3% GeO₂ doping) at room temperature and wavelengths of 1310 nm and 1550 nm.

3.3 Steady state behaviour of the coated optical fibre

3.3.1 Optical response

The optical fibre constituting the sensors developed in this work is supposed to be free of any external strain, i.e., it is mechanically independent of its host. The only fibre strain arises from the differential thermal and hygroscopic expansions of the fibre and coating materials. Assuming that the coating adheres perfectly to the fibre and that the fibre is infinitely long, such that plane sections remain plane after deformation, the change of the axial fibre strain, $\Delta\varepsilon_{z,f}$, due to relative humidity and temperature changes is

$$\Delta\varepsilon_{z,f} = (\beta_{cf} - \beta_f)\Delta RH + (\alpha_{cf} - \alpha_f)\Delta T, \quad (3.10)$$

where

- β_{cf} and α_{cf} are the hygroscopic and thermal longitudinal expansion coefficients of the coated fibre respectively (see 3.3.2),
- β_f is the hygroscopic expansion coefficient of the fibre, and
- $\Delta RH = RH - RH_0$ is the change of relative humidity from a reference state, RH_0 .

As silica is hygroscopically inert, $\beta_f = 0$.

In the linear relation proposed in Eq. (3.10), the variation of the partial vapour pressure due to a change in temperature at constant RH is supposed to not affect the hygroscopic expansion of the coating, i.e., at increasing temperatures the reduced potential of the water molecules to penetrate the coating polymer matrix due to molecules' higher kinetic energy (faster molecules are less likely to be adsorbed) compensates for the higher vapour concentration. Sacher et al. [65] reported that DuPont's PI polyimide, which is the transducer coating material used in this work (see 4.2), exhibits temperature independent sorption isotherms between 25 and 85 °C.

As the amount of absorbed water is the determining factor of hygroscopic swelling of polymeric materials, the proposed model is valid in the present case.

Introducing the axial fibre strain change expressed in Eq. (3.10) into Eq. (3.8), the relative sensor optical path length change due to a relative humidity and temperature change becomes

$$\frac{\Delta\zeta_L}{\zeta_L} = S_{RH}\Delta RH + S_T\Delta T, \quad (3.11)$$

where,

- S_{RH} is the relative humidity sensitivity¹ of the coated fibre

$$\begin{aligned} S_{RH} &= (1 - \hat{p}_e)\beta_{cf} \\ &= \beta_{cf} - \hat{p}_e\beta_{cf} \end{aligned} \quad (3.12)$$

- and S_T is the temperature sensitivity of the coated fibre

$$\begin{aligned} S_T &= (1 - \hat{p}_e)(\alpha_{cf} - \alpha_f) + (\alpha_f + \xi) \\ &= \alpha_{cf} - \hat{p}_e(\alpha_{cf} - \alpha_f) + \xi \end{aligned} \quad (3.13)$$

Similar to the fundamental expression of the sensor optical path length modulation in Eq. (3.8), the sensitivities are expressed as the sum of a mechanical, a strain-optic and, for S_T only, a thermo-optic contribution (see Figure 3.2).

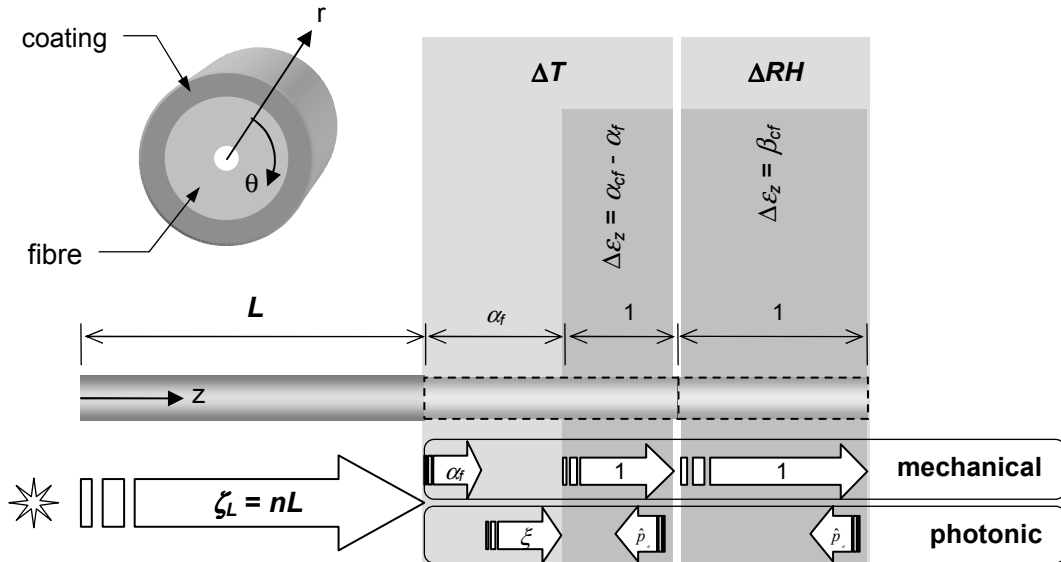


Figure 3.2 Influence of temperature and relative humidity on the sensor optical path length of a coated optical fibre (not to scale).

¹ In this work, sensitivity defines the relative sensor optical path length change for a unitary change of the corresponding measurand. This may not agree with its use sometimes found elsewhere, defining sensitivity to be the minimum detectable measurand change.

3.3.2 Mechanical behaviour

The longitudinal expansion coefficients of the coated fibre are determined using a mechanical model wherein an infinitely long bi-material composite rod is subjected to differential material expansion. Assuming a perfect cohesion between the two materials, a temperature or relative humidity variation results in a constrained deformation of the two materials. To describe the mechanical behaviour of the coated fibre, a one-dimensional axial (1-D), and a three-dimensional (3-D) model are developed and compared.

3.3.2.1 Analytical 1-D model

The 1-D model is formulated using the condition of static equilibrium of the axial forces in the fibre and in the coating,

$$\sigma_{z,f}A_f + \sigma_{z,c}A_c = 0, \quad (3.14)$$

where

- $\sigma_{z,i}$ are the axial normal stresses and
- A_i are the cross-section areas of the fibre ($i = f$) and of the coating ($i = c$),

and the condition of kinetic compatibility of the axial fibre and coating deformations,

$$\frac{\Delta L_f}{L} = \frac{\Delta L_c}{L} = \frac{\Delta L_{cf}}{L}, \quad (3.15)$$

where

- $\Delta L_f/L = \varepsilon_{z,f} + \alpha_f \Delta T$ is the total (i.e., elastic and thermal) axial relative length change of the fibre,
- $\Delta L_c/L = \varepsilon_{z,c} + \alpha_c \Delta T + \beta_c \Delta RH$ is the total (i.e., elastic, thermal and hygroscopic) axial relative length change of the coating, and
- $\Delta L_{cf}/L = \alpha_{cf} \Delta T + \beta_{cf} \Delta RH$ is the total (i.e., thermal and hygroscopic) axial relative length change of the coated fibre.
- $\varepsilon_{z,i}$ are the axial strains of the fibre ($i = f$) and of the coating ($i = c$), and
- α_c and β_c are the thermal and hygroscopic expansion coefficients of the coating respectively.

Assuming isotropic, linear-elastic fibre and coating materials obeying Hooke's law, i.e.,

$$\begin{aligned}\sigma_{z,f} &= E_f \varepsilon_{z,f} \\ \sigma_{z,c} &= E_c \varepsilon_{z,c}\end{aligned}\quad (3.16)$$

where

- E_i are Young's moduli of the fibre ($i = f$) and of the coating ($i = c$),

we can express the longitudinal expansion coefficients of the coated fibre by substituting Hooke's law (Eq. (3.16)) in the equilibrium condition (Eq. (3.14)) and then combining the equilibrium with the compatibility condition (Eq. (3.15)), i.e.,

$$\begin{aligned}\alpha_{cf} &= k_f \alpha_f + k_c \alpha_c \\ \beta_{cf} &= k_c \beta_c\end{aligned}\quad (3.17)$$

where

- $k_i = E_i A_i / \sum_j E_j A_j$ are the stiffness proportions of the fibre ($i = f, j = f, c$) and of the coating ($i = c, j = f, c$) with respect to the coated fibre.

Knowing that the fibre is hygroscopically inert, i.e., $\beta_f = 0$, we notice the similarity between the expressions of α_{cf} and β_{cf} in Eq. (3.17).

3.3.2.2 Analytical 3-D model

A 3-D approach is used to model more realistically the mechanical behaviour of the optical fibre by taking into account axial, radial and tangential deformations. The importance of this can be illustrated by the fact that most materials exhibit a lateral contraction (or swelling) when pulled (or compressed), which is proportional to the amplitude and normal to the direction of the applied load. The proportionality factor of this transversal strain is called Poisson's ratio, which is a material constant and ranges from near zero (for highly compressible materials such as cork) to 0.5 (for incompressible materials such as rubber)². In a partially constrained system being subjected to differential material expansion, a transversal strain inevitably affects the axial strain. For the coated fibre this signifies that the tangential compression of the coating due to an expansion of the coating material amplifies its longitudinal expansion and hence the longitudinal expansion of the system, α_{cf} and β_{cf} .

The coated fibre can be modelled as an infinitely long bi-material composite rod with an inner, plain cylinder (fibre) and a concentric outer, hollow cylinder (coating). In a first step the 3-D strain and stress fields in a section of each cylinder are expressed separately using the equilibrium and compatibility conditions of the circular plane and

² In theory, i.e., based on thermodynamic considerations of strain energy, Poisson's ratio may range from -1.0 to +0.5. However, only very few materials with negative ratios are known.

a valid 3-D constitutive law. In a second step the two cylinders are coupled together using the corresponding static and kinetic boundary conditions.

The following expressions are formulated for a thermal load (ΔT). However, the RH-analogues can be obtained by substituting the hygroscopic expansion coefficients for the thermal ones.

Neglecting higher order terms, Timoshenko [66] has presented the in-plane equilibrium condition of a circular section under a hydrostatic load as

$$\sigma_{\theta,i}(r) - \sigma_{r,i}(r) - r \frac{d}{dr} \sigma_{r,i}(r) = 0, \quad (3.18)$$

where

- $\sigma_{\theta,i}(r)$ and $\sigma_{r,i}(r)$ are the tangential and radial normal stresses at radial coordinate r respectively, identified by subscript $i = f$ for fibre and $i = c$ for coating.

Due to the uniform, axisymmetric loading, no shear stresses appear and the normal stresses are axisymmetric, depending for a given system only on the radial coordinate r .

If we designate the in-plane displacement of a cylindrical surface with radius r by $u_i(r)$, then the radial and tangential strains at radial coordinate r , $\varepsilon_{r,i}(r)$ and $\varepsilon_{\theta,i}(r)$ respectively, can be expressed with the compatibility condition of a circular section, i.e.,

$$\begin{aligned} \varepsilon_{r,i}(r) &= \frac{d}{dr} u_i(r) - \alpha_i \Delta T \\ \varepsilon_{\theta,i}(r) &= \frac{1}{r} u_i(r) - \alpha_i \Delta T \end{aligned} \quad (3.19)$$

where

- α_i is the thermal expansion coefficient.

As for an infinitely long cylinder plane sections are supposed to remain plane, the axial strain, $\varepsilon_{z,i}$, does not vary with r , i.e.,

$$\varepsilon_{z,i} = (\alpha_{cf} - \alpha_i) \Delta T. \quad (3.20)$$

Assuming the fibre and the coating material to be linear-elastic and isotropic, we can use Hooke's generalised constitutive law given by

$$\begin{bmatrix} \sigma_{z,i}(r) \\ \sigma_{r,i}(r) \\ \sigma_{\theta,i}(r) \end{bmatrix} = \frac{E_i}{(1+\nu_i)(1-2\nu_i)} \begin{bmatrix} (1-\nu_i)\varepsilon_{z,i} + \nu_i(\varepsilon_{r,i}(r) + \varepsilon_{\theta,i}(r)) \\ (1-\nu_i)\varepsilon_{r,i}(r) + \nu_i(\varepsilon_{z,i} + \varepsilon_{\theta,i}(r)) \\ (1-\nu_i)\varepsilon_{\theta,i}(r) + \nu_i(\varepsilon_{r,i}(r) + \varepsilon_{z,i}) \end{bmatrix} \quad (3.21)$$

where

- ν_i is Poisson's ratio.

Having introduced the strain expressions (Eqs. (3.19) and (3.20)) into the constitutive law (Eq. (3.21)) and having substituted the latter for the stresses in the equilibrium condition (Eq. (3.18)), we can rewrite the equilibrium condition as a function of $u_i(r)$ and r ,

$$\frac{d^2}{dr^2}u_i(r) + \frac{1}{r}\frac{d}{dr}u_i(r) - \frac{1}{r^2}u_i(r) = 0. \quad (3.22)$$

As it can be demonstrated by substitution, the general solution of this differential equation is

$$u_i(r) = \left(C_{1,i}r + \frac{C_{2,i}}{r} \right) \Delta T, \quad (3.23)$$

where

- $C_{1,i}$ and $C_{2,i}$ are the constants for a unitary temperature change, only depending on the boundary conditions of the corresponding section.

We notice that the displacement is proportional to the applied load (ΔT), as expected for linear-elastic materials.

Using this explicit form of $u_i(r)$, we can rewrite the constitutive law for a homogenous, linear-elastic and isotropic cylinder as,

$$\begin{bmatrix} \sigma_{z,i} \\ \sigma_{r,i}(r) \\ \sigma_{\theta,i}(r) \end{bmatrix} = \frac{E_i}{(1+\nu_i)(1-2\nu_i)} \begin{bmatrix} \alpha_{cf} - \alpha_i + \nu_i(2C_{1,i} - \alpha_{cf} - \alpha_i) \\ C_{1,i} - \frac{C_{2,i}}{r^2} - \alpha_i + \nu_i\left(\frac{2C_{2,i}}{r^2} + \alpha_{cf} - \alpha_i\right) \\ C_{1,i} + \frac{C_{2,i}}{r^2} - \alpha_i + \nu_i\left(-\frac{2C_{2,i}}{r^2} + \alpha_{cf} - \alpha_i\right) \end{bmatrix} \Delta T \quad (3.24)$$

It is of interest to note that not only $\varepsilon_{z,i}$, but also $\sigma_{z,i}$ is independent of r .

Considering the two cylinders, there are five parameters ($C_{1,f}$, $C_{2,f}$, $C_{1,c}$, $C_{2,c}$ and α_{cf}) to be determined in order to describe the mechanical behaviour of the coated fibre. These unknowns are found by solving a system of five equations representing the five boundary conditions, which are:

- | | |
|--|---|
| 1. plain fibre cylinder | $u_f(r=0) = 0$ |
| 2. radial compatibility of fibre with coating at interface | $u_f(r=a) = u_c(r=a)$ |
| 3. radial stress continuity at fibre/coating interface | $\sigma_{r,f}(r=a) = \sigma_{r,c}(r=a)$ |
| 4. coating surface unconstrained | $\sigma_{r,c}(r=b) = 0$ |
| 5. equilibrium between axial forces in fibre and coating | $a^2 \sigma_{z,f} + (b^2 - a^2) \sigma_{z,c} = 0$ |

where

- a and b are the fibre and coating outer radii respectively.

Conditions 1 and 2 are the kinetic boundary conditions relying on the radial displacements given in Eq. (3.23), whereas conditions 3, 4 and 5 are the static boundary conditions involving the stresses expressed in Eq. (3.24).

The general expressions of the unknowns as a function of the fibre geometry and the material properties are given in the annexe. We note that $C_{2,f} = 0$, which is required in order to satisfy condition 1, regardless of any of the other parameters' values. Consequently, as expected for a plain cylinder with a hydrostatic load, the radial and tangential stresses are equal and constant over the whole fibre section, i.e., $\sigma_{r,f} = \sigma_{\theta,f}$. Setting Poisson's ratio of the fibre and the coating materials to zero, i.e., $\nu_f = \nu_c = 0$, we observe that the expression of the thermal longitudinal expansion coefficient of the coated fibre is as expected identical to the 1-D expression presented in Eq. (3.17), i.e., $\alpha_{cf}^{3-D} = \alpha_{cf}^{1-D}$.

3.3.2.3 Numerical model

The numerical finite element (FE) model is implemented with the ANSYS software package. The coated fibre is modelled using two laterally connected, rectangular 2-D meshes of quadrilateral and axisymmetric 4-node-elements representing the fibre and the coating respectively. Considering the expected high radial stress gradient in the coating, the coating is, in radial direction, meshed denser than the fibre. Figure 3.3 shows the initial and deformed mesh for the typical fibre geometry under thermal loading. The fibre and coating materials are defined using isotropic, linear-elastic behaviour models. In order to simulate the strain and stress fields in an infinitely long, unconstrained coated fibre, the nodes of one perpendicular end face of the (finite) mesh are restrained from axial displacement while the opposite end face is left free to deform. Test runs have shown that a length-to-radius ratio of the model dimensions bigger than 3 is enough for the partially constrained bottom end face to be sufficiently far away from the unconstrained upper end face, such that the calculated strains at the bottom end face can be considered undisturbed and hence representative of an infinitely long fibre. In order to load the structure, a uniform and unitary temperature raise is applied ($\Delta T = 1$ K). Defining a thermal expansion coefficient for the fibre and coating materials, the temperature change is able to act on the coated fibre.

The FE-model does not allow for an explicit specification of hygroscopic expansion coefficients. However, due to the mechanical analogy of thermal and hygroscopic expansion, the hygroscopic load case may be treated as a thermal load case by applying the hygroscopic expansion coefficients as pseudo thermal expansion coefficients.

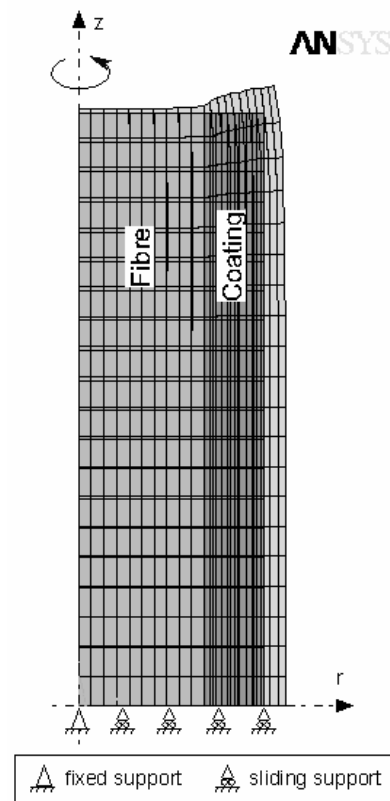


Figure 3.3 Finite element mesh with superimposed deformed state.

3.3.2.4 Discussion of mechanical models

For verifying the consistency of the models, the analytical 1-D and 3-D models were compared with the numerical model. All results refer to a typical polyimide coated optical fibre with a bare fibre diameter of 127 μm , a coating thickness of 15 μm and with the mechanical material properties listed in Table 3.2.

Properties	Fibre	Ref.	Coating	Ref.
Young's modulus, E [GPa]	72	[67]	2.45	[68]
Poisson's ratio, ν	0.17	[38]	0.41	[68]
Thermal expansion coeff., α [K^{-1}]	$5.0 \cdot 10^{-7}$	[38]	$4 \cdot 10^{-5}$	[68]
Hygroscopic expansion coeff., β [%RH $^{-1}$]	0		$7.0 \cdot 10^{-5}$	[69]

Table 3.2 Characteristic mechanical properties of the fibre (fused silica) and the coating (polyimide).

Regarding the 1-D model, we may compare the analytical and the numerical solutions by setting Poisson's ratios in the FE-model to zero. The analytically determined thermal longitudinal expansion coefficient (Eq. (3.17)) is $\alpha_{cf}^{1-D} = 1.20 \cdot 10^{-6} \text{ K}^{-1}$, which is identical to the value obtained with the FE-model. The analytical and numerical solutions also correspond for the hygroscopic load case, with a hygroscopic longitudinal expansion coefficient of the coated fibre of $\beta_{cf}^{1-D} = 1.24 \cdot 10^{-6} \text{ \%RH}^{-1}$.

Using a 3-D approach, the longitudinal expansion coefficients of the coated fibre are $\alpha_{cf}^{3-D} = 1.39 \cdot 10^{-6} \text{ K}^{-1}$ and $\beta_{cf}^{3-D} = 1.58 \cdot 10^{-6} \text{ \%RH}^{-1}$. Again, the analytical and the numerical results match.

Table 3.3 lists the calculated thermal and hygroscopic longitudinal expansion coefficients of the coated fibre.

Long. expansion coefficient of coated fibre	1-D model		3-D model	
	Analytical	Numerical	Analytical	Numerical
α_{cf} [10^{-6} K^{-1}]	1.20	1.20	1.39	1.39
β_{cf} [$10^{-6} \text{ \%RH}^{-1}$]	1.24	1.24	1.58	1.58

Table 3.3 Thermal and hygroscopic longitudinal expansion coefficients of a polyimide coated fibre (coating thickness 15 μm , material properties from Table 3.2), calculated with the 1-D and 3-D models.

We notice that the thermal longitudinal expansion coefficients obtained with the 3-D model, α_{cf}^{3-D} , is 16% higher than α_{cf}^{1-D} . β_{cf}^{3-D} is even 27% higher than β_{cf}^{1-D} . This indicates that a 1-D approach underestimates the mechanical contribution to the sensor sensitivities compared with the 3-D approach. For thicker coatings, however, the deviation between the models becomes smaller. The use of a 3-D approach is especially important for calculating the hygroscopic expansion of fibres with thin coatings.

Figure 3.4 to Figure 3.6 show the theoretical, temperature induced axial, radial and tangential fibre and coating stresses, determined with the analytical (Eq. (3.24)) and the numerical 3-D model. The analytical and the numerical results agree in trend as well as numerically, in as far as they show

- uniform tensile axial stress in fibre,
- uniform compressive axial stress in coating,
- equal and uniform radial and tangential stresses in fibre,
- radial stress continuity at fibre-coating interface and
- no radial stress at outer coating surface.

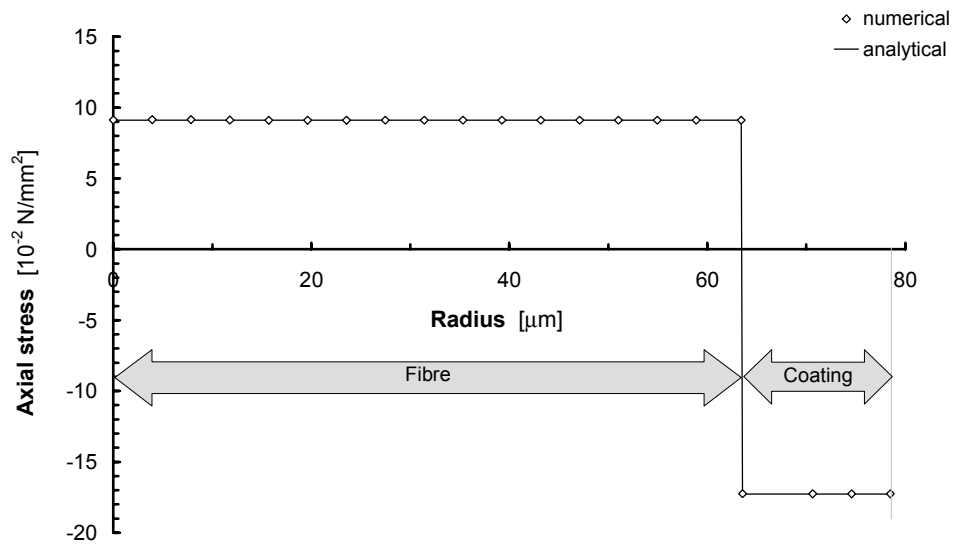


Figure 3.4 Theoretical axial stress distribution over the section of a coated optical fibre due to a unitary thermal load ($\Delta T = 1$ K), calculated with an analytical and a finite element model.

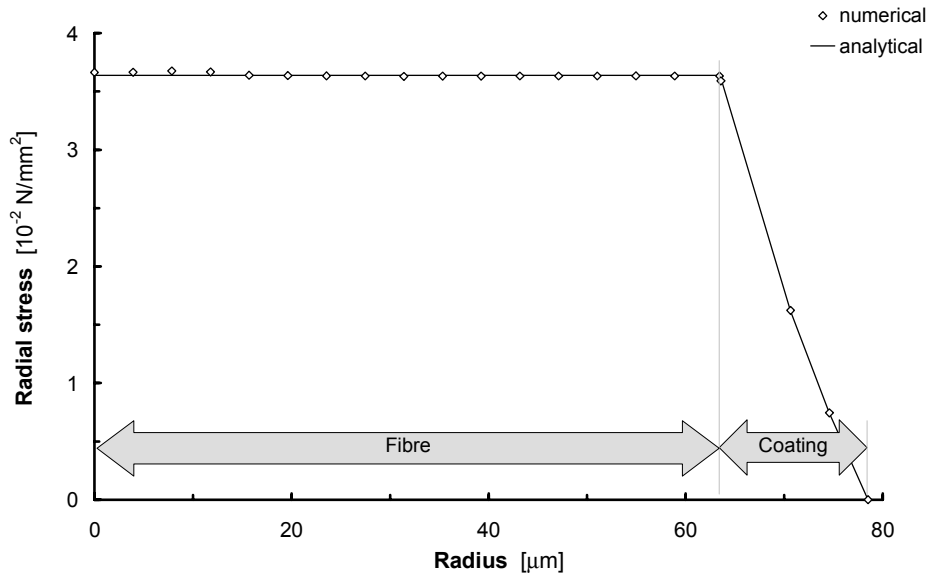


Figure 3.5 Theoretical radial stress distribution over the section of a coated optical fibre due to a unitary thermal load ($\Delta T = 1 \text{ K}$), calculated with an analytical and a finite element model.

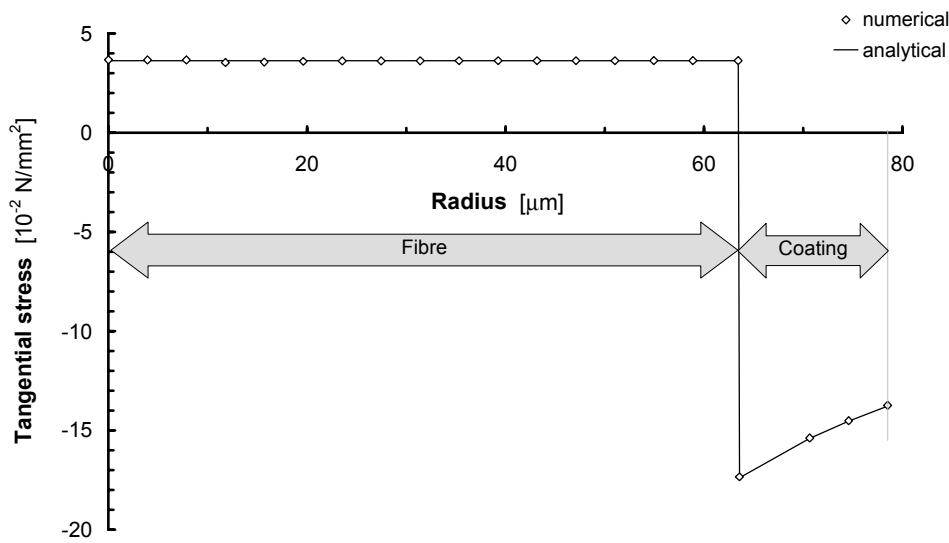


Figure 3.6 Theoretical tangential stress distribution over the section of a coated optical fibre due to a unitary thermal load ($\Delta T = 1 \text{ K}$), calculated with an analytical and a finite element model.

3.3.3 Discussion of optical response

We have seen in 3.3.1 and 3.3.2 that the RH- and T-sensitivities of the coated fibre are a function of the material and the geometrical properties. In the experimental part of this work the coating thickness is the only parameter to be varied. The theoretical dependence of the RH- and T-sensitivities on the coating thickness is plotted in Figure 3.7. The sensitivity values are calculated with the 3-D model based on the material properties given in Table 3.1 ($\lambda = 1550$ nm) and Table 3.2. For thin coatings, the RH- and T-sensitivities depend nearly linearly on the coating cross-section area, while they eventually saturate at $S_{RH}^{max} = \beta_c - \hat{p}_e \beta_c$ and $S_T^{max} = \alpha_c - \hat{p}_e (\alpha_c - \alpha_f) + \xi$ respectively, for (infinitely) thick coatings. For a bare fibre, the RH-sensitivity is zero as expected and the T-sensitivity is $S_T^{min} = \alpha_f + \xi$. With the hygroscopic expansion coefficient of the coating material being higher than the thermal one (see Table 3.2), S_{RH} is more sensitive to coating thickness variations than S_T .

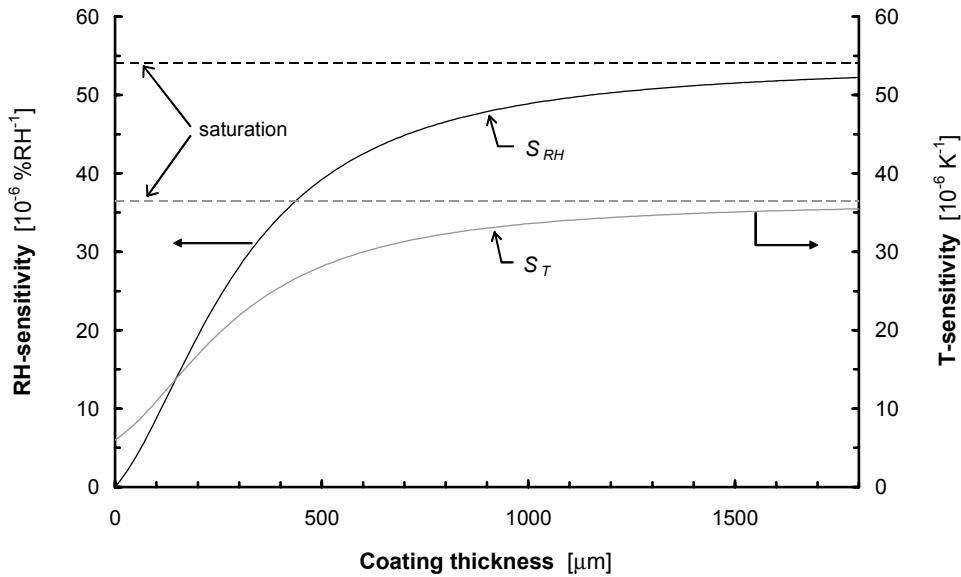


Figure 3.7 RH- and T-sensitivities as a function of the coating thickness, calculated with the 3-D model.

If the fibre diameter was reduced (e.g., 80 μm for a reduced cladding diameter fibre), the sensitivities would increase due to the higher coating-to-fibre stiffness ratio (and hence, according to Eq. (3.17), bigger longitudinal expansion coefficients of the coated fibre).

Figure 3.8 and Figure 3.9 illustrate the model-dependence of the RH- and T-sensitivities with respect to the coating thickness. For thin coatings, the difference between the sensitivities based on the 1-D and the 3-D models is mainly due to the model-dependence of the elasto-mechanical term, as seen in 3.3.2.4. For the given fibre and coating properties, S_{RH}^{1-D} is up to 14% smaller than S_{RH}^{3-D} , whereas the

relative deviation between S_T^{1-D} and S_T^{3-D} is attenuated due to the model- and coating thickness-independent thermo-optic contribution. In the common case of thin coatings, the 3-D model is thus especially indicated for determining S_{RH} .

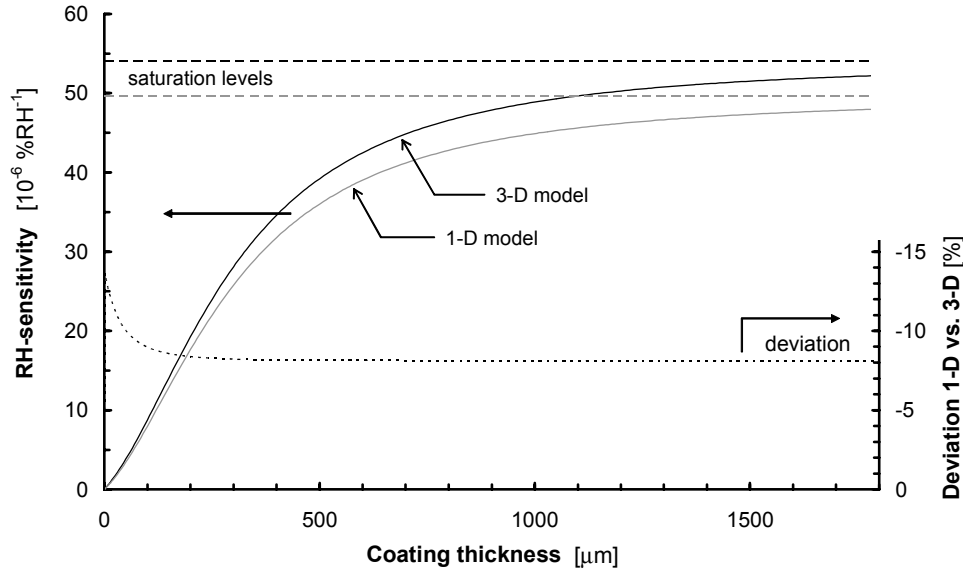


Figure 3.8 RH-sensitivity as a function of the coating thickness, calculated with the 1-D and 3-D models.

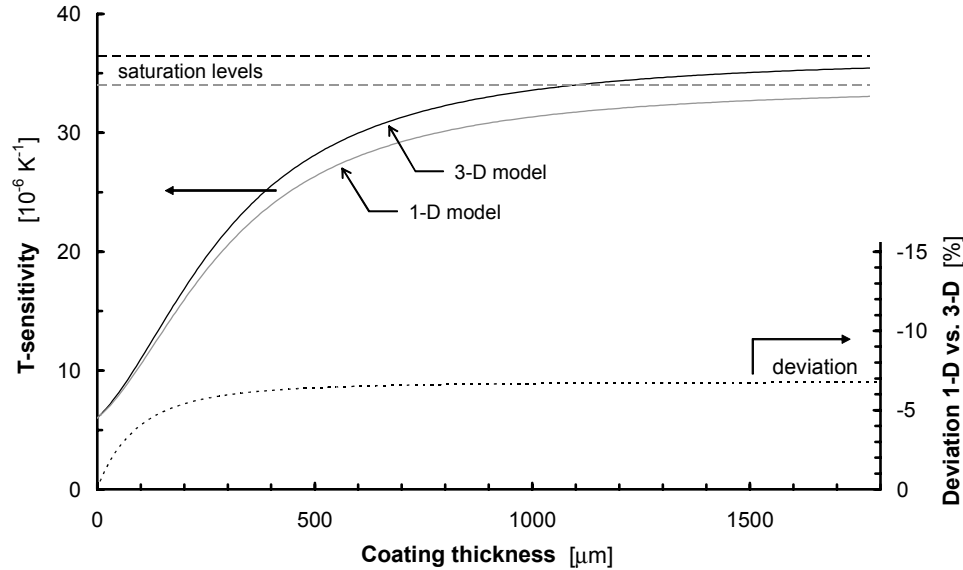


Figure 3.9 T-sensitivity as a function of the coating thickness, calculated with the 1-D and 3-D models.

Regarding thick coatings we notice that the difference between the maximum sensitivities calculated using a 1-D and a 3-D approach no longer depends on the longitudinal expansion coefficient of the coated fibre ($\beta_{cf} = \beta_c$, $\alpha_{cf} = \alpha_c$), but only on the effective photoelastic coefficient. Figure 3.10 shows \hat{p}_e as a function of the

coating thickness. For thick coatings, \hat{p}_e^{3-D} eventually saturates at a value that is smaller than that of \hat{p}_e^{1-D} . According to the 1-D model where the radial fibre strain is not considered, $\hat{p}_e^{1-D} = n^2/2 p_{12}$ remains constant irrespective of the coating thickness. On the other hand, \hat{p}_e^{3-D} , which varies as a function of the radial-to-axial fibre strain ratio (see Eq. (3.9)), is superior to \hat{p}_e^{1-D} for thin coatings (axial and radial fibre strains have the same sign), but lower than \hat{p}_e^{1-D} for thick coatings (axial and radial fibre strains have opposite signs). Using the material parameters shown in Table 3.1 ($\lambda = 1550$ nm) and Table 3.2, the values of the effective photoelastic coefficient are $\hat{p}_e^{1-D} = 0.291$, $\hat{p}_e^{3-D,max} = 0.415$ (coating thickness $\rightarrow 0$) and $\hat{p}_e^{3-D,min} = 0.228$ (coating thickness $\rightarrow \infty$). With a $67.5 \mu\text{m}$ thick coating, the fibre is elastically unstrained in radial direction ($\hat{p}_e^{3-D} = \hat{p}_e^{1-D}$).

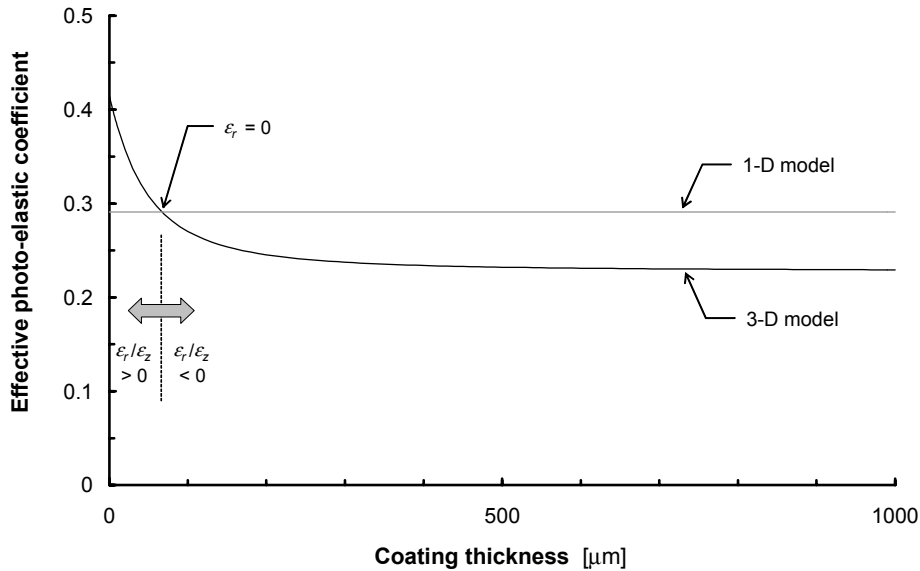


Figure 3.10 Effective photo-elastic coefficient as a function of the coating thickness, calculated with the 1-D and 3-D models.

We notice that in the particular case of stationary, axisymmetric and evenly distributed mechanical loading of the fibre and of the coating along their axis (which is the case for thermal and hygroscopic expansion), the individual fibre and coating originated loads can be assumed to share the same location on the fibre. Any modification of the fibre and coating expansion coefficients (which may be considered as the load intensities of the fibre and the coating respectively) can therefore be represented as the intensity change of a single, stationary load, which has, as stated before, no influence on the radial-to-axial fibre strain ratio. For this reason, the value of \hat{p}_e remains identical, irrespective of whether there is a relative humidity or a temperature variation.

3.4 Transient state behaviour of the coated optical fibre

The transient state behaviour of the hygroscopic response of the sensor is characterised by the rate at which the water molecules penetrate the polymeric transducer coating and accumulate therein. The water transport and accumulation in the coating material is a non-stationary diffusion process, which can be described by Fick's 2nd law,

$$\frac{\partial c}{\partial t} = D\nabla^2 c, \quad (3.25)$$

where

- $c = c(x, y, z, t)$ is the concentration of a diffusant at position (x, y, z) and time t , and
- D is the constant diffusion coefficient, or diffusivity.

The following three diffusion scenarios are investigated:

1. Plane layer with steady state boundary conditions
2. Cylindrical layer with steady state boundary conditions
3. Cylindrical layer with nonsteady state boundary conditions

While the first scenario depicts diffusion in a plane sheet, the second and third scenarios use a cylindrical model to account better for the tubular geometry of the coating. The third scenario assumes nonsteady state boundary conditions, which resembles more the kind of environment to which the sensor will be subjected. The third scenario also accounts for a concentration dependent diffusivity. As will be seen in 4.6.2 diffusivity is likely to depend on concentration for hygroscopically swelling polymers.

In all models the layer thickness remains constant (swelling is neglected), the coating/fibre interface is impermeable, and the diffusant diffuses perpendicularly to the layer faces (one-dimensional diffusion).

3.4.1 Plane layer with steady state boundary conditions

This is the simplest model assuming one-dimensional diffusion in a plane layer with an abrupt concentration-change. The one-dimensional expression of Fick's diffusion equation (Eq. (3.25)) is

$$\frac{\partial c}{\partial t} = D \frac{\partial^2 c}{\partial x^2}, \quad (3.26)$$

and the appropriate initial and boundary conditions are

- $c(0 < x < L, t = 0) = c_0$,
- $c(x = 0, t \geq 0) = c_0 + \Delta c = c_{ext}$ and
- $\frac{\partial c}{\partial x}(x = L, t \geq 0) = 0$,

where

- c_0 is the uniform initial concentration,
- Δc is the external concentration change at $t = 0$,
- c_{ext} is the external concentration after the concentration has changed and
- L is the layer thickness.

Figure 3.11 illustrates the layer geometry with the initial concentration levels at $t = 0$.

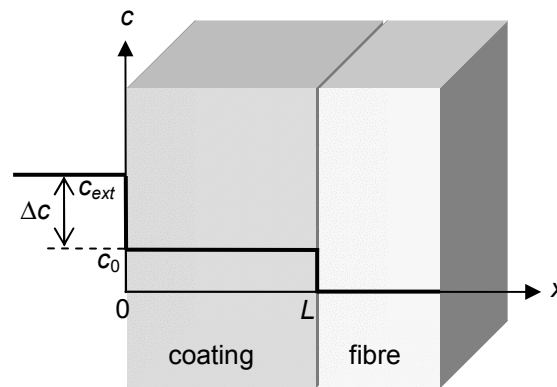


Figure 3.11 Scheme of the plane layer with initial concentration levels at $t = 0$.

For this case Crank [69] proposes an explicit analytical expression for the normalised accumulated mass of diffusant which has entered (or left) the layer at time t , M_t/M_∞ (M_∞ is the accumulated mass at equilibrium),

$$\frac{M_t}{M_\infty} = 1 - \sum_{n=0}^{\infty} \frac{8}{(2n+1)^2 \pi^2} \exp\left(-\frac{D(2n+1)^2 \pi^2 t}{4L^2}\right). \quad (3.27)$$

3.4.2 Cylindrical layer with steady state boundary conditions

For radial diffusion in a cylinder, the general diffusion equation shown in Eq. (3.25) can be expressed in cylindrical coordinates

$$\frac{\partial c}{\partial t} = D \frac{1}{r} \frac{\partial}{\partial r} \left(r \frac{\partial c}{\partial r} \right). \quad (3.28)$$

The initial and boundary condition for the tubular layer with an abrupt external concentration change are

- $c(a < r < b, t = 0) = c_0$,
- $c(r = b, t \geq 0) = c_0 + \Delta c = c_{ext}$ and
- $\frac{\partial c}{\partial r}(r = a, t \geq 0) = 0$,

where

- a and b are the fibre and coating outer radii respectively.

Figure 3.12 illustrates the layer geometry with the initial concentration levels at $t = 0$.

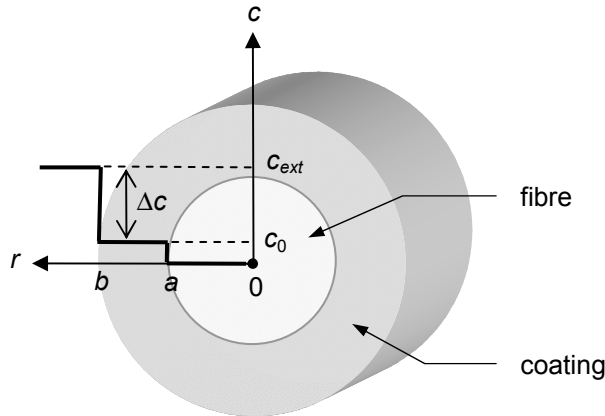


Figure 3.12 Scheme of the tubular layer with initial concentration levels at $t = 0$.

Considering the given boundary conditions, Crank [69] (§5.4.2) proposes an analytical solution for Eq. (3.28)

$$\begin{aligned} \frac{c(r, t)}{c_{ext}} &= 1 - \pi \sum_{n=1}^{\infty} \exp(-D\alpha_n^2 t) J_1(a\alpha_n) J_0(b\alpha_n) \\ &\times \frac{Y_0(r\alpha_n) J_1(a\alpha_n) - J_0(r\alpha_n) Y_1(a\alpha_n)}{J_0(b\alpha_n)^2 - J_1(a\alpha_n)^2} \end{aligned} \quad (3.29)$$

where

- $J_i()$ and $Y_i()$ are the first and second kind Bessel functions of order i respectively, and
- α_n is the n^{th} positive root of $J_1(a\alpha)Y_0(b\alpha) - J_0(b\alpha)Y_1(a\alpha) = 0$.

The normalised accumulated mass of diffusant, which has entered (or left) the coating at time t , is

$$\frac{M_t}{M_\infty} = \frac{1}{c_{ext}(b-a)} \int_a^b c(r,t) dr. \quad (3.30)$$

3.4.3 Cylindrical layer with concentration dependent diffusivity and nonsteady state boundary conditions

Accounting for concentration dependent diffusivity, $D(c)$, the differential equation of radial diffusion in a cylinder is expressed similar to Eq. (3.28),

$$\frac{\partial c}{\partial t} = \frac{1}{r} \frac{\partial}{\partial r} \left(D(c)r \frac{\partial c}{\partial r} \right). \quad (3.31)$$

$D(c)$ is an empirical relation, typically based on an exponential [69]

$$D(c) = D_0 \exp(ac) \quad (3.32)$$

or a power-law function [71]

$$D(c) = D_0 c^a, \quad (3.33)$$

where

- D_0 and a are coefficients.

The presence of nonsteady state boundary conditions requires a numerical approach in order to solve Eq. (3.31). The continuous process of matter transport is replaced by a stepwise one. In this context Vergnaud [72] proposes a finite difference model which divides the layer in a finite number of parallel and equally thick slices and allows evaluation of the concentration evolution at each slice-to-slice interface at constant time increments. If time and space are written in discrete form, i.e.,

$$\begin{aligned} t &= k\Delta t \\ r &= n\Delta r \end{aligned} \quad (3.34)$$

respectively, where Δt and Δr are the increments and k and n are integers, then $c_{n,k}$ is the diffusant concentration at the interface “plane” between slices n and $n+1$ at time t

$$c_{n,k} = c(r,t). \quad (3.35)$$

Using Fick's 1st law in radial direction,

$$J = -D(c) \frac{\partial c}{\partial r}, \quad (3.36)$$

where J is the diffusant flux, the matter balance in the Δr -thick control volume centred around "plane" n (grey in Figure 3.13) during a time increment becomes

$$(A_{n-0.5}J_{n-0.5} - A_{n+0.5}J_{n+0.5})\Delta t = A_n\Delta r(c_{n,k+1} - c_{n,k}), \quad (3.37)$$

where

- $A_{n-0.5} = 2\pi(n-0.5)\Delta r$

$$A_n = 2\pi n\Delta r$$

$$A_{n+0.5} = 2\pi(n+0.5)\Delta r$$

are the discrete expressions of the cross-sectional area of the control volume at positions $n-0.5$, n and $n+0.5$, and

- $J_{n-0.5} = -D_{n-0.5} \frac{c_{n,k} - c_{n-1,k}}{\Delta r}$

$$J_{n+0.5} = -D_{n+0.5} \frac{c_{n+1,k} - c_{n,k}}{\Delta r}$$

are the discrete expressions of the flux at positions $n-0.5$ and $n+0.5$.

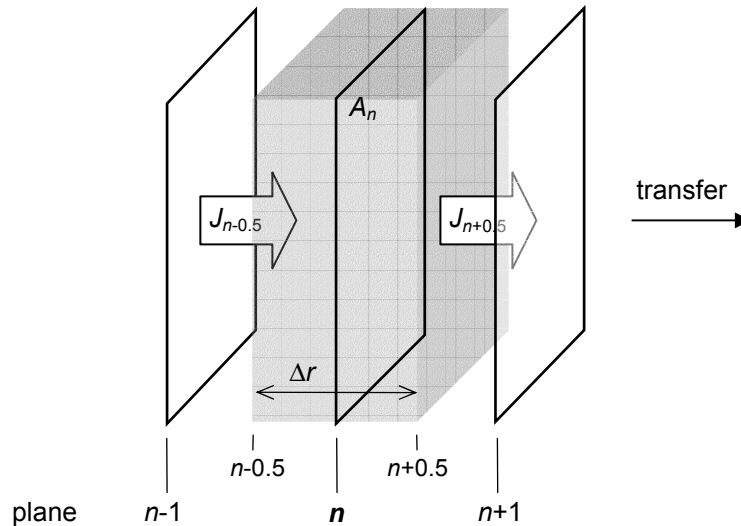


Figure 3.13 Matter balance in the finite difference diffusion model.

The discrete forms of $D(c)$ are

- $D_{n-0.5} = D_0 \exp\left(a \frac{c_{n-1,k} + c_{n,k}}{2}\right)$

$$D_{n+0.5} = D_0 \exp\left(a \frac{c_{n,k} + c_{n+1,k}}{2}\right)$$

for the exponential concentration dependence and

- $D_{n-0.5} = D_0 \left(\frac{c_{n-1,k} + c_{n,k}}{2}\right)^a$

$$D_{n+0.5} = D_0 \left(\frac{c_{n,k} + c_{n+1,k}}{2}\right)^a$$

for the power-law concentration dependence.

The new concentration at position n after an elapse of time Δt , $c_{n,k+1}$, and based upon the previous concentrations at positions $n-1$ and $n+1$, can be extracted from Eq. (3.37)

$$c_{n,k+1} = c_{n,k} + \frac{1}{M} (I_{n-0.5} - I_{n+0.5}), \quad (3.38)$$

where

- $I_{n-0.5} = \frac{n-0.5}{n} D_{n-0.5} (c_{n-1,k} - c_{n,k})$ and

$$I_{n+0.5} = \frac{n+0.5}{n} D_{n+0.5} (c_{n,k} - c_{n+1,k})$$

- $M = \frac{(\Delta r)^2}{\Delta t} \left(> \frac{n-0.5}{n} D_{n-0.5} + \frac{n+0.5}{n} D_{n+0.5} \right)$ is a dimensionless ratio.

If diffusivity does not depend on concentration, i.e., $D(c) = D$, Eq. (3.38) becomes

$$c_{n,k+1} = \frac{1}{M} \left(\frac{n-0.5}{n} c_{n-1,k} + (M-2)c_{n,k} + \frac{n+0.5}{n} c_{n+1,k} \right), \quad (3.39)$$

where

- $M = \frac{(\Delta r)^2}{D\Delta t} (> 2)$ is a dimensionless ratio.

We note that Δr and Δt can be chosen arbitrarily as long as M satisfies the indicated inequality. This condition is required in order to have a positive and non-zero contribution of the $c_{n,k}$ term in Eqs. (3.38) and (3.39). Smaller increments improve the model accuracy.

For the tubular coating layer, the initial and boundary conditions are expressed with time index $k = 0$ for the initial concentration and space index $n = 0$ for the surface concentration.

For the initial condition, the concentration in the entire layer is supposed to be uniform and equal to the surface concentration, $c_{ext}(t)$, i.e.,

$$\blacksquare c_{n,0} = c_{ext}(t = 0) \quad \text{for } n = N_i \text{ to } N_e. \quad (3.40)$$

The boundary conditions are given at the coating surface (external) and at the coating-fibre interface (internal),

$$\blacksquare c_{N_e,k} = c_{ext}(t = k\Delta t) \quad \text{for } k = 0 \text{ to } K \text{ and} \quad (3.41)$$

$$\blacksquare c_{N_i-1,k} = c_{N_i,k} \quad \text{for } k = 0 \text{ to } K \text{ respectively,} \quad (3.42)$$

where

- $N_i = a/\Delta r$,
- $N_e = b/\Delta r$ (a and b the fibre and coating outer radii respectively, as shown in Figure 3.12) and
- K is the number of considered time intervals.

Once the concentration distribution in the coating at time increment k is known, the normalised accumulated mass of diffusant which has entered (or left) the coating at this moment, M_k/M_K , can be calculated

$$\frac{M_k}{M_K} = \frac{C_k - C_0}{C_K - C_0}, \quad (3.43)$$

where

$$\blacksquare C_k = \sum_{n=N_i}^{N_e} c_{n,k}.$$

For water vapour diffusion, the surface concentration, c_{ext} , may be expressed as a function of the external relative humidity using the sorption isotherm. S being the solubility of vapour in the polymer matrix, the absorbed water concentration at equilibrium is

$$c_{ext} = Sp, \quad (3.44)$$

where

- $p = p_0 \frac{RH[\%]}{100}$ is the external partial vapour pressure

and p_0 is the saturation pressure of water. p_0 is a function of temperature as described by Clausius-Clapeyron's formula.

The permeability of the polymer matrix, P , is the product of diffusivity and solubility and is written as

$$P = DS. \quad (3.45)$$

If water vapour sorption in the diffusion layer obeys a purely Henry's law³, the sorption isotherms are linear, S does not depend on concentration and the surface concentration thus is proportional to the partial vapour pressure (or RH at constant temperature). In this case we may use the partial vapour pressure as surface concentration as it is, since any constant concentration proportionality factor is cancelled in Eq. (3.31).

The external boundary condition (Eq. (3.41)) also assumes an infinite evaporation / condensation rate, i.e., the water concentration at the coating surface reaches the concentration at equilibrium instantly. A more realistic model should consider the time required for the liquid to pass into the vapour phase or vice versa.

3.4.4 Discussion of diffusion models

Figure 3.14 shows the normalised accumulated mass of diffusant as a function of time following an abrupt concentration change (steady state boundary conditions), calculated for a plane (Eq. (3.27)) and a tubular layer (Eq. (3.30)). Characteristic polyimide coating properties were chosen, i.e., $D = 10^{-12} \text{ m}^2/\text{s}$ [73], $L = 50 \text{ }\mu\text{m}$ (plane layer), $a = 63.5 \text{ }\mu\text{m}$ and $b = 113.5 \text{ }\mu\text{m}$ (tubular layer). Comparing the two curves, we notice that the cylindrical layer saturates quicker than the plane layer. This difference is due to the smaller volume/surface ratio of the cylinder compared with the plane sheet.

³ At constant temperature, the mass of gas dissolved in a liquid at equilibrium is proportional to the partial pressure of the gas.

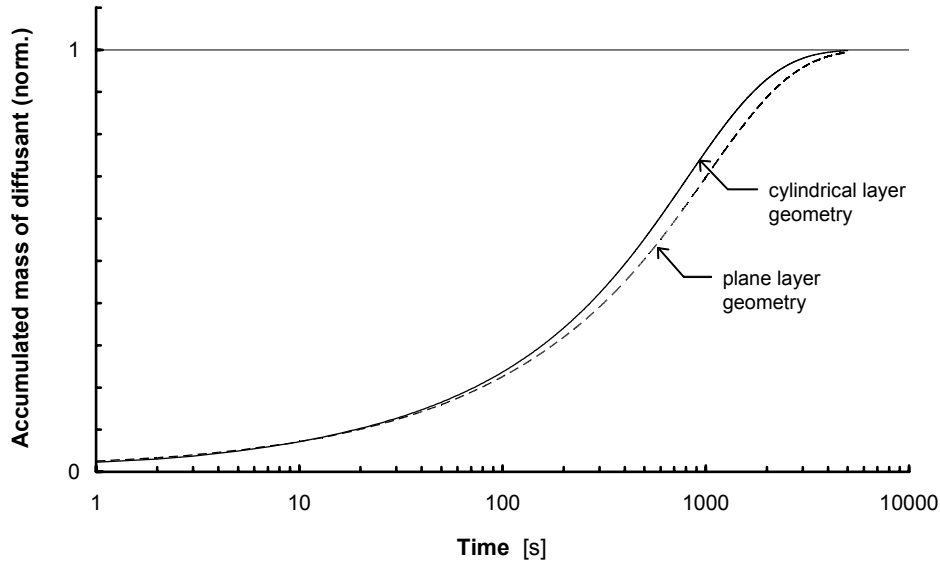


Figure 3.14 Normalised accumulated mass of diffusant as a function of time, calculated with the plane and the tubular diffusion model (steady state boundary conditions, $D = 10^{-12} \text{ m}^2/\text{s}$, layer thickness $50 \text{ }\mu\text{m}$).

Figure 3.15 shows the time required for a plane and a tubular layer to reach 95% saturation ($M_t/M_\infty = 0.95$) after an abrupt concentration change as a function of diffusivity (from 10^{-13} to $10^{-11} \text{ m}^2/\text{s}$). The layer geometries are the same as above. As expected, both layer geometries saturate quicker at higher diffusivities. For the considered diffusivity range, the plane layer requires up to 25% more time for saturation than the tubular layer. However, the percent deviation seems to decrease linearly with diffusivity.

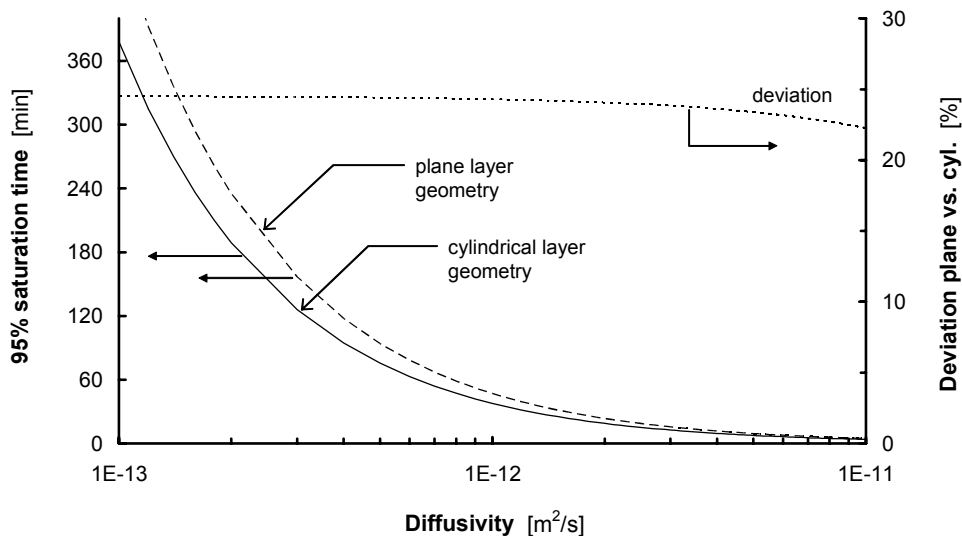


Figure 3.15 Time required for a plane and a tubular layer to reach 95% saturation as a function of diffusivity (steady state boundary conditions, layer thickness $50 \text{ }\mu\text{m}$). The dotted curve is the percent deviation between the plane and the cylindrical model.

Figure 3.16 shows the time required for a plane and a tubular layer to reach 95% saturation after an abrupt concentration change as a function of layer thickness (from 0 to 100 μm). The diffusivity and inner radius of the tubular layer are kept constant, i.e., $D = 10^{-12} \text{ m}^2/\text{s}$ and $a = 63.5 \mu\text{m}$. As expected and for both layer geometries, the saturation time tends to zero for zero layer thickness and increases exponentially with the layer thickness. For the considered thickness range, the plane layer requires up to 40% more time for saturation than the tubular layer. The percent deviation escalates for thicker layers.

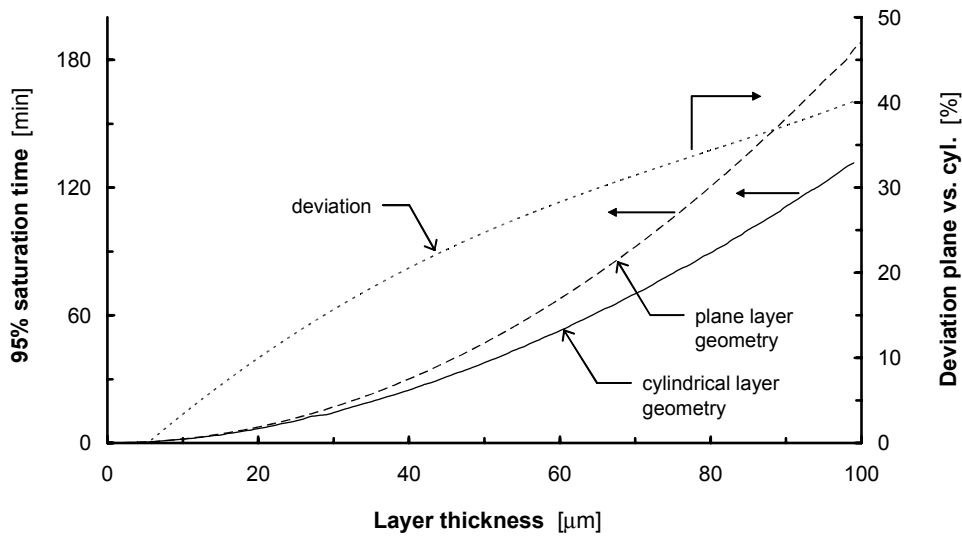


Figure 3.16 Time required for a plane and a tubular layer to reach 95% saturation as a function of layer thickness (steady state boundary conditions, $D = 10^{-12} \text{ m}^2/\text{s}$). The dotted curve is the percent deviation between the plane and the cylindrical model.

The deviation between the saturation times calculated with the plane layer and the cylindrical layer model is significant. The plane layer model overestimates the time required for the fibre coating to saturate. Therefore the use of the cylindrical model is indicated for describing the diffusion in the fibre coating.

3.5 Fibre Bragg grating humidity sensor

The fibre optic intracore Bragg grating sensor, henceforth called FBG sensor, relies on the narrowband reflection from a region of permanent periodic variation in the core refractive index, called Bragg grating, of an optical fibre [74]. The grating structure is written into the core of an optical fibre using holographic techniques or a phase mask. When a broadband light is injected into the fibre, the index-varying structure reflects by constructive interference the narrowband spectral component (the Bragg wavelength) which satisfies the resonance condition of the grating. The resonance condition depends on the modulation period of the core index of refraction, Λ , and on the index of refraction. A schematic representation of a FBG is given in Figure 3.17.

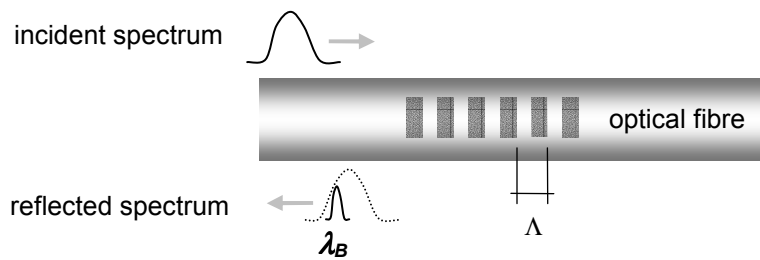


Figure 3.17 Scheme of an optical fibre Bragg grating.

The modulated parameter of a FBG is the centre wavelength of the reflected spectrum, called Bragg wavelength, λ_B , and is written as [41]

$$\lambda_B \equiv 2n_{eff}\Lambda . \quad (3.46)$$

We note that the modulated mechanical parameter in Eq. (3.46) is no longer L as it was for the sensor optical path length expressed in Eq. (3.1), but Λ . For the index of refraction the value of the effective index, n_{eff} , is used. The derivatives of Λ with respect to T and ε_z , however, remain identical to those of L with respect to T and ε_z . According to Eq. (3.8), a change in axial strain and temperature will result in a relative Bragg wavelength shift,

$$\frac{\Delta\lambda_B}{\lambda_B} = (1 - \hat{p}_e)\Delta\varepsilon_z + (\alpha_f + \xi)\Delta T . \quad (3.47)$$

The FBG sensor is wavelength encoded and thus insensitive to light intensity variations, typically due to instabilities of the source power and the photodetector response or due to losses in the fibre (connectors, macrobends). Wavelength encoding also provides a convenient and simple method of multiplexing.

The FBG is made humidity sensitive by coating the region of the fibre where the FBG is located with the hygroscopic transducer material. The coating procedure is described in 4.3.2.2. According to the general expression of the relative sensor optical path length change given in Eq. (3.11), the relative Bragg wavelength shift of a hygroscopically recoated FBG due to ΔRH and ΔT is expressed as a linear superposition of a relative humidity and a temperature term

$$\frac{\Delta \lambda_B}{\lambda_B} = S_{FBG,RH} \Delta RH + S_{FBG,T} \Delta T, \quad (3.48)$$

where the FBG sensor sensitivities are identical to the fundamental form expressed in Eqs. (3.12) and (3.13), i.e.,

$$S_{FBG,RH} = S_{RH} = \beta_{cf} - \hat{p}_e \beta_{cf} \quad (3.49)$$

and

$$S_{FBG,T} = S_T = \alpha_{cf} - \hat{p}_e (\alpha_{cf} - \alpha_f) + \xi. \quad (3.50)$$

The FBG humidity sensor sensitivities can be altered by using a different coating material or by modifying the sensor section geometry, i.e., the fibre diameter and / or the coating thickness (see 3.3.3). Varying the grating length or Λ does not affect the sensitivities. Longer gratings however lead to a narrower bandwidth of the reflected spectrum which can be demodulated more accurately.

3.6 Michelson interferometric fibre optic humidity sensor

The Michelson interferometric fibre optic humidity sensor, henceforth called SOFO⁴ humidity sensor due to its similarity with the SOFO deformation sensor [77], consists of a pair of colocated single-mode optical fibres that are connected at one end by a 3 dB-coupler to the reading unit and terminated by mirrors at the opposite, free ends, as shown in Figure 3.18.

⁴ SOFO is the French acronym for “Surveillance des Ouvrages par Fibre Optique” (structural monitoring using fibre optics). The SOFO term has its origin in a research program which started at the IMAC laboratory in 1993 and focuses on the development and application of fibre optic sensing tools for structural monitoring.

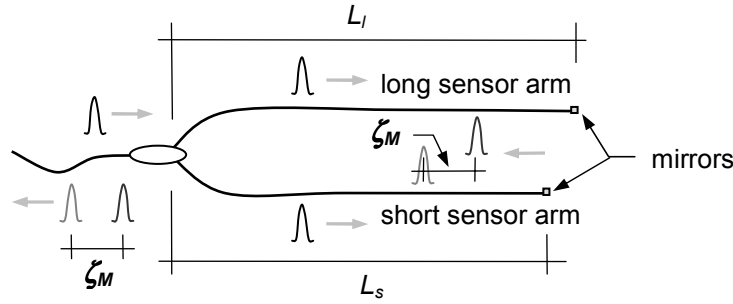


Figure 3.18 Michelson interferometric fibre optic sensor (SOFO sensor).

The measured parameter is the sensor optical path length unbalance, ζ_M , between the two sensor arms

$$\zeta_M \equiv 2(\zeta_{L,l} - \zeta_{L,s}), \quad (3.51)$$

where

- $\zeta_{L,i} = n_g L_i$ are the optical path lengths of the long ($i = l$) and the short sensor arm ($i = s$). For the index of refraction the value of the group index, n_g , is used.
- L_i is the arm length (measured from the coupler to the mirrored ends).

The sensor arms are identified by their optical path lengths (long arm, short arm) rather than by their function (sensing arm, reference arm), common for Michelson interferometric fibre optic sensors. The latter convention may lead to confusion because it does not consider whether the sensing arm is longer or shorter than the reference arm. For instance, the sensor response is inverted (i.e., negative sensitivity) if the sensing arm is shorter than the reference arm. The index of refraction is uniform because both sensor arms use the same type of fibre and are isothermal. The factor of 2 in Eq. (3.51) is because the lightwave travels back and forth. The SOFO sensor uses phase encoding and thus features the same insensitivity to light intensity variations as does the FBG sensor.

The measurand induced shift of the sensor optical path length unbalance, $\Delta\zeta_M$, is a function of the individual sensor arms' optical path length variation, $\Delta\zeta_{L,i}$,

$$\Delta\zeta_M = 2(\Delta\zeta_{L,l} - \Delta\zeta_{L,s}). \quad (3.52)$$

For the SOFO sensor to be humidity sensitive, the two sensor arms must exhibit a different RH-sensitivity. This can be realised by using a hygroscopically coated fibre for one sensor arm and a bare fibre for the other arm. Alternatively, the bare fibre may be replaced by a fibre with a non-hygroscopic coating, such as a metallic coating (e.g., gold, silver, copper, zinc). Analogous to the fundamental expression of the relative

shift of the sensor optical path length presented in Eq. (3.11), the relative shift of the sensor optical path length unbalance, $\Delta\zeta_M/\zeta_L$, due to ΔRH and ΔT is written as,

$$\frac{\Delta\zeta_M}{\zeta_L} = S_{SOFO,RH}\Delta RH + S_{SOFO,T}\Delta T, \quad (3.53)$$

where

- $\zeta_L = n_g L$ is the mean sensor optical path length of the sensor arms ($L = (L_l + L_s)/2$) and
- $S_{SOFO,RH}$ and $S_{SOFO,T}$ are the SOFO sensor RH- and T-sensitivities respectively.

Using Eqs. (3.11) and (3.52), the SOFO sensor sensitivities can be expressed as a function of the individual sensor arm sensitivities, $S_{RH,i}$, and $S_{T,i}$,

$$S_{SOFO,RH} = 2 \left(\frac{\zeta_{L,l}}{\zeta_L} S_{RH,l} - \frac{\zeta_{L,s}}{\zeta_L} S_{RH,s} \right) \quad (3.54)$$

and

$$S_{SOFO,T} = 2 \left(\frac{\zeta_{L,l}}{\zeta_L} S_{T,l} - \frac{\zeta_{L,s}}{\zeta_L} S_{T,s} \right) \quad (3.55)$$

or, in a more explicit form according to Eqs. (3.12) and (3.13),

$$S_{SOFO,RH} = 2 \left(\frac{L_l}{L} \beta_{cf,l} (1 - \hat{p}_{e,l}) - \frac{L_s}{L} \beta_{cf,s} (1 - \hat{p}_{e,s}) \right) \quad (3.56)$$

and

$$S_{SOFO,T} = 2 \left(\frac{L_l}{L} (\alpha_{cf,l} - \hat{p}_{e,l} (\alpha_{cf,l} - \alpha_f) + \zeta) - \frac{L_s}{L} (\alpha_{cf,s} - \hat{p}_{e,s} (\alpha_{cf,s} - \alpha_f) + \zeta) \right), \quad (3.57)$$

where α_f and ζ can be considered to be uniform because the sensor arms use the same type of fibre and are assumed to be isothermal.

The SOFO sensor sensitivities depend directly on the sensitivity difference between the sensor arms. If the sensitivity of the short arm is set to zero, the maximum SOFO sensitivity obtained is twice the arm-length weighted sensitivity of the long arm, $S_{SOFO,RH}^{\max} = 2S_{RH,l}L_l/L$ and $S_{SOFO,T}^{\max} = 2S_{T,l}L_l/L$. Due to the permanent T-sensitivity inherent to optical fibres, this limit value may however only be reached for the RH-sensitivity. As we will see in 4.7, the arm-to-sensor length proportion, L_l/L , is a particularly useful parameter for temperature compensation.

3.7 Concluding remarks

The steady state relative humidity response of a hygroscopically coated optical fibre can be expressed analogously to the temperature response, except for the thermo-optical effect which is inexistent.

The analytical and the numerical (finite element) models that describe the mechanical behaviour of the coated fibre for a thermal and a hygroscopic load are in agreement. Compared with the 3-D model, the 1-D axial model underestimates the fibre deformation significantly. The more complex 3-D model should be used for thin coatings and for the hygroscopic load case, where the deviation between the models is particularly high.

The RH- and T-sensitivities of the coated fibre depend on the coating thickness. Thicker coatings increase the sensitivities. The deviation between the sensitivities calculated with the 1-D and the 3-D model is still present, although it is attenuated compared to the deviation obtained for the mechanical behaviour. The use of a 3-D approach is particularly important for determining the RH-sensitivity of fibres with thin coatings.

The transient state saturation time increases for thicker coatings and for lower diffusivities. The layer geometry of the diffusion model also influences the saturation time. The plane layer may require significantly more time to saturate than the tubular layer. In order to accurately describe the diffusion in the fibre coating the tubular layer model should be used.

A short gauge humidity sensor can be realised by coating a fibre Bragg grating with the hygroscopically swelling transducer polymer. For a long gauge humidity sensor, the two sensor arms of a Michelson interferometer (SOFO sensor) must have different RH-sensitivities (e.g., one arm with, the other one without coating).

4. Sensor designs and characterisation

4.1 Requirements

The humidity sensors that are developed in this work should meet several metrological and environmental requirements. These requirements are characteristic for non-destructive monitoring of construction materials in common laboratory and in-situ environments.

Measurement range: 10 to 100 %RH. As seen in 2.2, the relative humidity in construction materials may cover almost the entire range. In concrete, chemical degradation processes typically are limited to an RH between 40 and 95 %RH, while the curing rate is RH-sensitive between 80 and 95 %RH. In timber, biological degradation processes occur in general at RH levels close to 100 %RH, while its mechanical properties are RH-sensitive over the whole RH range. Relative humidity below 30 %RH is rarely encountered in outdoor environments, but it may occur under laboratory conditions (e.g., during drying experiments).

Operating temperature: -20 to 105 °C. This range includes seasonal temperature variations as well as temperature increases due to exothermic chemical reactions inside the material, such as hydration of concrete. If used for drying experiments, the sensors should remain operational up to 105 °C.

Measurement accuracy: ± 3 %RH under steady state conditions (average ± 5 %RH under transient state conditions). This accuracy should allow for the determination of the moisture content of construction materials with adequate accuracy. For example in concrete, the slope of the sorption isotherms is typically 0.1 wt% between 60 and 90 %RH [3]. Thus the suggested RH accuracy allows measurement of water content with an accuracy of 0.3 wt%. This is better than what is possible with the gravimetric reference method (see 2.3.1). The smaller accuracy under transient state conditions accounts for the deviation due to the sensor response delay.

Response time: depends on the accepted deviation and on the rate of moisture variation at the sensor location.

Environmental compatibility. Sensors should withstand the conditions typically encountered in construction environments. Potentially harmful influences are humidity, salinity, alkalinity and electromagnetic interference.

Durability: long term (> 10 years). One of the objectives of this work is to support the continuous health monitoring of construction materials. Since this is a task that is carried out over several years, sensors should provide a stable response over a decade at least.

Impact on the host material: as small as possible. Sensors must be able to provide non-destructive measurements. Small sensors reduce the disturbing impact on host materials. The use of large, invasive sensors may locally disturb the natural moisture equilibrium and hence lead to non-representative measurements. Also they can alter other processes which depend on the mechanical integrity of the investigated material (e.g., ion and gas permeation).

Spatial resolution: as versatile as possible. Depending on the size and type of structure and on the phenomena under investigation, sensors should be able to make local point measurements as well as long base measurements that average the RH over the measurement zone. Moisture profile assessment is an example where a good in-depth resolution of point measurements is desired.

Sensors should be able to be integrated within existing fibre optic sensor networks. To facilitate the integration of new sensors in existing structural monitoring networks, they should rely on established fibre optic sensor technologies.

4.2 Transducer coating

Water immersion tests with a fibre optic Michelson interferometer set up with polyimide coated fibres revealed the hygroscopic swelling capacity of polyimide polymers. Polyimide coated fibres are commonly used for high temperature sensing and telecom applications and for applications where a good strain transfer between the host and the fibre is required, such as in fibre optic strain sensors.

To explain the swelling behaviour of polyimides, two physico-chemical mechanisms have been suggested [69]:

- Capillary condensation of water in cavities inside the layer or
- Chemical and polar bonding of OH⁻ and water molecules at unsaturated bonds of the polymer chains.

Chemical sorption is assumed to be the main reason for the observed swelling.

The steady and transient state hygroscopic swelling behaviour of polyimides depends on many characteristic polymer properties (i.e., stiffness of polymer chains, hydrophily, degree of imidizing / chain orientation, cured thickness / shrinkage, packing density / porosity), which themselves vary depending on polyimide type, deposition and curing process. Therefore, it is difficult to compare polyimides with different origins among each other.

For this work, polyimides have been selected as transducer material because:

- They swell hygroscopically.
- Polyimide coatings are known to adhere well to optical fibres.
- They have a glass transition temperature, T_g , that is substantially higher than the operating temperature range of the sensor mentioned in 4.1 ($T_g > 320$ °C for Pyralin [68]). Therefore the mechanical properties may be assumed to remain constant and the polymer relaxation rate is generally smaller or similar to the moisture diffusion rate (case II or III diffusion).

Hot strong acids (such as H₂SO₄ at 120 °C) dissolve polyimides. Exposure to alkaline solutions over several months revealed signs of degradation of polyimide coatings [75]. In the context of the present study these issues are however not relevant as the polyimide is intended to be exposed only to a gaseous, neutral environment.

4.3 FBG sensor

4.3.1 Sensor operation and interrogation

As explained in 3.5, a fibre Bragg grating is a permanent periodically index-varying structure written into the core of a silica fibre. When a broadband light is injected into the fibre, the index-varying structure reflects the narrowband spectral component (the Bragg wavelength) which satisfies the resonance condition of the grating. In the transmitted light, the spectral component corresponding to the Bragg wavelength is missing, as illustrated in Figure 4.1. The bandwidth of the Bragg spectrum depends on

several parameters, particularly the grating length. It typically is 0.05 to 0.3 nm for sensor applications [45].

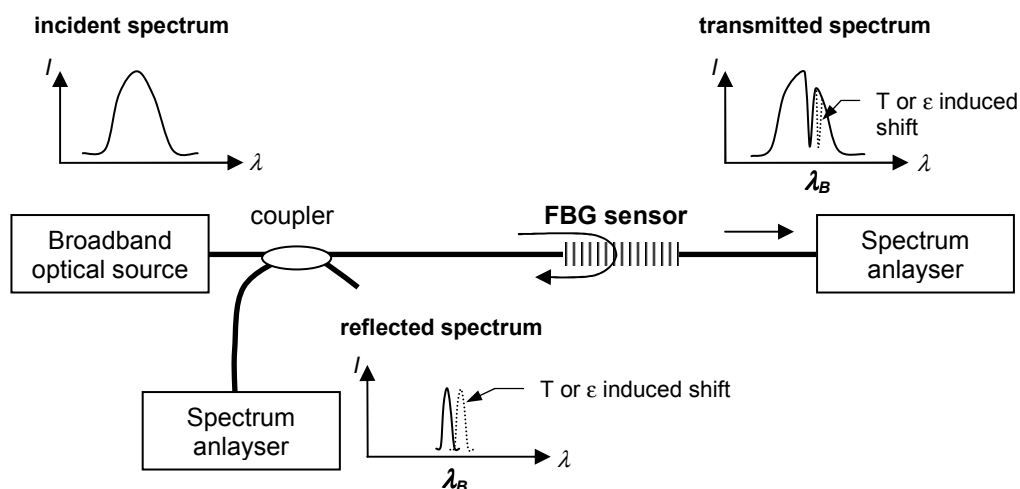


Figure 4.1 Fibre Bragg grating based sensor system with transmissive and reflective detection.

Figure 4.2 shows a typical FBG reflection spectrum.

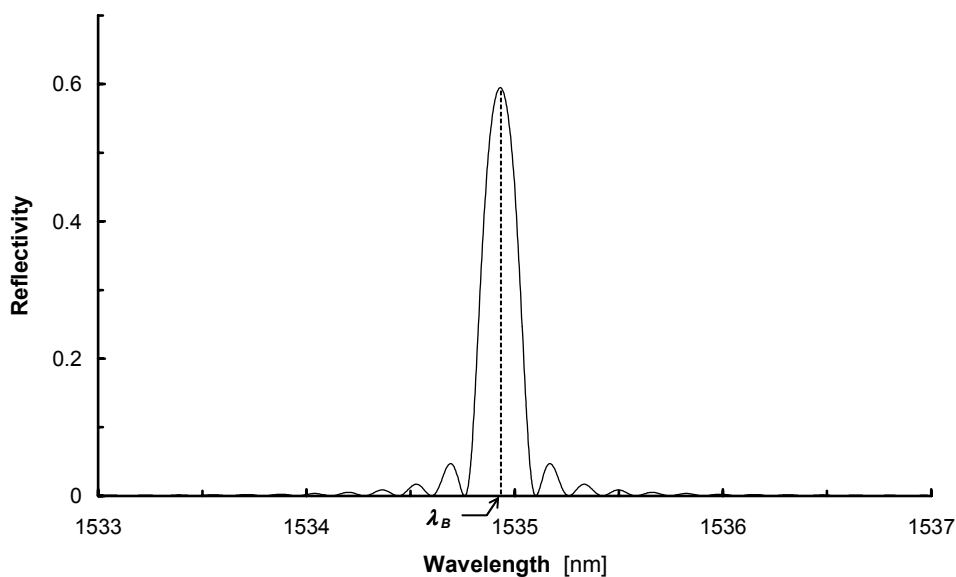


Figure 4.2 Typical reflection spectrum of a FBG (courtesy of Ph. Giaccari, IOA / EPFL).

In this work, all FBG sensors were interrogated in reflective mode using either a tunable laser or a fibre Fabry-Perot tunable filter. The operating wavelength was 1550 nm.

Tunable laser

With this technique the wavelength of a laser source is continuously tunable in order to scan the potential Bragg wavelength range. When the laser wavelength satisfies the

Bragg condition, the light is reflected and detected at the photodetector, thereby allowing determination of the Bragg wavelength by the wavelength of the source.

Although tunable lasers feature an enhanced signal-to-noise ratio, their limited scanning speed is not appropriate for high speed sampling. For the tunable laser, we used a Tunic 1550 from Photonetics Inc., which resolves wavelengths down to 1 pm and achieves a wavelength accuracy of ± 5 pm. For device control and data acquisition a GPIB interface from National Instruments and LabVIEW routines were used. All equipment was from the Laboratory of Applied Optics (IOA) at EPFL and the LabVIEW routines were implemented by Ph. Giaccari.

Fibre Fabry-Perot tunable filter

This interrogation technique is based on a tunable passband filter which tracks the FBG signal. When the filter window overlaps the reflected Bragg wavelength, the light is passed on to the detector. A broadband LED is used as source. The wavelength value is obtained by comparing the filter position with a well-known and stable narrowband source.

The fibre Fabry-Perot tunable filter used in this work is the Fibre Bragg Grating Interrogation System (FBG-IS) from Micron Optics Inc. This system resolves wavelengths down to 1 pm and achieves a calibrated wavelength accuracy of ± 5 pm. The FBG-IS simultaneously demodulates up to 30 FBGs at a sampling rate of 50 Hz. A digital acquisition card from National Instruments (DAQCard-DIO-24) serves as computer interface and LabVIEW routines process and display data.

Characteristics of the two interrogation systems are listed in Table 4.1.

	Tunable laser	Fibre Fabry-Perot tunable filter
Model	Tunic 1550	FBG-IS 1550-110-FCS (v3.3)
Manufacturer	Photonetics Inc., US	Micron Optics Inc., US
Wavelength range	1480 – 1580 nm	1530 – 1570 nm
Resolution	1 pm	1 pm
Accuracy	± 5 pm	± 5 pm
Max. number of gratings to be read together	≈ 100	30
Max. sampling rate	1 Hz	50 Hz
PC interface	IEEE-488.1 (GPIB) (National Instruments)	DAQCard-DIO-24 (National Instruments)
Software	LabVIEW	LabVIEW
Portability	No	Yes
Price	$\approx \$60'000$	$\$18'000$

Table 4.1 Characteristics of the used FBG demodulation systems.

In this work, FBGs were multiplexed serially using wavelength division (WDM). A detailed presentation of multiplexing methods and network topologies for FBG sensors is given by Morey et al. [76].

4.3.2 Sensor design

The FBG sensors used in this work are of two different origins. Some were commercially produced by Innovative Fibers Inc., and others were entirely self-made. The Innovative Fibers gratings have a centre wavelength of 1550 nm and are specified with 0.2 nm bandwidth and 90% reflectivity. The fibre is SMF-28 type. Unfortunately, no information could be obtained regarding the recoating process and the type of polyimide used.

For the self-made sensors, the following two sections illustrate the processes involved in the fabrication of an FBG and its recoating.

A list of all FBG sensors is given in Table 4.2.

FBG	Origin	S/N	Fibre	Coating	
				Material	Avg. thickness
1	IOA / IMAC	IOA-0	SMF-28	none	0 μm
2	IOA / IMAC	IOA-1	SMF-28	Pyralin	3.5 \pm 1 μm
3	IOA / IMAC	IOA-4	SMF-28	Pyralin	6.6 \pm 1 μm
4	IOA / IMAC	IOA-9	SMF-28	Pyralin	11.8 \pm 1 μm
5	IOA / IMAC	IOA-5	SMF-28	Pyralin	18.7 \pm 1 μm
6	IOA / IMAC	IOA-3	SMF-28	Pyralin	21.3 \pm 1 μm
7	IOA / IMAC	IOA-8	SMF-28	Pyralin	27.3 \pm 1 μm
8	IOA / IMAC	IOA-6	SMF-28	Pyralin	29.3 \pm 1 μm
9	Innovative Fibers	BRR-8548-1-25	SMF-28	(Polyimide)	33.0 \pm 1 μm
10	Innovative Fibers	BRR-8548-1-28	SMF-28	(Polyimide)	36.5 \pm 1 μm
11	Innovative Fibers	BRR-8548-1-27	SMF-28	(Polyimide)	50 \pm 1 μm

Table 4.2 Description of FBG sensors. The coating thickness is measured by microscope.

4.3.2.1 Grating fabrication

The gratings were written using a phase mask, which is illuminated through a lens system by an excimer laser. The laser emits in the ultraviolet wavelength range ($\lambda = 193$ nm). In order to be able to write gratings into the optical fibre core, the fibre must be photosensitive at the wavelength used for writing. Germanosilicate fibres, which exhibit a natural photosensitivity, are ideal candidates for this purpose. For small GeO_2 doping levels, the photosensitivity must be enhanced by charging the fibre with hydrogen (typical exposure rate: 8 days at 150 bar and ambient temperature).

A special writing setup was used to tune the Bragg wavelength without the need to change the phase mask. It includes two more lenses which produce a horizontally (i.e., in the sense of the fibre) diverging laser beam at the phase mask (Figure 4.3). With this configuration, the modulation period of the grating, i.e., the Bragg wavelength, can be shifted by moving the phase mask forwards or backwards (Figure 4.4). The achieved tuning range is from -10 nm to +10 nm around the nominal wavelength. FBGs with different wavelengths can be easily multiplexed using wavelength division multiplexing.

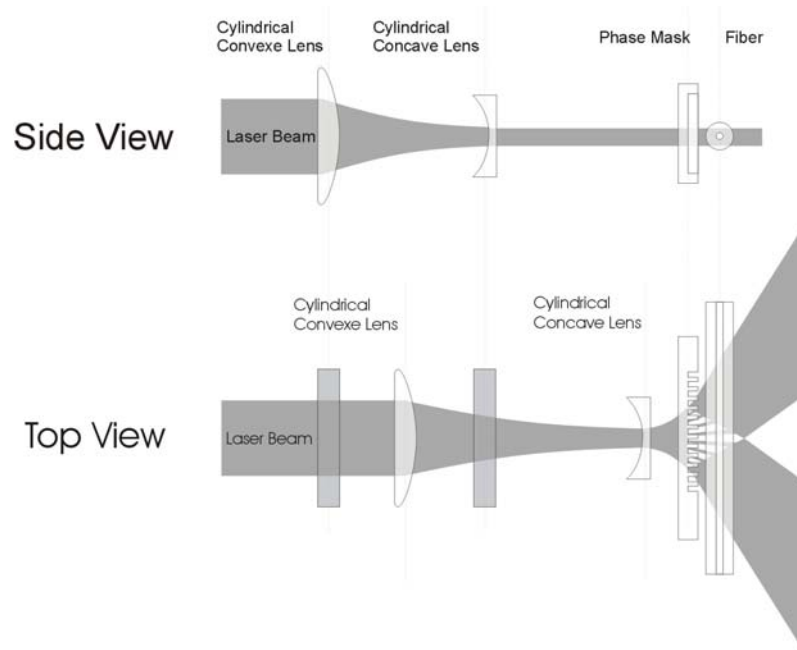


Figure 4.3 Writing setup with wavelength tuning option (courtesy of Ph. Giaccari, IOA / EPFL).

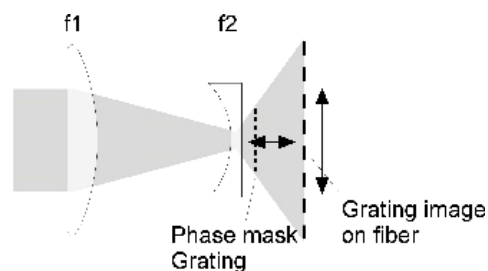


Figure 4.4 Wavelength tuning principle (courtesy of Ph. Giaccari, IOA / EPFL).

The FBGs used in this work were written in the 1.55 μm wavelength band using standard SMF-28 type fibres and they exhibited a typical reflectivity of 70% and bandwidth of 0.3 nm. The grating length was approximately 5 mm. All gratings were fabricated by Ph. Giaccari (IOA / EPFL).

4.3.2.2 Recoating

The recoating was performed with a Vytran PTR-100 optical fibre recoater. This machine is equipped with an ultra-violet (UV) lamp for curing the acrylate coating material which is commonly used for recoating (acrylate coating material is UV-curable). As in this application, the coating material is polyimide and polyimides are normally not UV-curable, an important challenge was to find a polyimide polymer containing a UV-curable component. Pyralin from HD MicroSystems GmbH is such a polyimide [68]. Pyralin is available at several viscosities, depending on the amount of solvent. We used the highly viscose Pyralin PI 2525 (viscosity ≈ 60 Poise) in order to maximize the coating gain per coating cycle.

To prepare the recoating, the fibre is placed in the quartz recoat mould assembly such that the part with the FBG lies in the middle of the mould (Figure 4.5). Next the recoat top and the holding fixtures on either side of the mould assembly are closed to keep the fibre in position. Now the liquid Pyralin is injected with a syringe through the injection plunger into the mould cavity. While injecting, care must be taken so as not to inject air bubbles. The viewport can be used to control the homogeneity of the injected recoating material. Finally the UV lamp is switched on for three minutes, turning the Pyralin to a soft, gelatinous state. After the UV irradiation, the fibre is carefully removed from the mould assembly and put in an oven to be heat cured at 200 °C for two hours. This converts the polyamic acid precursor to the insoluble and hard imide form. For this imidization process, a minimum temperature of 180 °C is required. Ideally, the curing temperature should be at least as high as the temperature to which the polyimide is going to be exposed later on in order to avoid outgassing of residual solvent vapours. The temperature ramp rate must not exceed the values specified by the manufacturer.

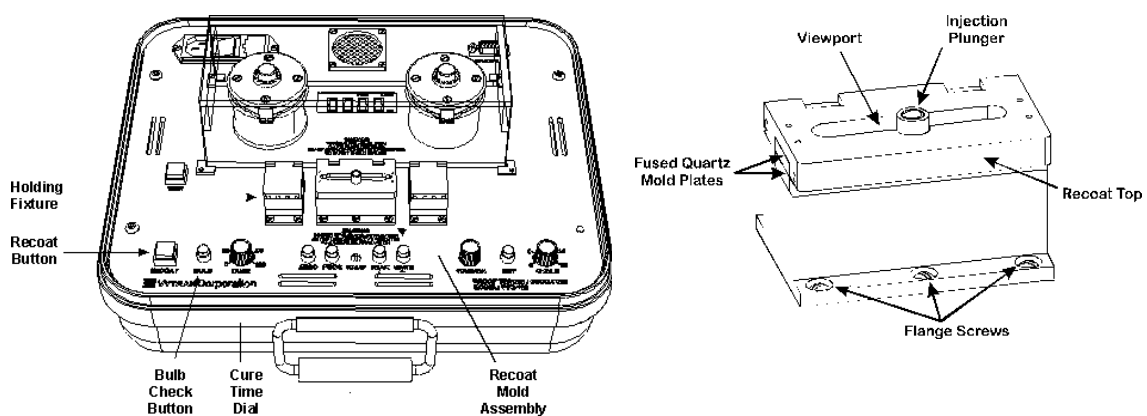


Figure 4.5 Vytran PTR-100 recoater (courtesy of Vytran Inc.).

Despite a recoat mould diameter of 260 μm , one coat adds only approximately 3 μm of coating layer. This is due to the high shrinkage of polyimide during the heat cure. For thicker coating layers, the coating procedure described above has to be repeated.

The final recoating thickness is measured by microscope. Due to the non-homogeneity of the recoating layer and the measurement uncertainty, the specified average thickness value exhibits an uncertainty of $\pm 1 \mu\text{m}$. Figure 4.6 illustrates a recoated fibre Bragg grating.

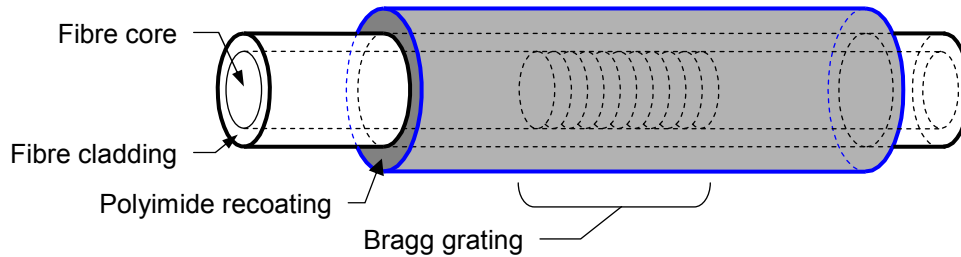


Figure 4.6 Recoated optical fibre Bragg grating (not to scale).

4.4 SOFO sensor

4.4.1 Sensor operation and interrogation

The SOFO measurement system is based on low-coherence interferometry in tandem configuration. One interferometer is the sensor; the other one is the analyser, as illustrated in Figure 4.7.

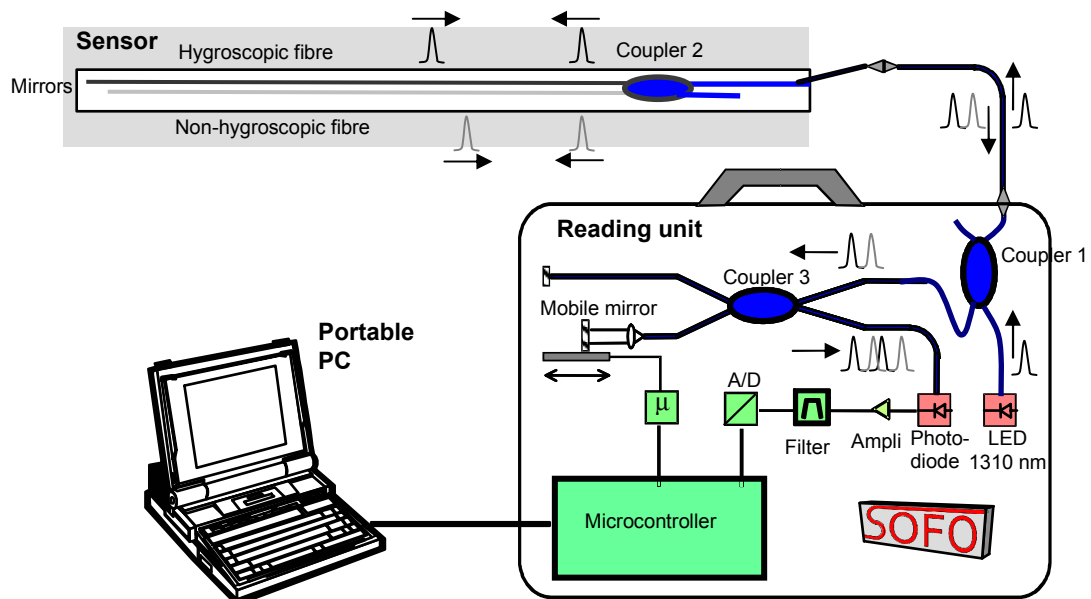


Figure 4.7 SOFO measurement system (adapted from [77]).

The infrared radiation of a light emitting diode (LED) is injected into a standard single mode fibre and directed, through coupler 1 (3 dB) in the reading unit and coupler 2 (3 dB) in the sensor, towards the two fibres acting as sensor. One of the fibres is hygroscopic (polyimide coated), the other one is hygroscopically inert (e.g., bare). Both fibres must be mechanically independent of the host material and installed side by side such as to undergo similar temperature fluctuations. Mirrors, deposited chemically (immersion in silver nitrate solution) at the end of each fibre, reflect the light back to coupler 2 which recombines the two beams and directs them through coupler 1 towards the analyser. The analyser is a Michelson interferometer with the end mirror of one arm installed on a translation stage, enabling introduction of a well known optical path length unbalance between the arms by mirror translation. On moving this mirror, a modulated signal is obtained on the photodiode only when the difference between the optical path length unbalances of the sensor and the analyser is smaller than the coherence length of the source (in our case some hundredths of mm). Using special signal processing routines [77], the demodulation resolution of the reading unit achieves less than 5 μm . Figure 4.8 shows a typical interference response as a function of the mirror position.

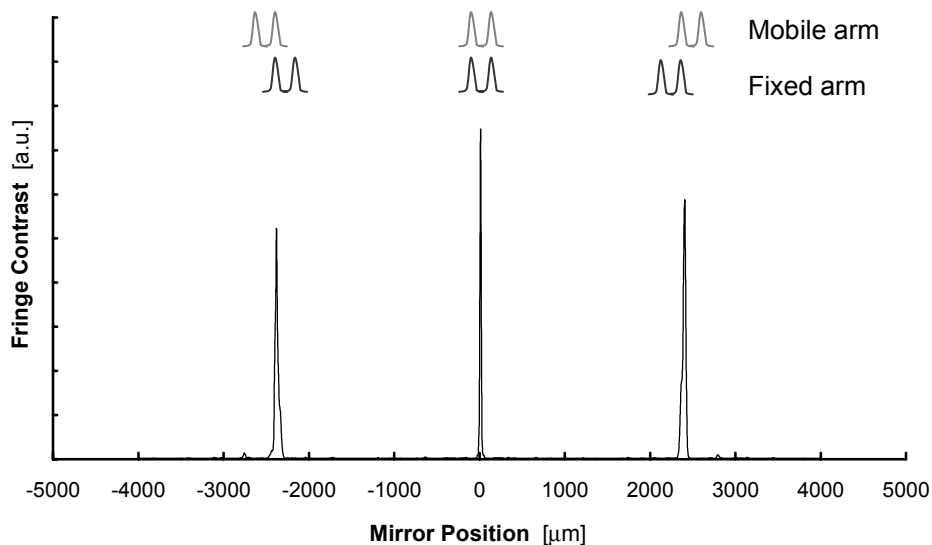


Figure 4.8 Fringe contrast at the photodetector as a function of the mirror position (from [77]).

Each measurement gives a new compensation position reflecting the relative humidity and temperature at the sensor.

The used SOFO reading unit was a SOFO V from Smartec SA. Its specifications are listed in Table 4.3.

Model	SOFO V
Manufacturer	Smartec SA, Switzerland
Operating wavelength	1310 nm
Coherence length	40 μm
Resolution of optical path length unbalance	4.7 μm
Deviation from linearity	< 0.2%
Max. optical path length unbalance	≈ 16.8 cm
Max. number of sensors to be read together	2
Measurement time per sensor	≈ 10 s
PC interface	RS 232
Software	SOFO DB
Portability	Yes (battery powered)
Price	\approx SFr. 50'000

Table 4.3 Specifications of the SOFO reading unit.

The SOFO software provides the sensor optical path length unbalance in terms of the light flight time delay between the two sensor arms, t . The following formula is used to translate this value into the sensor optical path length unbalance

$$\zeta_M = tc, \quad (4.1)$$

where $c = 3 \cdot 10^8$ m/s is the speed of light in vacuum.

The SOFO sensors in this work were multiplexed in a parallel network topology using an optical switch. A detailed presentation of multiplexing methods and network topologies for SOFO sensors is given by Inaudi [77].

4.4.2 Sensor design

To setup a SOFO RH-sensor, a polyimide coated and a bare fibre are each spliced to one of the output arms of a 3 dB-coupler. On the input side of the coupler a connected lead-in fibre is spliced to one of the arms. The remaining input arm is left free. The polyimide coated fibre is a SMT1310J from Spectran Inc. (coating thickness 14 μm). No specifications on the type of polyimide or the curing process are available. The bare fibre is an acrylate coated fibre, where the coating had been chemically removed by immersing the fibre in hot sulphuric acid. The bare fibre diameter is 127 μm . Bare

fibres are fragile and thus very delicate to handle. For this reason non-hygroscopic coatings, such as metallic coatings (e.g., gold, silver, copper, zinc), present an interesting, albeit costlier alternative for the humidity insensitive sensor arm. After having mirrored the sensor arms by depositing chemical mirrors on the cleaved fibre ends (dipping in silver nitrate solution, see [77]), the sensor is operational.

The lengths of the sensor arms must be chosen such that the optical path length unbalance between the two arms (from coupler to mirror) does not exceed the value specified for the reading unit, $\zeta_{M,max}$. Eq. (3.51) can be used to determine the maximum allowable length difference, $\Delta L (= L_l - L_s)$, between the fibres:

$$\Delta L < \frac{\zeta_{M,max}}{2n_g} \quad (4.2)$$

With $\zeta_{M,max} = 16.8$ cm (see Table 4.3) and $n_g = 1.450$ (for $\lambda = 1.3$ μm , see Table 3.1), $\Delta L < 5.8$ cm. The expected dynamic range of the sensor must also be considered when defining the arm length difference (longer sensors have larger dynamic ranges).

In order to avoid parasite effects due to the coatings of the coupler output fibres (generally acrylate), it is important to cut them to equal lengths before splicing the polyimide coated and bare fibres.

The SOFO RH-sensor, which will be characterised in 4.5.2, had the following specifications (see Figure 4.9):

- Polyimide coated sensor arm: $L_l = 114.5$ cm,
- Bare sensor arm: $L_s = 111.5$ cm,

thus $\Delta L = 3$ cm (< 5.8 cm).

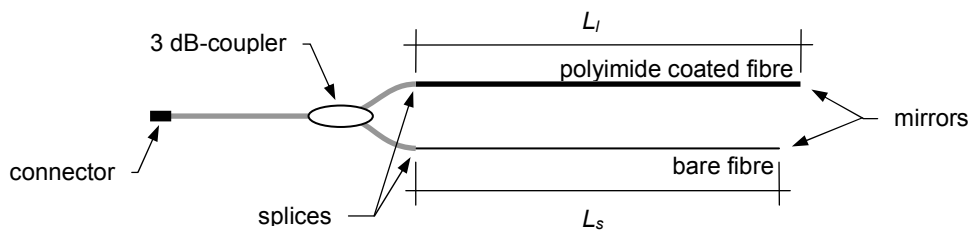


Figure 4.9 SOFO RH-sensor.

4.5 Steady state sensor response

4.5.1 FBG sensor

Note: Part of the experimental work on the FBG sensor presented hereafter was published in Optics Letters [78].

4.5.1.1 Experimental setup

The FBG sensor's response to RH and T was measured experimentally in a computer controlled climatic chamber (Vötsch VCL 4100 MH). Figure 4.10 shows the experimental setup with a linearly spliced array of seven recoated and one bare gratings interrogated with the FBG-IS. For reference monitoring, a calibrated, industry standards-compliant, combined resistive temperature (RTD) and capacitive relative humidity gauge (Rotronic HygroClip IM-3) is placed next to the gratings. Measurements have been taken in 1-min intervals and automatically recorded on PC.

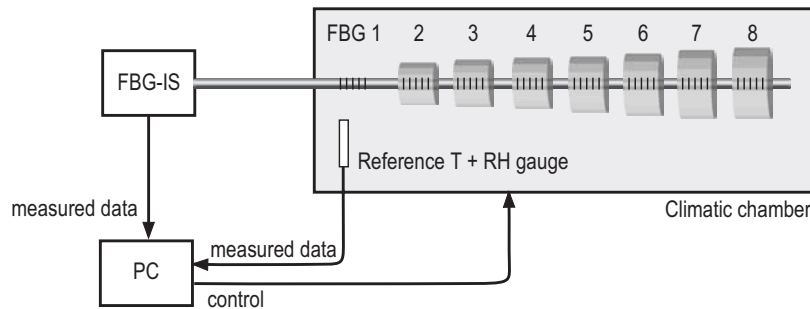


Figure 4.10 Experimental setup with an array of 8 gratings interrogated using the FBG-IS.

In order to characterise the sensor response, the RH was incrementally raised from the lowest value the climatic chamber can attain to 90 %RH, and then lowered back to the starting value for five different temperatures between 13 °C and 60 °C. The lower RH limit is given by the minimum dew point temperature, $T_{D,min}$, at which the climate chamber can operate ($T_{D,min} = 5$ °C). Each RH-step was maintained for 4 hours to make sure that the sensor response reaches a steady state. As we will see in 4.6, the time needed for the water content within the polyimide to attain an equilibrium state depends on parameters such as coating thickness and temperature. In order to analyse the reproducibility of the sensor response, a drying sequence with the same RH-steps as used for wetting was added at 39 °C. The whole sequence, which is shown in Figure 4.11, ends by returning the temperature and relative humidity to ambient values. We were not able to avoid the noisy RH regulation, mainly at low temperatures and high RH, which is due to unstable control routines of the climatic chamber. However, as the fluctuations are of rather high frequencies, it does not significantly affect the (slower) sensor response.

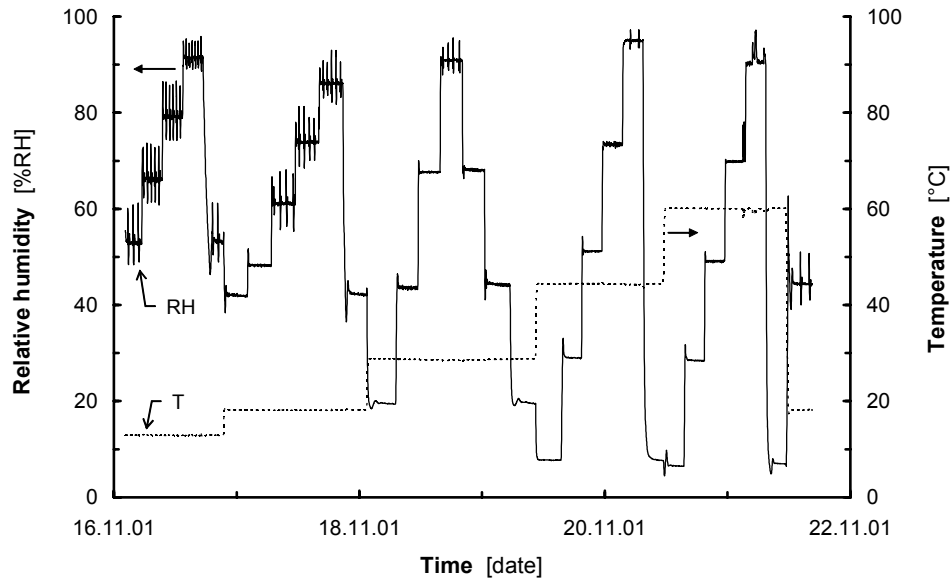


Figure 4.11 Relative humidity and temperature test sequence in climatic chamber used for characterising the sensor response (measurement data of the electrical reference gauge).

4.5.1.2 Response behaviour

Figure 4.12 shows the sensor response, $\Delta\lambda_B/\lambda_B$, of a recoated (FBG 8, recoating thickness 29.3 μm) and a bare grating (FBG 1), subjected to the test sequence described above. While the bare FBG is not sensitive to RH, the recoated FBG depends on RH. Both gratings respond to temperature variations. The mentioned hygroscopic inertia of silica and the hygroscopicity of polyimide hence are experimentally confirmed. We notice that an increase in temperature or RH shifts the Bragg wavelength to higher values, while a decrease in temperature or RH shifts the Bragg wavelength to lower values. Thus, the sensor exhibits a regular (i.e., non-inversed) and reversible response.

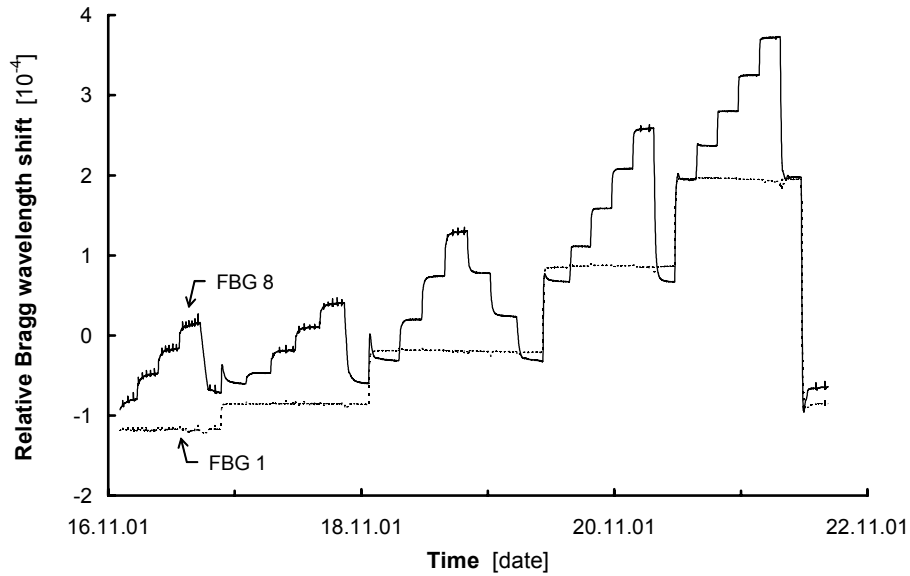


Figure 4.12 Relative Bragg wavelength shift of a polyimide recoated (FBG 8) and a bare grating (FBG 1) for the test sequence depicted in Figure 4.11.

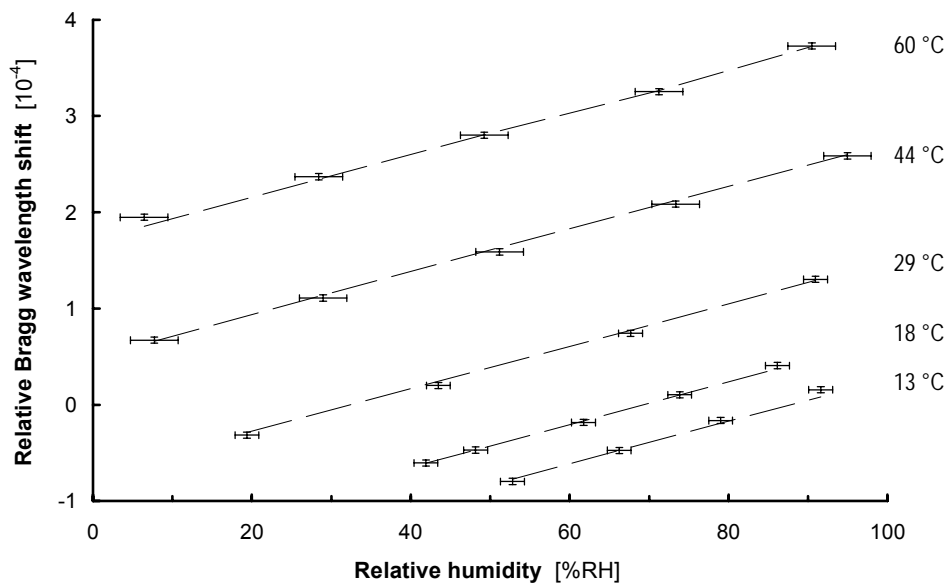


Figure 4.13 Relative Bragg wavelength shift of FBG 8 as a function of relative humidity at several temperatures (steady state average values). The error bars indicate the measurement uncertainty of the RH-gauge and the FBG interrogation system. The dashed lines represent the fitted steady state response model.

Figure 4.13 shows the average steady state relative Bragg wavelength shift of FBG 8 for each RH level and for all five temperatures. The error bars indicate the measurement uncertainties, based on the accuracy specifications of the measurement devices. For the reference gauge the RH uncertainty varies between ± 1.5 and ± 3 %RH (depending on RH and T), while for the FBG-IS the relative Bragg wavelength uncertainty is $\pm 3.2 \cdot 10^{-6}$ (based on the wavelength demodulation accuracy

mentioned in Table 4.1). The experimental data agrees with the linear dependency of the sensor response on T and RH, as proposed by the steady state response model in 3.5. Regressing the sensor response linearly on the T and RH data, the coefficients (i.e., the T- and RH-sensitivity estimates for FBG 8) are $S_{FBG,T} = (7.79 \pm 0.08) \cdot 10^{-6} \text{ K}^{-1}$ and $S_{FBG,RH} = (2.21 \pm 0.10) \cdot 10^{-6} \text{ \%RH}^{-1}$ respectively. The intercept has no physical significance and is only used for sensor calibration. The error values demarcate the 95% confidence interval of the regression coefficients. The multiple correlation coefficient of the fit is $R^2 = 0.9993$, which confirms that the sensor response may be described by a linear model. Tests with a quadratic regression have shown that the quadratic and mixed terms are smaller than the uncertainties in the linear regression: an indication that non-linear effects, such as alteration of the material properties due to temperature, humidity or stress, are not significant over the tested temperature range.

As for the bare grating, $S_{FBG,RH} = 0 \text{ \%RH}^{-1}$, whereas $S_{FBG,T} = (6.31 \pm 0.05) \cdot 10^{-6} \text{ K}^{-1}$, which matches the temperature sensitivity obtained via an independent calibration measurement using a thermostatic water bath. The T-sensitivity agrees well with the value given by Alavie [64] for $\lambda = 1.55 \text{ }\mu\text{m}$, $(6.0 \pm 0.5) \cdot 10^{-6} \text{ K}^{-1}$.

Figure 4.14 shows the steady state sensor response for a complete wetting-drying cycle at constant temperature (39 °C). The reproducibility of the sensor response is good; the end-cycle relative Bragg wavelength shift coincides again with the starting value. The absence of hysteresis shows that all absorbed water can desorb, and that the polyimide swelling is fully reversible.

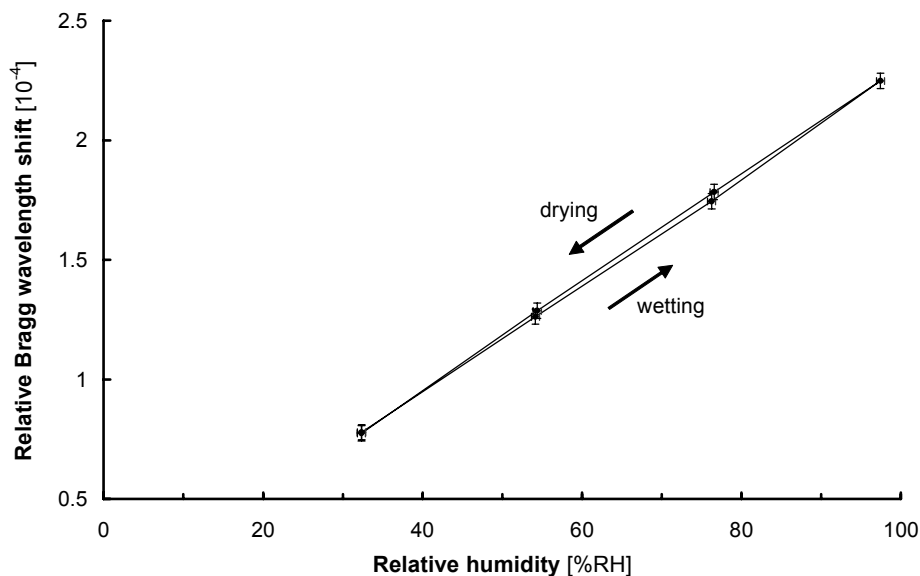


Figure 4.14 Relative Bragg wavelength shift of FBG 8 vs. relative humidity measured with the RH-gauge for a wetting-drying cycle at 39 °C (steady state average values). The error bars indicate the reproducibility of the FBG-IS and the RH-gauge.

In order to quantify the dependence of the sensor sensitivities on the coating thickness, seven gratings have been recoated, each with a different thickness (see Table 3.2). Figure 4.15 shows the RH- and T-sensitivities of the bare (FBG 1) and the recoated gratings (FBG 2 – 8) as a function of the coating cross-section area, $A_c = \pi(b^2 - a^2)$, where a and b are the fibre and coating outer radii respectively. The vertical and horizontal error bars represent the sensitivity uncertainties and the coating cross-section area uncertainties (based on the thickness uncertainty) respectively. The dashed lines represent the fitted, theoretical FBG sensor sensitivities (Eq. (3.49) and Eq. (3.50)), which depend on the coating thickness in the same way as the sensitivities of the coated fibre do (see Figure 3.7). As mentioned in 3.3.3, the sensitivities depend quasi-linearly on the coating cross-section area for thin coatings. The deviation from linearity is less than 4% for the thicknesses used here.

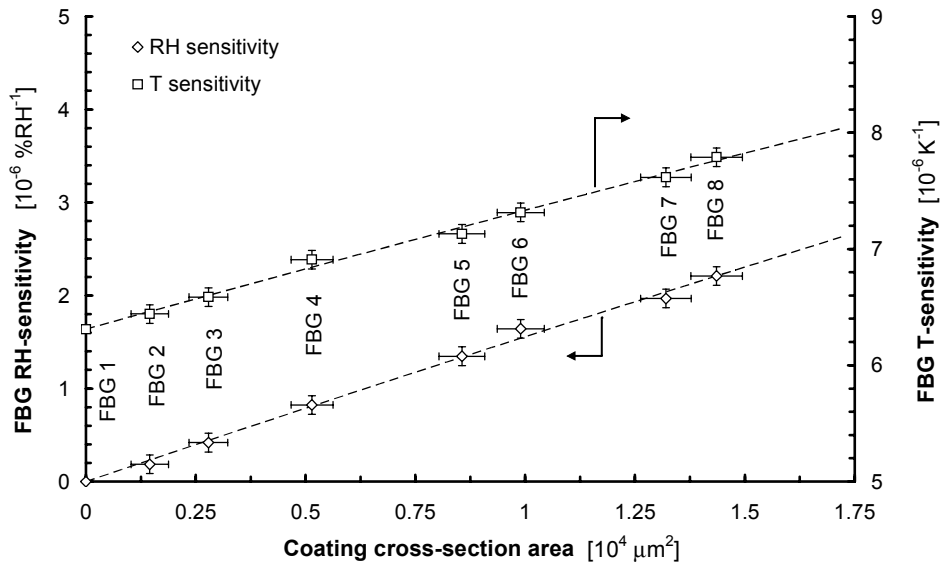


Figure 4.15 RH- and T-sensitivities of the FBG sensors as a function of the recoating cross-section area. The dashed lines represent the theoretical 3-D model.

Regressing the T-sensitivity data on the recoating thickness by means of the 3-D sensitivity model, the sensitivity gradient expresses the recoating thickness dependence of α_{cf} and \hat{p}_e , while the intercept is the sum of the constant parameters ξ and α_f . Since both α_{cf} and \hat{p}_e are also a function of various mechanical material properties such as Young's moduli, Poisson's coefficients and the thermal expansion coefficients of the fibre and the coating (see 3.3.2 and Eq. (3.9)), only the two least certain parameters, α_c and ξ , were selected to be fitted. The remaining parameters were taken from literature (see Table 4.4). The regression of the RH-sensitivity data is done analogously to the T-sensitivity regression, with β_c being the fitted parameter. The estimates are $\alpha_c = 4.9 \cdot 10^{-5} K^{-1}$, $\xi = 0.581 \cdot 10^{-5} K^{-1}$ and $\beta_c = 7.4 \cdot 10^{-5} \%RH^{-1}$. For α_c only a vague indication of its value, $4 \cdot 10^{-5} K^{-1}$, could be found in the Pyralin product

specification sheet [68]. As the properties of polyimides may vary considerably according to the curing process, this difference is acceptable. ξ agrees with the value obtained from literature, $(0.55 \pm 0.05) \cdot 10^{-5} \text{ K}^{-1}$ [64]. Concerning β_c , Sager et al. [69] has measured a hygroscopic expansion coefficient between $6.0 \cdot 10^{-5}$ and $8.0 \cdot 10^{-5} \%RH^{-1}$ (depending on the curing temperature) for a DuPont Pyralin PI 2722 polyimide film. Despite this not being exactly the same polyimide as used here, our estimate agrees well with the proposed range of values. The zero intercept of the RH-sensitivity regression confirms that bare silica is not hygroscopic ($\beta_f = 0 \%RH^{-1}$). Table 4.4 resumes all fibre and coating material properties.

Property	This work	Other work	
			Ref.
Fibre (silica)			
Young's modulus, E_f [GPa]	-	72	[67]
Thermal exp. coeff., α_f [10^{-5} K^{-1}]	-	0.05	[38]
Hygroscopic exp. coeff., β_f [$\%RH^{-1}$]	0	0	
Thermo-optic coeff., ξ [10^{-5} K^{-1}]	0.581	0.55 ± 0.05	[64]
Effective refractive index, n_{eff}	-	1.446	
Strain-optic coeff., p_{11}	-	0.121	[38]
Strain-optic coeff., p_{12}	-	0.270	[38]
Recoating (Pyralin polyimide)			
Young's modulus, E_c [GPa]	-	2.45	[68]
Thermal exp. coeff., α_c [10^{-5} K^{-1}]	4.9	4	[68]
Hygroscopic exp. coeff., β_c [$10^{-5} \%RH^{-1}$]	7.4	6.0 – 8.0	[69]

Table 4.4 Properties of the fibre and recoating materials (wavelength: 1550 nm).

It is important to emphasise that the stated coating material properties are only valid for Pyralin polyimide which is coated and cured according to the indications given in this work. Any modifications of the coating / curing process or of the used polyimide type may lead to different material properties. An investigation of the recoating properties of the commercial gratings reveals a minor inconsistency. Lacking any information about the polyimide type and the coating / curing process used by the manufacturer, mechanical recoating material properties of the Innovative Fibers gratings were not investigated.

4.5.2 SOFO sensor

4.5.2.1 Experimental setup

As with the FBG sensor, the SOFO sensor's response to RH and T was evaluated experimentally in the computer controlled climatic chamber. Figure 4.16 shows the experimental setup. For reference monitoring, the Rotronic RH / T gauge was placed next to the sensor. Measurements were taken in 2-min intervals and automatically recorded on PC.

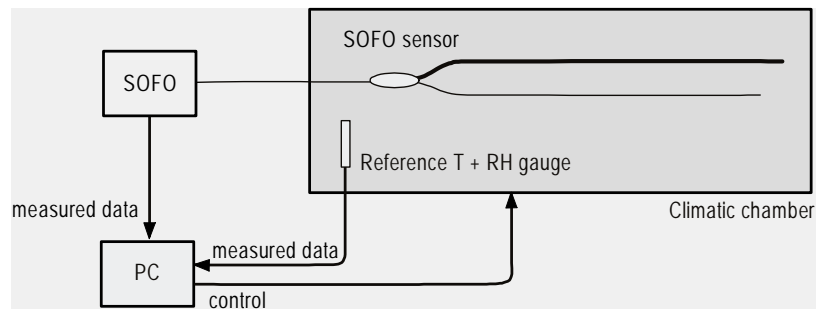


Figure 4.16 Experimental setup with a SOFO sensor in the climatic chamber.

The test sequence used for characterising the sensor response is depicted in Figure 4.17. Several temperature and relative humidity settings from 24 °C to 61 °C and from 10 %RH to 90 %RH were run.

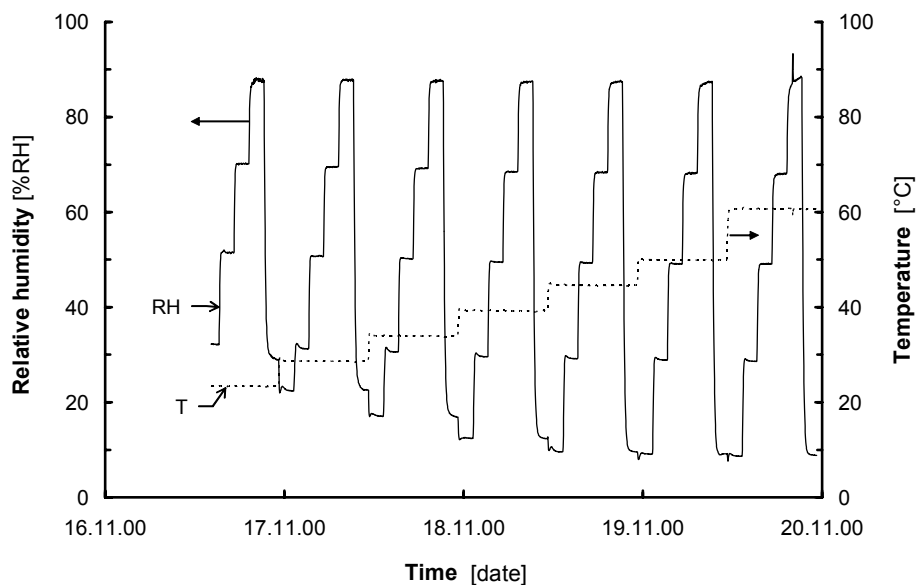


Figure 4.17 Relative humidity and temperature test sequence in the climatic chamber used for characterising the SOFO sensor response (measured with the Rotronic reference gauge).

4.5.2.2 Response behaviour

Figure 4.18 shows the response of the SOFO sensor specified in 4.4.2, subjected to the test sequence shown above. The sensor exhibits a regular and reversible response to RH and temperature.

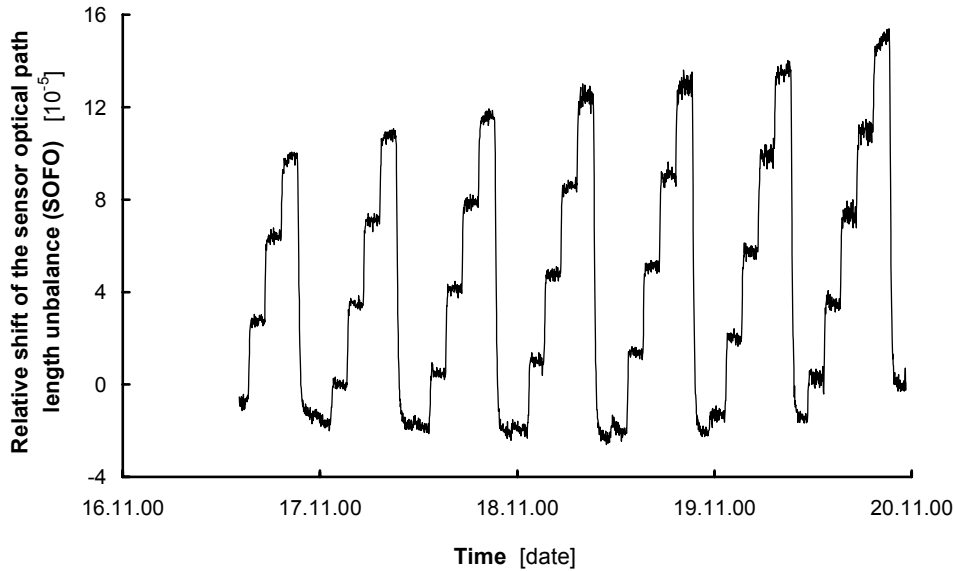


Figure 4.18 Relative shift of the optical path length unbalance of a SOFO sensor for the test sequence depicted in Figure 4.17.

The RH- and T-sensitivities of the SOFO sensor, estimated by regressing the sensor response linearly on the T and RH reference measurements, are $S_{SOFO,RH} = (1.90 \pm 0.01) \cdot 10^{-6} \%RH^{-1}$ and $S_{SOFO,T} = (1.33 \pm 0.01) \cdot 10^{-6} K^{-1}$ respectively (see Eqs. (3.56) and (3.57)). The error values demarcate the 95% confidence interval of the regression coefficients. The multiple correlation coefficient of the fit is $R^2 = 0.995$.

The SOFO sensor sensitivities, calculated with the 3-D model on the basis of the mechanical fibre and coating properties which were used for the FBG sensor (see Table 4.4) and on the dimensions of the fibres (see 4.4.2), are $S_{SOFO,RH} = 2.03 \cdot 10^{-6} \%RH^{-1}$ and $S_{SOFO,T} = 1.67 \cdot 10^{-6} K^{-1}$. As the operating wavelengths of the SOFO and FBG systems are not the same, the optical properties of the fibre differ from the ones used for the FBG sensor (see Table 3.1).

The deviation between the experimental and theoretical sensitivities is probably due to the different mechanical properties of the polyimide coating of the Spectran fibre compared to the Pyralin polyimide FBG coating.

Contrary to the FBG sensor, the RH- and T-sensitivities of the SOFO sensor cannot readily be modified by adapting the coating thickness, unless a fibre with different coating thickness is available. For a given coated fibre, the sensitivities may only be varied by modifying the arm-to-sensor length ratios (see Eqs. (3.56) and (3.57)). The

adaptation of this sensitivity parameter is however limited due to the restricted allowable length difference between the sensor arms (see Eq. (4.2)), making it useless for modifying the RH- and T-sensitivities to any substantial degree.

Due to its dual fibre configuration, a large proportion of the SOFO sensor's T-sensitivity is auto-compensated (both fibres respond similarly to T-variations). This results in a much smaller temperature sensitivity compared to the FBG sensor. As we will see in 4.7, the remaining temperature sensitivity can be cancelled by adjusting the sensor arm lengths.

4.6 Transient state sensor response (FBG)

The following experimental evaluation of the transient state response behaviour focuses on the short gauge length fibre Bragg grating type RH-sensor. The SOFO sensor is expected to behave similarly, as the bare fibre is not hygroscopic and thus does not affect the transient state response. However, the diffusivity values of the coating may not be the same because the polyimide and its curing process are likely to differ.

4.6.1 Experimental setup

The transient state sensor response was investigated for a commercial grating (FBG 11, recoating thickness 50 μm) by means of the tunable laser interrogation system and Rotronic's electrical reference gauge. The specifications indicate for the RH-sensitive element (C94 capacitance) a response time of 10 s to reach 70% of the final response. The filter cover (metallic net with mesh size 20-25 μm) does not significantly retard the sensor response.

Similar to the test sequence used for the steady state, the RH-gauge and FBG sensor responses were recorded in 1-min intervals for 4 relative humidity elevations (10 \rightarrow 30, 30 \rightarrow 50, 50 \rightarrow 70 and 70 \rightarrow 90 %RH) at 7 different temperatures (23, 29, 34, 39, 45, 50 and 60 $^{\circ}\text{C}$). Again, the inferior RH limit at low temperatures is higher than the 10 %RH target value due to the dew point temperature limitation of the climate chamber. At 23 $^{\circ}\text{C}$ the 10 \rightarrow 30 %RH step is completely omitted. Each RH level was maintained for 2 hours in order to make sure that the sensor response reaches a steady state. In order to avoid any disturbance by calibration irregularities, the FBG sensor and RH-gauge data are analysed individually for each RH-step.

4.6.2 Response behaviour

Figure 4.19 shows the normalised transient responses of the FBG sensor and the RH-gauge for the 30 → 50 %RH step at 23 °C. The plain curve represents the normalised water uptake in the polyimide coating layer, calculated with the tubular layer diffusion model shown in 3.4.3 and fitted to the experimental FBG sensor data. As the axial deformation of the coated fibre is assumed to be uniform on its section (plane section conservation), the sensor response is proportional to the mass of water accumulated over the entire coating thickness. The continuously varying RH-gauge measurements indicate that the boundary conditions of the diffusion model are nonsteady state. Therefore, the model uses them as external concentration values. Water permeation tests with DuPont's PI-2550 polyimide have indeed revealed a temperature independent, linear sorption isotherm between 10 and 100 %RH [65], justifying the assumption of a concentration independent solubility coefficient and hence the linear relation between RH and boundary concentration. The fitted coefficient (i.e., the estimate of the polyimide coating diffusivity) is $D = 0.92 \cdot 10^{-12} \text{ m}^2/\text{s}$ and the resulting root mean square error (RMS) between the model and the experimental data at 0.01 to 0.95 is $\text{RMS} = 0.012$. The obtained diffusivity falls well within the range of values indicated in literature. Mrotek et al. [73] investigated the moisture diffusion in polyimide coatings by using a special experimental technique based on fibre strength measurements and proposes a diffusivity of $D = (1.2 \pm 0.4) \cdot 10^{-12} \text{ m}^2/\text{s}$ for a 20 → 95 %RH step at 25 °C.

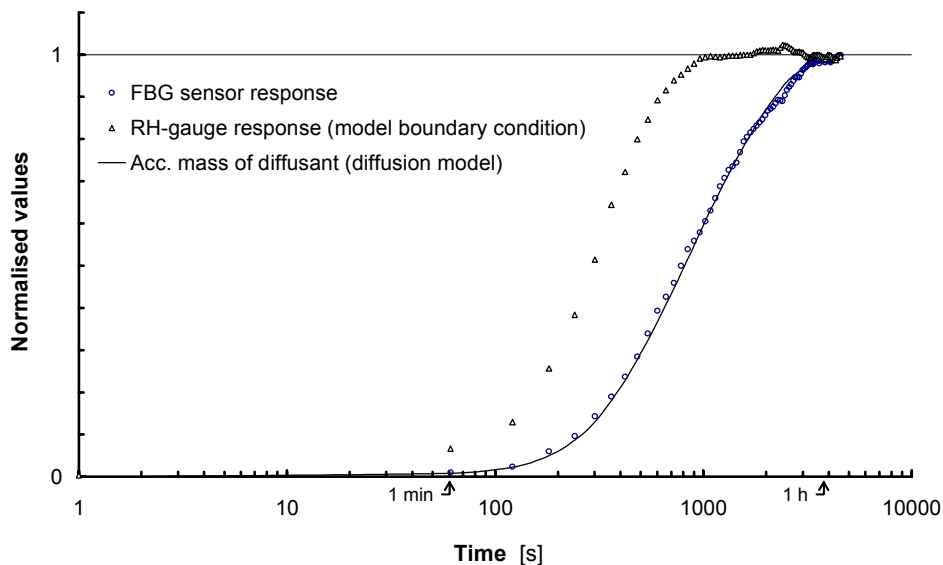


Figure 4.19 Normalised transient state sensor response for the 30 → 50 %RH step at 23 °C and fitted tubular diffusion model (the nonsteady state external boundary concentration is obtained from the electrical RH-gauge).

Figure 4.20 resumes the estimated sorption diffusivity values (logarithmic scale) for each RH-step as a function of the reciprocal of absolute temperature, $1/T$. The diffusivity values rise as a function of temperature, i.e., higher temperature accelerates the diffusion process. This acceleration is due to the increased kinetic energy available at higher temperatures and may be expressed using Arrhenius'⁵ relation

$$D(T) = D_0 \exp\left(-\frac{E_A}{RT}\right), \quad (4.3)$$

where

- D_0 is the frequency factor,
- E_A is the activation energy and
- $R = 8.314 \text{ J mol}^{-1} \text{ K}^{-1}$ is the universal gas constant.

The activation energy for diffusion can be thought of as the energy required to stretch the polymer chain against the polymer's cohesive forces, thus forcing the diffusing molecule through the surrounding structure. The frequency factor is related to the number of holes in the chain that are capable of accommodating a water molecule. If we assume that D_0 and E_A do not depend on temperature but may depend on RH, we can estimate them by fitting Arrhenius' equation individually for each RH-step to the experimental diffusivity data (lines in the figure). The values of the fitted parameters are listed in Table 4.5.

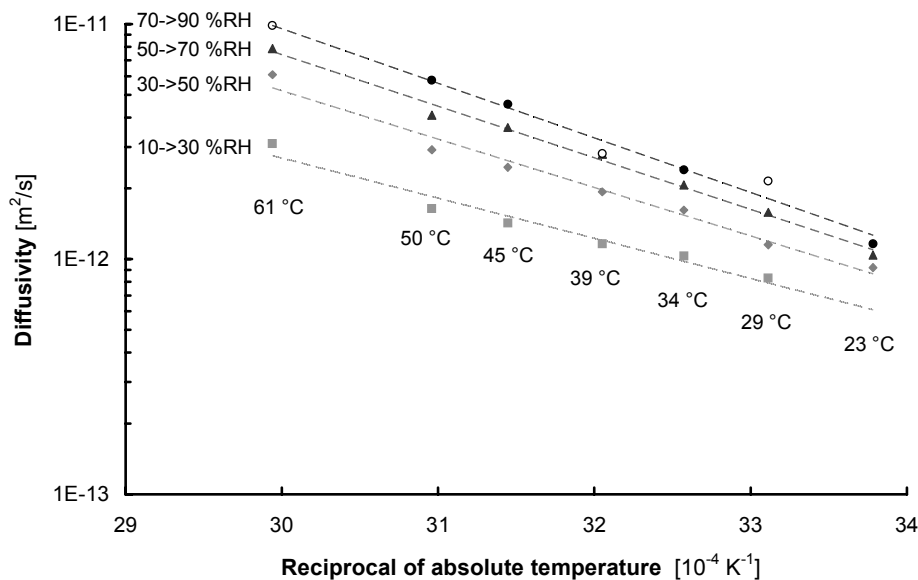


Figure 4.20 Arrhenius plot of the diffusivity as a function of the reciprocal of the absolute temperature, grouped according the RH-steps. Blanked out markers indicate inferior correlation (RMS > 0.020) between the experimental data and the diffusion model. The dashed lines represent the fitted Arrhenius' equation (Eq. (4.3)).

⁵ Arrhenius' equation is used to describe thermodynamic processes by predicting the rate of a chemical reaction at a certain temperature, given the activation energy and the chance of successful collision of molecules.

RH-step	Frequency factor, D_0 [$\text{m}^2 \text{s}^{-1}$]	Activation energy, E_A [kJ mol^{-1}]	R^2
10 → 30 %RH	$0.35 \cdot 10^{-6}$	32.7	0.964
30 → 50 %RH	$7.75 \cdot 10^{-6}$	39.4	0.982
50 → 70 %RH	$28.2 \cdot 10^{-6}$	42.0	0.992
70 → 90 %RH	$87.8 \cdot 10^{-6}$	44.4	0.982

Table 4.5 Estimates of the fitted Arrhenius' equation parameters as a function of the RH-step.

The estimated D_0 and E_A are similar to the values found in literature. Sacher et al. [65] propose for DuPont's PI-2550 polyimide at 50 %RH a frequency factor of $3 \cdot 10^{-6} \text{ m}^2/\text{s}$ or $10 \cdot 10^{-6} \text{ m}^2/\text{s}$ and an activation energy of $(43.6 \pm 2.2) \text{ kJ/mol}$ or $(46.3 \pm 3.9) \text{ kJ/mol}$, depending on the analysing method, namely polymer permeation analyser or sorption balance respectively, used by them.

We notice that higher RH-levels result in a rise of the frequency factor as well as the activation energy leading us to the conclusion that the diffusivity of polyimide is concentration dependent. This observation becomes even more evident when plotting the diffusivity as a function of the average partial vapour pressure per RH-step (see Figure 4.21).

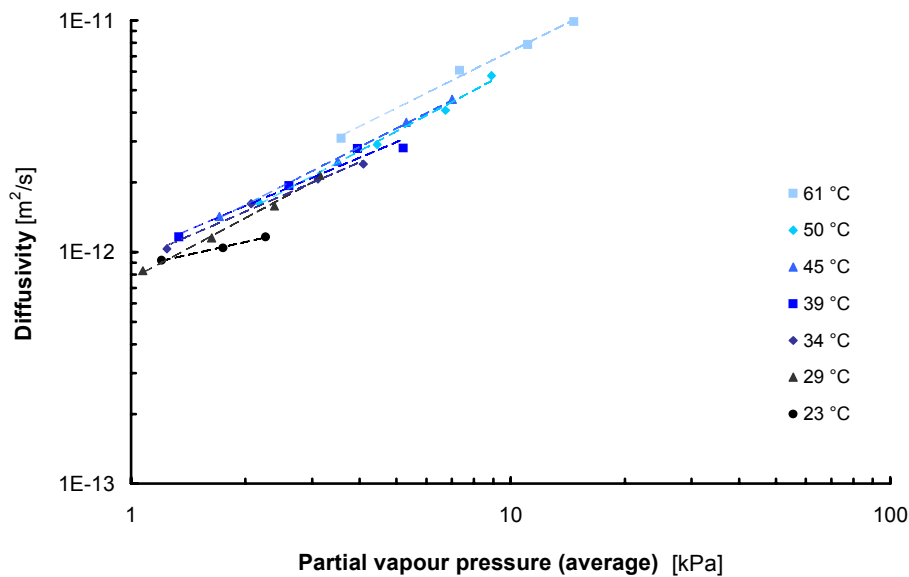


Figure 4.21 Estimated diffusivities as a function of the average partial vapour pressure for several temperatures. The dashed lines are the isothermal power-law trend lines.

Since $\log(D)$ appears to depend linearly on $\log(p)$, we may express the diffusivity as the empirical power-law function of the concentration seen in Eq. (3.33) – still assuming that the solubility is concentration independent.

Table 4.6 lists the estimates of the isothermal (i.e., they are kept constant for each temperature) diffusivity parameters obtained from the fit of the diffusion model with concentration dependent diffusivity to the experimental data.

Temperature	Coefficient, D_0 [$\text{m}^2 \text{s}^{-1} \text{kPa}^{-1}$]	Power, a	RMS error
23 °C	$0.86 \cdot 10^{-12}$	0.36	0.016
29 °C	$0.84 \cdot 10^{-12}$	0.63	0.024
34 °C	$1.05 \cdot 10^{-12}$	0.56	0.020
39 °C	$0.94 \cdot 10^{-12}$	0.70	0.022
45 °C	$0.90 \cdot 10^{-12}$	0.80	0.021
50 °C	$0.87 \cdot 10^{-12}$	0.81	0.022
61 °C	$1.24 \cdot 10^{-12}$	0.79	0.027

Table 4.6 Estimated parameters of the concentration dependent diffusivity as a function of temperature, obtained from the fit of the diffusion model with concentration dependent diffusivity to the experimental data (D_0 is vapour pressure related).

It is difficult to tell whether the estimated diffusivity parameters depend significantly on temperature or if their variability lies within the statistical uncertainty of the measurements and the used models. Ignoring the two temperature levels with the highest RMS error, the power value, a , seems nonetheless to increase with a rise in temperature. A more detailed theoretical and experimental study of the phenomena involved would certainly help in clarifying this point.

A comparison of wetting (in-) and drying (out-diffusion) confirms the observed concentration dependence of the diffusivity. Using the diffusion model with concentration independent diffusivity, an experimental study of the transient response of a 30 μm thick coating at 39 °C revealed up to 30% higher diffusivity for a drying step than for the wetting step with the same RH boundaries. This agrees with the fact that higher concentration results in higher diffusivity because it is predominately the starting condition of a RH-step (low concentration / diffusivity when wetting, high concentration / diffusivity when drying) which determines the average diffusivity.

If the diffusion model with concentration dependent diffusivity is fitted to the experimental data of a single RH-step, then the estimated power parameter of the diffusivity law is always negative. But this would indicate a decrease in diffusivity with a rise in humidity, which is inconsistent with the positive concentration dependence of the average diffusivity observed when the fit is performed over several RH-steps. The following measurement anomalies may explain this inconsistency:

- Delay between the real humidity conditions in the climate chamber and the RH-gauge response, which serves as boundary condition, is not considered.
- Internal clocks of RH-acquisition unit and FBG system may be inaccurately synchronised (offset between time stamps of the recorded measurement data).
- 1-min acquisition interval may be too large to synchronise accurately enough the fibre optic with the reference sensor.

The concentration dependence of the diffusivity indicates the presence of a chemical interaction between the diffusant and the polymer matrix, which is characteristic for the hygroscopic swelling of polyimides (H-bonding). Nevertheless, the observed concentration dependence is surprising since it contradicts Mrotek's findings [73]. Mrotek states that polyimide diffusivity is concentration independent.

4.7 Temperature compensation

In order to discriminate the RH information from the sensor response, the humidity sensor needs to be temperature compensated.

For the FBG sensor, all-fibre compensation may be done by colocating two gratings with different T- and RH-sensitivities. As discussed in 3.5, the FBG sensitivities may be modified by varying the recoating thickness. Since the temperature discrimination improves the more the RH-sensitivity ratio differs from the T-sensitivity ratio [45], a combination of a polyimide recoated and a bare grating is ideal for this purpose.

A more affordable alternative to this all-fibre configuration is to use an electrical temperature sensing element, such as a thermocouple and a thermistor, placed next to the polyimide recoated grating. Using an electrical sensor for temperature compensation, the RH-sensor however loses some of its metrological benefits characteristic to fibre optic sensors, such as their electromagnetic immunity and ease to be multiplexed.

Figure 4.22 shows the RH- and T-measurements obtained with the Rotronic reference gauge and the calculated RH obtained from the calibrated and temperature compensated FBG sensor response (FBG 6). The steady state deviation between the two RH responses is due to the measurement errors of the electrical sensors and the inaccuracies inherent to the behaviour model, the calibration and the demodulation of the fibre optic sensor. For the example shown, the maximum deviation is less than 5 %RH.

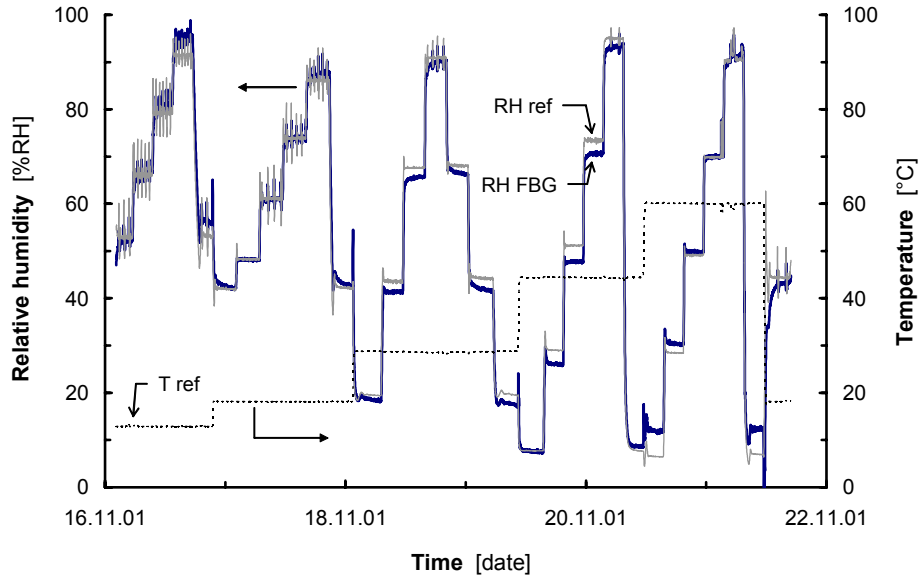


Figure 4.22 Calibrated and temperature compensated response of the FBG humidity sensor and reference RH / T as a function of time.

The SOFO sensor (partially) auto-compensates temperature effects due to its Michelson interferometer setup. Nevertheless, except for the special sensor configuration which allows a full auto-compensation (see following paragraph), full temperature compensation requires an additional colocated temperature sensor. An all-fibre T-compensation may be performed in combination with a SOFO temperature sensor [80]. Figure 4.23 shows the calibrated and temperature compensated response of the SOFO sensor described in 4.4.2. The steady state deviation between the SOFO and the reference RH is less than 2 %RH.

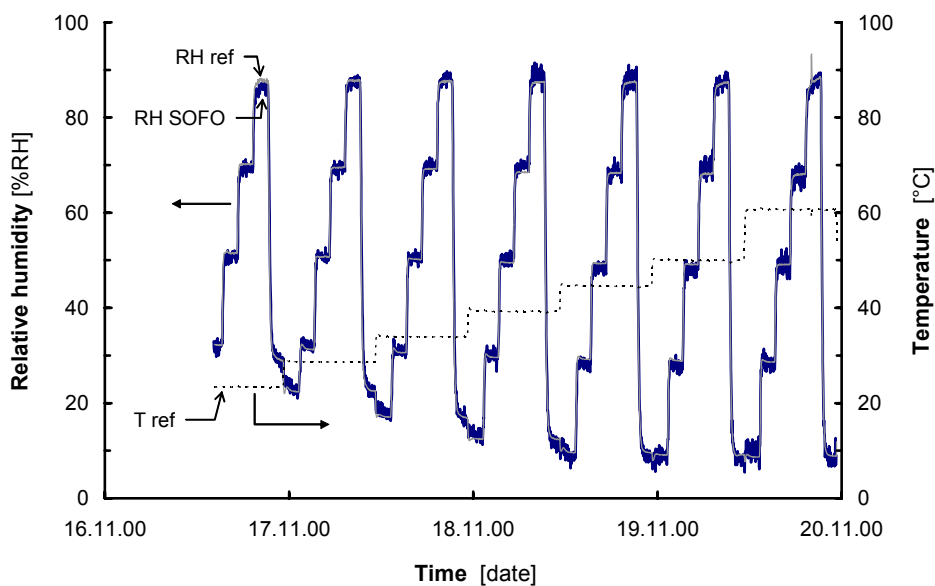


Figure 4.23 Calibrated and temperature compensated response of the SOFO humidity sensor and reference RH / T as a function of time.

For a full temperature auto-compensation, $S_{SOFO,T}$ (Eq. (3.57)) has to be zero. This is the case when the sensor arm length ratio, L_s/L_l , satisfies the following condition

$$\frac{L_s}{L_l} = \frac{S_{T,l}}{S_{T,s}} (\leq 1).$$

With the bare fibre as the long sensor arm and the polyimide coated fibre as the short sensor arm, the sensor arm length ratio for which the temperature is fully compensated becomes

$$\frac{L_s}{L_l} = 0.910.$$

Figure 4.24 illustrates the efficiency of the temperature auto-compensation of the SOFO sensor in comparison to the uncompensated FBG sensor response. The temperature rise has little influence on the SOFO sensor response.

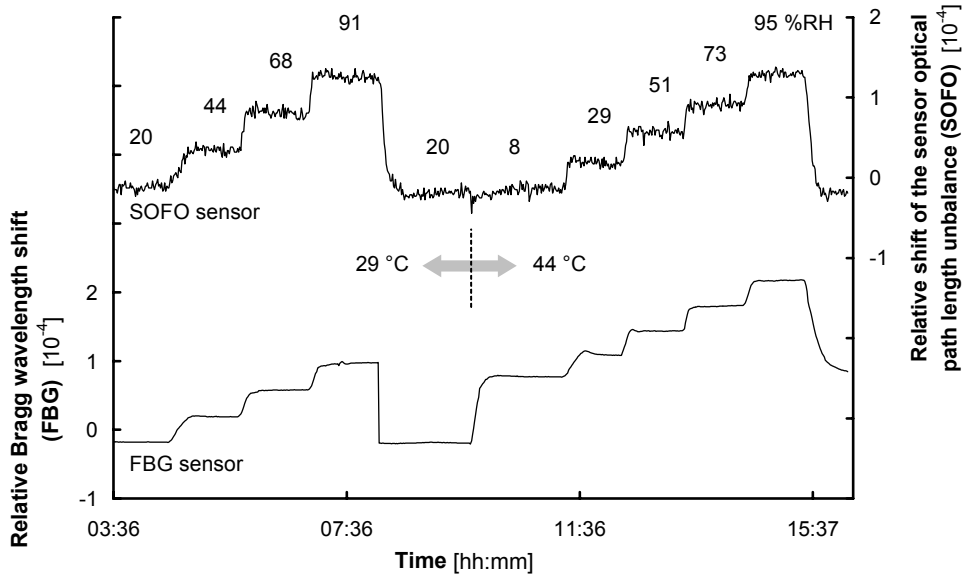


Figure 4.24 SOFO and FBG sensor responses to RH and T variations.

4.8 Discussion

Figure 4.25 shows the RH measurement uncertainty as a function of the recoating thickness. The RH measurement uncertainty is determined using

$$\text{RH uncertainty (FBG)} = \frac{S_{tot}}{\lambda_B S_{FBG,RH}}, \quad (4.4)$$

where $S_{tot} = \sqrt{\sum S_i^2}$ is the combined uncertainty of all systematic and random uncertainty sources i , expressed as a wavelength.

Considering only the RH uncertainty due to the wavelength demodulation inaccuracy of the interrogation system (see Table 4.1) and ignoring model, calibration and temperature compensation uncertainty, we obtain the values plotted in Figure 4.25. The RH measurement uncertainty depends hyperbolically on the coating thickness. If the grating is demodulated with the FBG-IS, a 30 μm thick recoating is sufficient to comply with the accepted uncertainty mentioned in 4.1 ($\pm 3\% \text{RH}$).

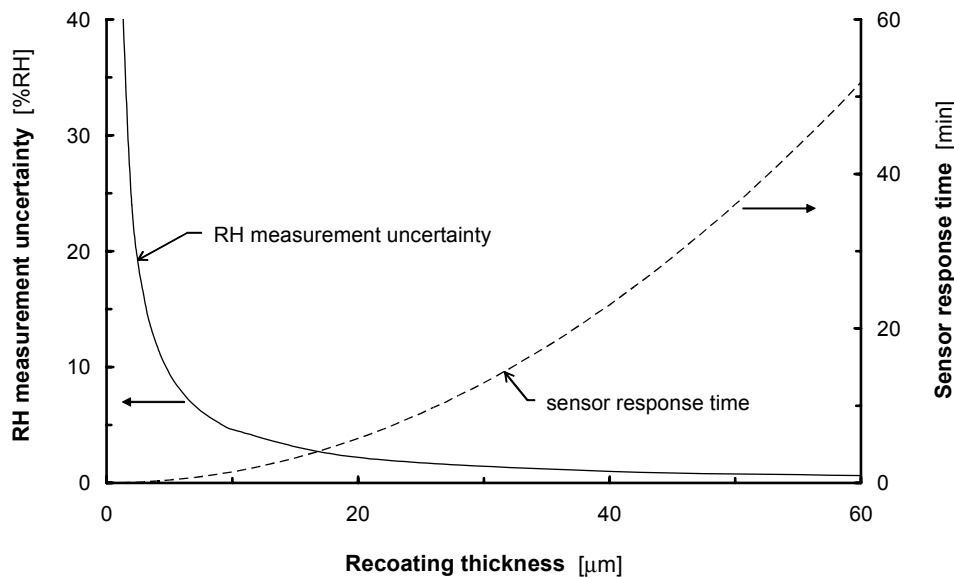


Figure 4.25 RH measurement uncertainty and (unpacked) sensor response time (90% final response after sudden RH-rise from 50 to 70 %RH at 20 °C) as a function of recoating thickness, according to the specifications of the FBG-IS.

The coating thickness influences also the sensor response time (the thicker the coating the slower the response). Figure 4.25 shows, as a function of the recoating thickness, the estimated time needed for the sensor to reach 90% of its final response following a sudden RH-rise calculated on the basis of the polyimide diffusivity at 50 \rightarrow 70 %RH and 20 °C.

Comparing the sensor response time with the RH measurement uncertainty, a trade-off in terms of optimum recoating thickness has to be made. For applications that require a rapid sensor response (or low temperature applications, which comes to the same), thin coatings should be used, this results however in less accurate measurements. On the other hand, very accurate measurements require thick recoatings, which increase the response time. For the 30 μm recoating thickness suggested above, the sensor response time at 20 °C is \approx 13 min.

While the RH measurement uncertainty of the FBG sensor depends on the recoating thickness, the RH measurement uncertainty of the SOFO sensor depends on the gauge length, L . It is calculated using

$$\text{RH uncertainty (SOFO)} = \frac{S_{tot}}{n_g L S_{SOFO,RH}}, \quad (4.5)$$

where $S_{tot} = \sqrt{\sum S_i^2}$ is the combined uncertainty of all systematic and random uncertainty sources i , expressed as a sensor optical path length unbalance.

For the SOFO sensor, the main source of uncertainty is the limited SOFO reading unit demodulation resolution (see Table 4.3). The uncertainty due to the deviation from linearity has only little influence for small dynamic ranges. This is because the humidity and temperature induced modulation of the optical path length unbalance increases with longer sensors, whereas the resolution of the optical path length unbalance demodulation of the SOFO reading unit remains sensor length independent. Hence, the RH measurement uncertainty decreases for longer sensors. Figure 4.26 illustrates the simulated RH measurement uncertainty of the SOFO sensor as a function of the sensor gauge length. For a fully temperature compensated sensor, the gauge length is limited to $L < 60$ cm, which produces a noisy response (RH uncertainty > 2.9 %RH). This trade-off may be overcome by replacing the bare fibre with a non-hygroscopically coated fibre that has a similar thermal expansion coefficient to the polyimide coated fibre. Once more, fibres with metallic coatings are an interesting option for this.

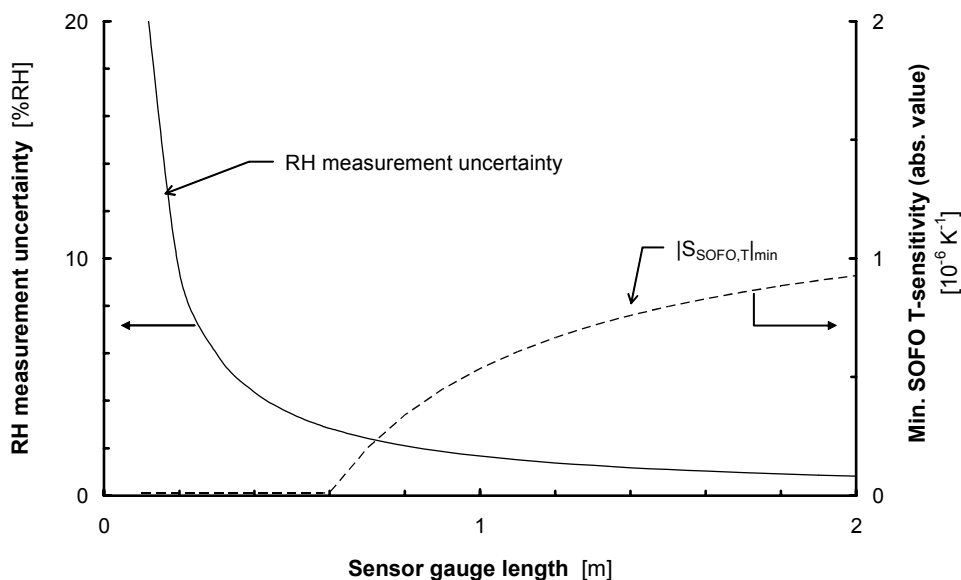


Figure 4.26 RH measurement uncertainty and minimum absolute SOFO T-sensitivity as a function of the sensor gauge length, according to the specifications of the SOFO reading unit. The minimum T-sensitivity is determined such that the allowed optical path length unbalance is not exceeded, i.e., the length difference between the two sensor arms must be smaller than 5.8 cm.

4.9 Sensor packaging

The purpose of the sensor packaging is to allow the sensing fibre to be embedded in the host material while remaining mechanically unconstrained. The packaging must satisfy the following requirements:

- Water vapour permeability
- Anti-adherent
- Mechanical protection of the fibre during sensor installation and, if used for concrete monitoring, during concrete pouring

The second requirement is particularly important in order to avoid that the RH- and T-induced deformation of the fibre is hindered by friction with the packaging.

Polytetrafluoroethylene (PTFE, also known as DuPont's brand Teflon®) satisfies all these requirements. This polymer features an extremely low coefficient of friction with excellent non-stick properties. Moreover, PTFE is virtually inert to all chemicals, has a wide service temperature range from -70 to 260 °C and is very durable. In sleeve form, it protects the inlaying fibre well. PTFE is hydrophobic, i.e., it keeps liquid water out, but allows water vapour to diffuse through it. As a consequence, the fibre is never immersed in water, even if the host material is water saturated. However, PTFE exhibits low vapour permeability and thus additionally delays the sensor response. Figure 4.27 illustrates the set-up of the packaged sensor.

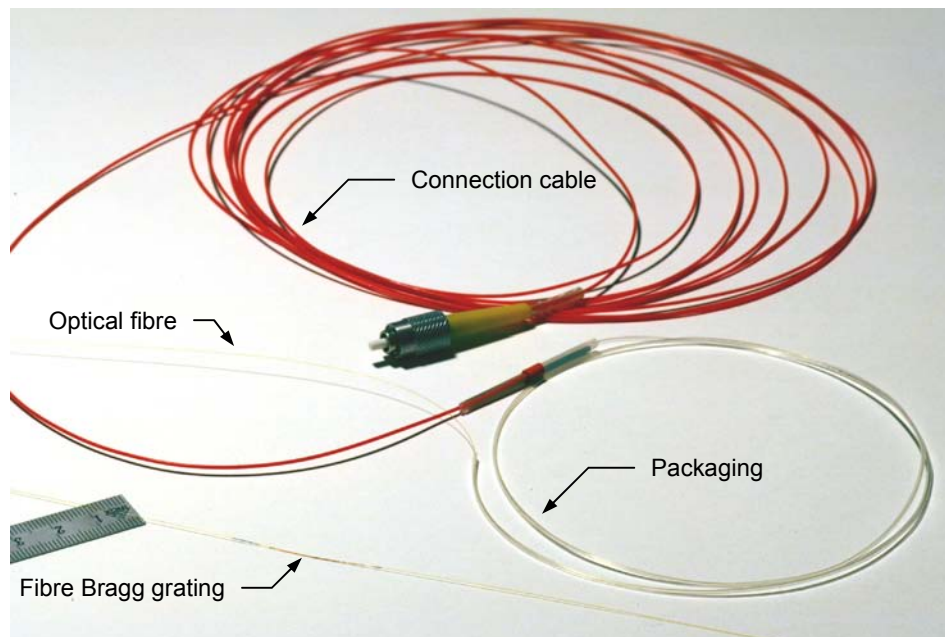


Figure 4.27 Sensor packaging set-up (FBG sensor).

Transient response tests with a FBG inserted in a thin wall PTFE sleeve (STW24 from Grange Tubes, inner diameter ≈ 0.58 mm, wall thickness ≈ 0.15 mm) have shown that the sensor has a response time to reach 90% saturation of $t_{90} \approx 1$ day at 20°C when exposed to a sudden RH change (steady state boundary conditions). According to Arrhenius' relation, this value increases quasi-exponentially with decreasing temperature (see Figure 4.28).

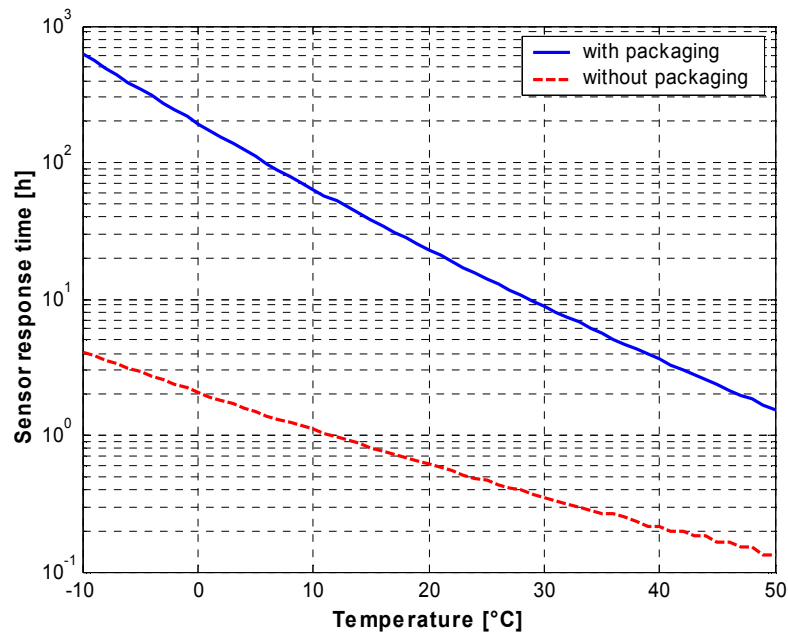


Figure 4.28 Estimated time for the sensor to reach 90% of the final response after a sudden RH change as a function of temperature for a sensor with and without PTFE sleeve packaging.

We note that for low temperatures the response time of the packaged sensor may become very long with t_{90} already exceeding 1 week at the freezing point. Compared with a FBG without packaging (FBG 11, $50 \rightarrow 70$ %RH), the packaging boosts the sensor response time by a factor of 20 at 50°C to more than a factor of 100 at sub-zero temperatures. In order to limit the amplification factor of the delay to 10 at the freezing point (i.e., $t_{90} \approx 1$ day at 0°C , $t_{90} \approx 2.5$ h at 20°C), the PTFE sleeve would require a wall thickness of 0.05 mm. This is a third of the actual dimension. Although PTFE sleeves with such a thin wall are not readily available they may be fabricated on demand (e.g., by Zeus Industrial Products, Inc.)

Figure 4.29 shows typical daily RH- and T-variations in near-surface concrete (depth 10 mm) as measured by Basheer et al. [21]. Figure 4.30 shows a simulation of the expected sensor response to this environment.

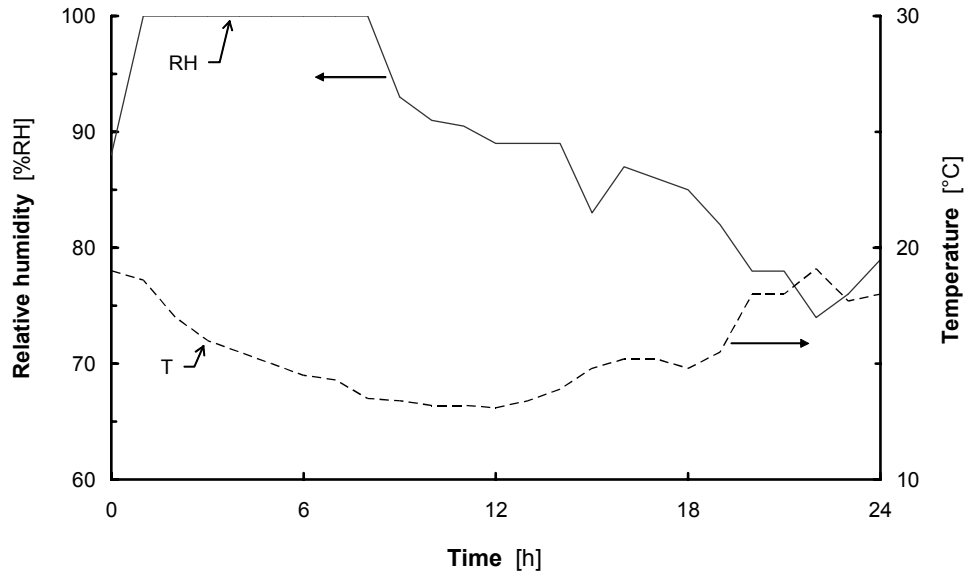


Figure 4.29 RH- and T-values measured over 24 h in near-surface concrete (depth 10 mm) (data from [21]).

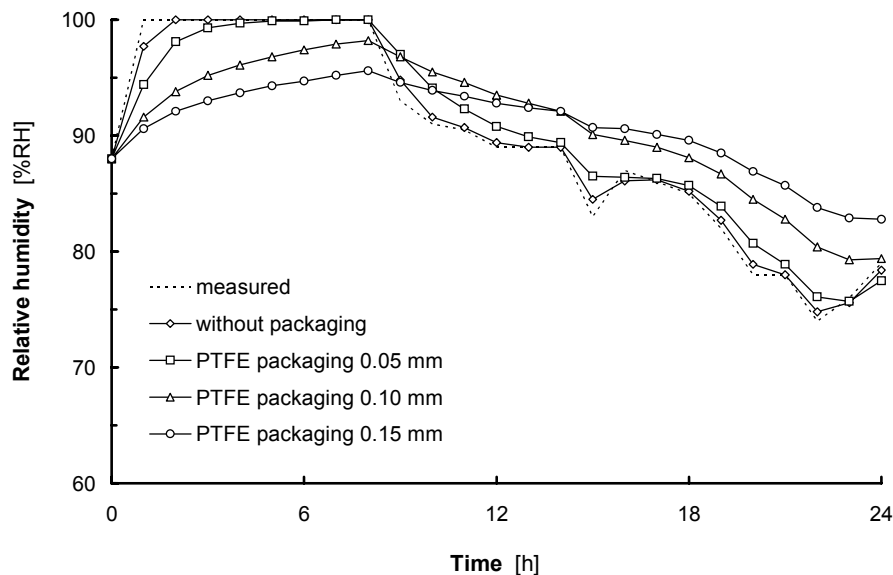


Figure 4.30 Simulated response of an unpackaged and of three packaged sensors with different sleeve wall thicknesses, based on characteristic RH- and T-values measured in near-surface concrete (see Figure 4.29). At the beginning, the fibre optic RH-sensor is in equilibrium with its environment.

Comparing the reference RH-values with the simulated fibre optic sensor RH-measurements, the following sensor response delay induced deviations are found (expressed as root mean square deviations):

Sensor	Deviation (RMS)
Without packaging	0.8 %RH
PTFE packaging, wall thickness 0.05 mm	2.0 %RH
PTFE packaging, wall thickness 0.10 mm	4.4 %RH
PTFE packaging, wall thickness 0.15 mm	5.8 %RH

The unpackaged sensor induces the smallest deviation, which is on average less than 1 %RH, while the thickest packaging produces the highest deviation, which is of the order of 6 %RH. These values are indicative and may be smaller for deeper sensor locations, less permeable concrete, less exposed test site or slower changes of external climatic conditions (rain, sun). We note that, if accurate humidity monitoring in a rapidly humidity-changing environment is required, the tested PTFE sleeve (wall thickness 0.15 mm) may delay the sensor response excessively and an alternative, more permeable packaging solution should be used.

4.10 Concluding remarks

A FBG point and a SOFO long gauge fibre optic relative humidity sensor based on a hygroscopically swelling transducer coating (polyimide) have been implemented. The sensors exhibit a linear, reversible and reproducible response to relative humidity between 5 and 95 %RH and between 13 to 60 °C, at least. The responses of the sensors therefore agree with the steady state behaviour models proposed in chapter 3.

The FBG sensor RH- and T-sensitivities depend on the recoating thickness as predicted by the mechanical model. The thermal and hygroscopic expansion coefficients of the polyimide coating agree with the values given in the literature.

The temperature cross-sensitivity of the sensors agrees with the model. For the FBG sensor the temperature cross-sensitivity may be compensated by using a collocated bare grating. The SOFO sensor (partially) auto-compensates temperature effects, making it less sensitive to temperature variations than the FBG sensor.

The RH values obtained from the calibrated and temperature compensated optical fibre responses agree well with the RH measurements of the electrical reference gauge.

The transient state response of the sensor agrees with the tubular diffusion model proposed in 3.4.3. The polyimide diffusivity matches the values proposed in literature and the temperature dependence of the diffusivity is coherent with thermodynamic

considerations (Arrhenius' relation). The concentration dependence of the diffusivity indicates the presence of a chemical interaction between the diffusant and the polymer matrix, which is characteristic for the hygroscopic swelling of polyimides (H-bonding). Considering the temperature and concentration dependence of the diffusivity we conclude that the sensors respond quicker for drying at high temperatures and high relative humidities and slower for wetting at low temperatures and low relative humidities.

Since the FBG sensor measures more accurately with thick recoatings (increased sensitivity) but responds quicker with thin recoatings, there is a trade-off between sensitivity and response time. For SOFO sensors, the measurement noise decreases for long gauge lengths while the temperature auto-compensation is best at short gauge lengths; thus the trade-off between measurement noise and temperature auto-compensation.

Due to its low permeability, the sensor packaging sleeve is the main controlling factor of the response time of the packaged sensor (response time of the order of hours at ambient temperature). For sensing environments with rapidly changing moisture sleeves with a very thin wall should be used.

We conclude that the experimental results have high model fidelity and that the experiments were not perturbed by parasitic effects. The sensor requirements are generally respected, except for the operating temperature range which could not be verified below 13 and above 60 °C due to experimental-technical limitations.

5. Moisture monitoring in construction materials

This chapter demonstrates the potential of the fibre optic short gauge humidity sensor for use within construction materials. For this purpose, two measurement series were carried out.

5.1 Mortar hydration

In this experiment the early desiccation of hydrating mortar was monitored. Its objective was to verify if the relative humidity measurements obtained with the fibre optic sensor agree with the measurement of a conventional electrical RH gauge.

5.1.1 Experimental setup and sensor installation

In order to avoid an influence of the environmental humidity on the hydration process (see 2.2.3), which is difficult to quantify, the mortar was cast in a watertight PVC mould such as to enable endogenous desiccation. The mould was cubic with an internal volume of 1 litre (see Figure 5.1). A special inlet covered with a Teflon filter served for introducing the electrical RH / T gauge (Rotronic Hygroclip, Switzerland) in the core of the mortar. The mould and the RH / T gauge were provided by G. Martinola from the Institute for Building Materials (IBWK) at ETHZ.

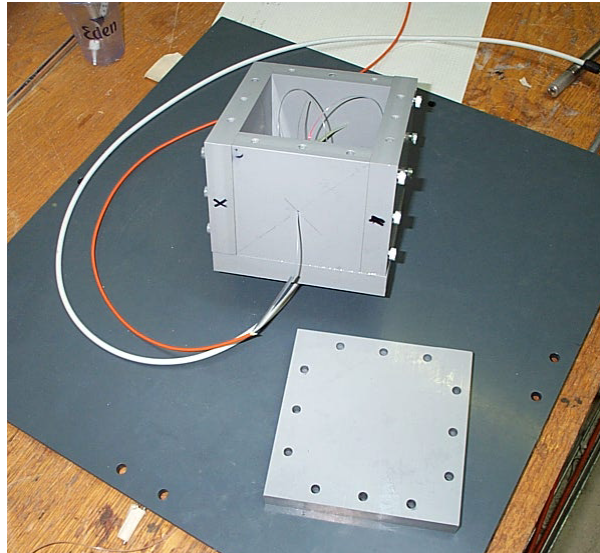


Figure 5.1 PVC mould with cover plate.

In order to have measurement redundancy for the fibre optic sensor, two calibrated recoated FBGs (FBG 3 and FBG 4, see Table 4.2) were spliced together to form a 2-point multiplexed sensor. A PTFE sleeving (wall thickness 0.15 mm) was used as packaging. The packaged sensor is attached to the inlet such that the grating zones are located alongside the inlet, each one on either side (see Figure 5.2). This makes sure that the fibre optic and the electrical sensor are subjected to identical RH and T conditions. A small access hole was drilled in one of the mould faces in order to lead the fibre out of mould.

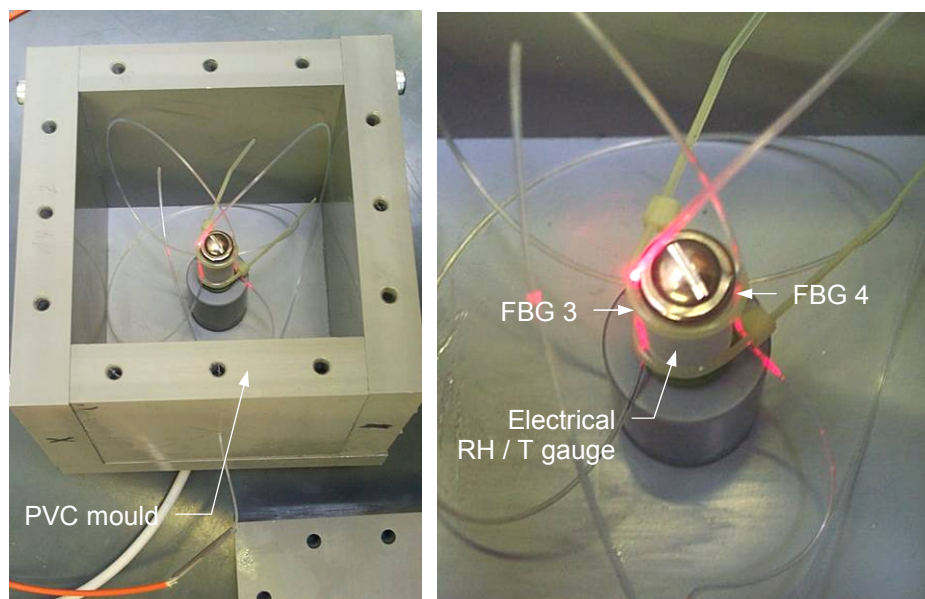


Figure 5.2 Arrangement of the electrical gauge and the fibre optic sensors (FBGs).

The FBG sensors were interrogated with the FBG-IS, while the Rotronic sensor was read with Rotronic's proprietary reading unit. The measurement interval was first 5 min and then 15 min for both measurement systems.

The following mortar mix was used:

- Aggregate 0-4 mm
- Cement CEM II 32.5
- 1% plasticizer
- $w/c = 0.3$

Once all test equipment was installed and started, the mortar was carefully cast into the mould (see Figure 5.3). But despite the care, the optical fibre broke at the splice between the gratings, leaving only FBG 4 operational.



Figure 5.3 Casting of mortar.

5.1.2 Measurements and discussion

Figure 3.7 shows the brute, uncompensated relative Bragg wavelength shift of the FBG sensor for the first 19 days, starting from the time of mortar casting. The fluctuations after the initial rise are due to temperature variations of the mortar.

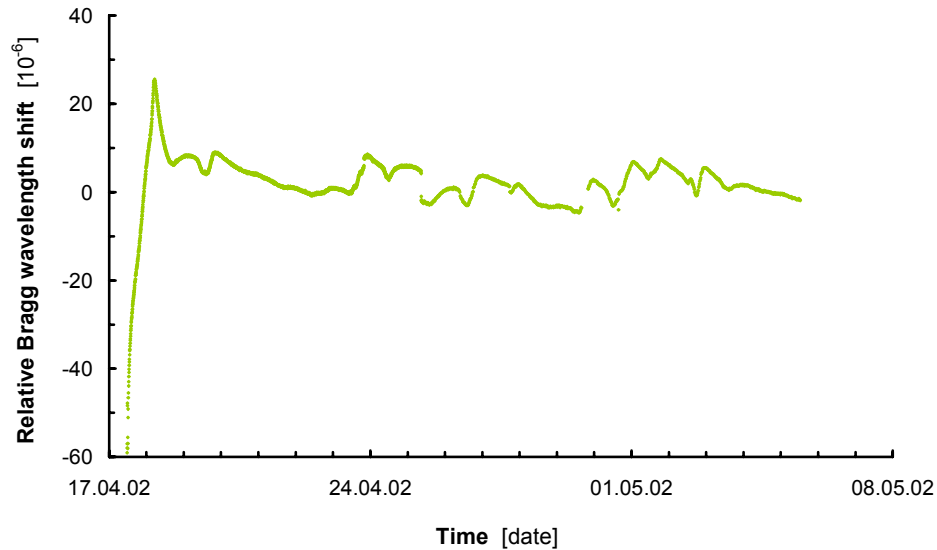


Figure 5.4 FBG sensor response during the first 19 days of the mortar curing process.

Using the calibration coefficients and compensating the thermal effect based on the temperature measurements of the Rotronic gauge, the relative humidity can be retrieved (see Figure 5.5).

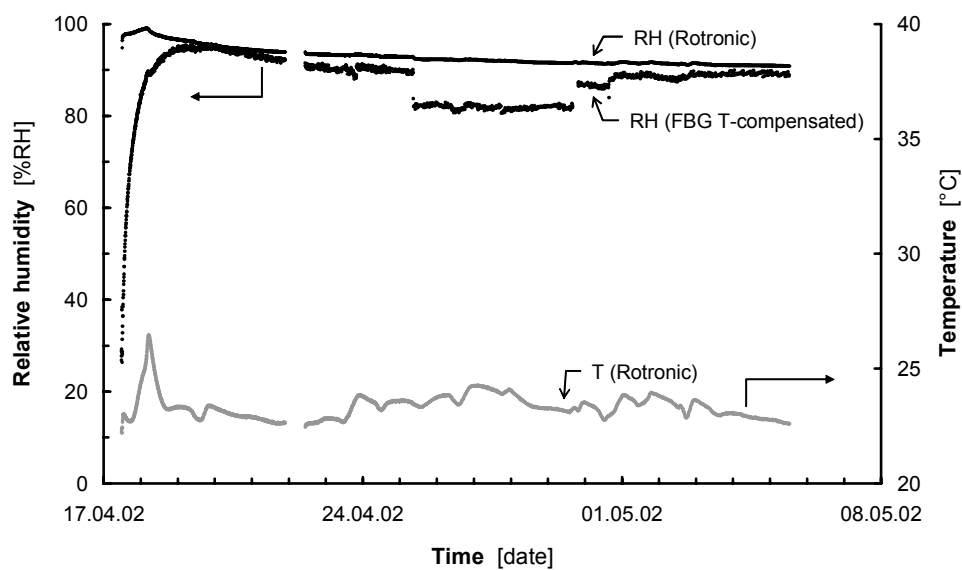


Figure 5.5 Relative humidity and temperature evolution inside the mortar during the first 19 days.

We notice that the FBG response is flattened after having compensated for the T-effect and the retrieved RH values agree well with the measurements of the electrical gauge. The delay of the FBG sensor in the initial phase is due to the sensor packaging ($t_{90} \approx 1$ day at 20 °C, see 4.9). The temporary offset of the FBG response during the second week is probably due to Bragg wavelength demodulation instabilities of the reading unit (the reading unit was switched off and on). Such parasitic phenomena can be minimised by using more stable reading units or by using sensors with thicker coatings which are less sensitive to wavelength demodulation inaccuracies.

With this test we have shown that the embedded FBG sensor seems to respond well to the moistening during casting and to the hydration induced desiccation. The RH values obtained from the FBG sensor response agree with the RH measurements of a conventional electrical gauge.

5.2 Water suction in timber

A second measurement series was carried out to evaluate the potential of the sensor to be used for moisture profile monitoring. For this purpose a suction experiment in timber was conducted, using a 5-point multiplexed FBG sensor to assess the hygroscopic moisture distribution.

5.2.1 Experimental setup and sensor installation

The packaged sensor chain was thread through the parallel holes which were drilled through a timber cuboid, such that the sensitive zones on the fibre (i.e., the gratings) lie each on a different level inside the timber (see Figure 5.6). The sensors were distributed in longitudinal direction, i.e., in direction of the wood fibres. Tiny rubber collars were used to seal the holes around the sensor packaging sleeve. For temperature compensation, 5 thermocouples were introduced into the timber on the same heights as the gratings, but from the adjacent side of the cuboid. In addition, 5 pairs of electrodes were introduced in the timber to measure its resistivity at the monitored positions. As seen in 2.3.2, the electrical resistivity of a porous material can be used to assess the moisture content. Figure 5.7 depicts the entire sensor setup.

After installation of the sensors, the timber piece was put in the climate chamber in order to control the environmental conditions during the experiment. The climate chamber was monitored with the electrical RH / T gauge from Rotronic. The FBG sensor was read with the FBG interrogation system and all electrical sensors (5

thermocouples, 5 pairs of electrodes and the Rotronic RH / T sensor) were interrogated and recorded with a data logger. Measurements were taken every 15 min.

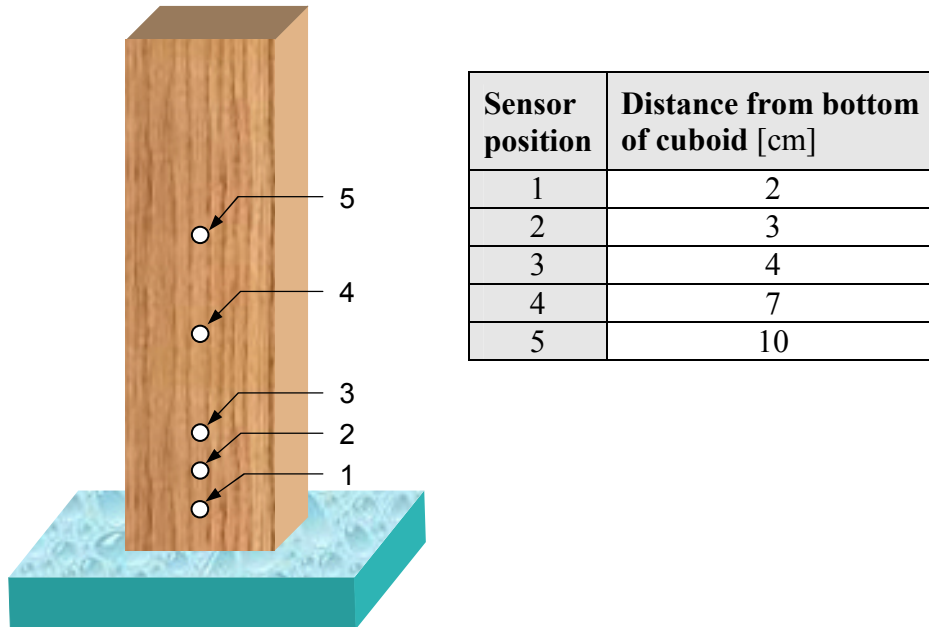


Figure 5.6 Sensor locations.

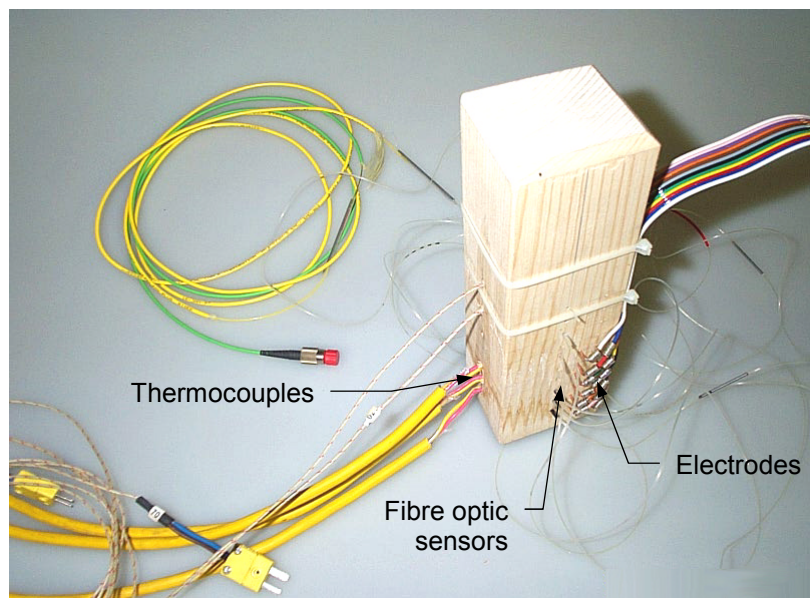


Figure 5.7 Monitoring of timber cuboid.

5.2.2 Measurements and discussion

The experiment was carried out in several different steps. First, the timber was dried at 30 %RH during one day. On day 2, water was added to immerse the cuboid by approximately 1 cm. We note that the cuboid was slightly elevated, leaving the water unhindered access to the bottom face. On days 3 and 4, the relative humidity of the climate chamber was incrementally increased to 64 %RH and 98 %RH respectively, while the timber was left immersed in water. The temperature was kept constant at 40 °C during the whole test cycle. Figure 5.8 shows the RH values obtained from the T-compensated responses of the 5 gratings. On day 1, the sensors at the lower positions (1, 2 and 3) indicate a desiccation. On day 2, when the cuboid is immersed, the sensor at position 1 responds, indicating a rapid increase of the relative humidity up to nearly 100 %RH due to capillary suction. 100 %RH relative humidity means that the wood fibres are fully saturated. The sensors at positions 2 and 3 also indicate a moistening of the timber, though less significant, reaching only 50 to 55 %RH. Since the sensors at position 4 and 5 do not respond, we may conclude that the capillary suction stops in between position 3 and 4. This agrees with the visual observation of darkened wet wood reaching up to just above sensor position 3. On the day 3 and 4, only the sensors laying in the not fully saturated part of the timber respond. However, we doubt that this response is a consequence of a vapour absorption induced moistening of the timber. It is more likely that humid air has penetrated the sensor cavities and locally increased the relative humidity. Another test with different and better sealing (e.g., silicone gel) should be performed to clarify this point.

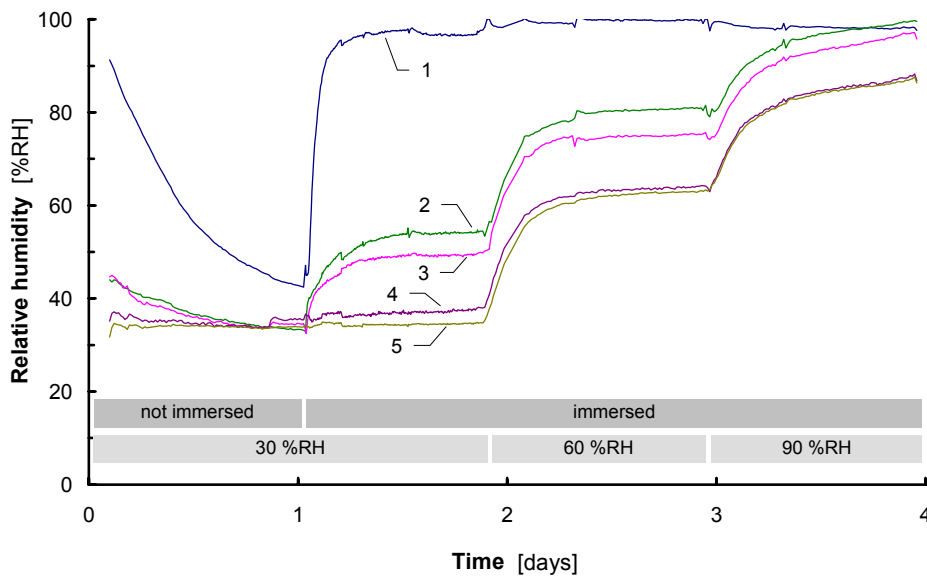


Figure 5.8 Relative humidity values obtained from the T-compensated FBG sensor responses to capillary suction and variations in ambient relative humidity.

Unfortunately, the electrodes became polarised (negative resistance!) and therefore the resistivity measurements could not be used for comparison. A qualitative comparison with the temperature values of the embedded thermocouples nevertheless confirmed the consistency of the fibre optic measurements (the thermocouple in a moist host behaves in some way similarly to the wet-bulb temperature gauge of a psychrometer, i.e., the higher the humidity of the host material in comparison to the ambient humidity is, the lower is its temperature).

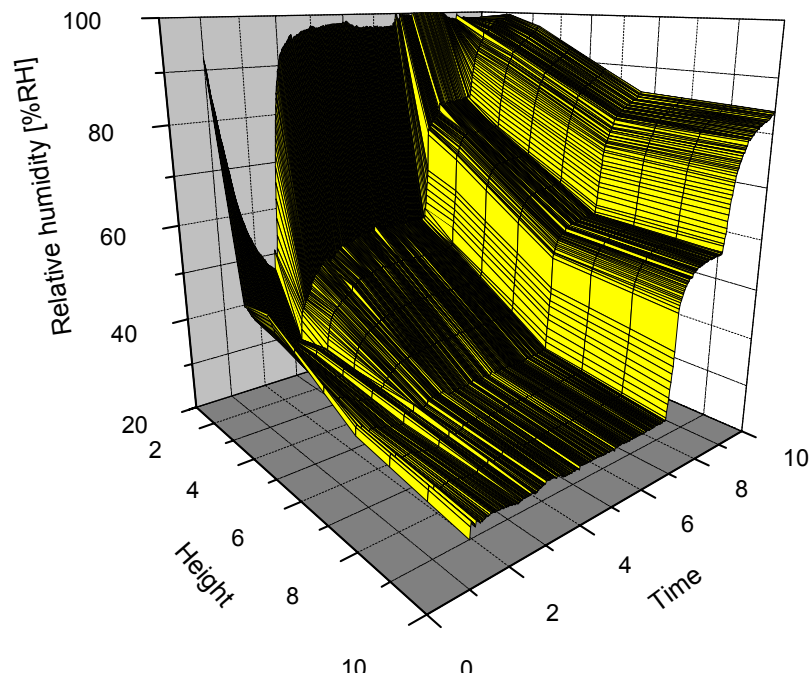


Figure 5.9 Surface plot visualising the time evolution of the relative humidity profile throughout the timber cuboid. Intermediate RH values between sensor positions 3 and 4, and 4 and 5 are estimated by linear interpolation. The height and time scales are arbitrary.

5.3 Concluding remarks

When embedded, the fibre optic sensor retains its sensing capability. This has been verified for cement and timber. Profile moisture monitoring can be performed by using a point multiplexed FBG sensor chain.

6. Future work

6.1 Sensor

The linear model describing the temperature dependence of the sensor response is valid at temperatures between 13 and 60 °C. However, for temperatures below or above this range, non-linear effects may occur. These could be due to

- Temperature dependent fibre and coating material properties and
- Temperature dependent vapour sorption behaviour of polyimide.

Since temperatures in in-situ civil engineering applications may easily drop below 13 °C, further investigations of this point would be useful. On the other hand, if the sensor is intended to be used in high temperature laboratory experiments, a better understanding of the sensor behaviour at temperatures exceeding 60 °C is required. Tests at temperatures below the freezing and above the boiling point (-20 to 160 °C) have already shown that the sensor withstands these temperatures without being damaged.

In order to perform these investigations, a climate chamber with a low dew point (for RH control at low temperatures) and a pressure chamber with pressure control (for experiments above 100 °C) would be required.

Sensors for monitoring applications in civil engineering require having a stable response behaviour over many years and even in harsh environments. Silica, i.e., the fibre material, is known to be very durable and inert to most chemical attacks. Polyimide coatings on the other side have shown signs of degradation after being exposed over several months to an alkaline environment [75]. Even if the sensor proposed in this work survives well in a neutral environment, its durability in chemically aggressive environments requires further study.

We have mentioned that the bare fibre in the SOFO sensor is not an ideal choice because its fragility and its temperature sensitivity are such that full temperature compensation is only possible for very short gauge lengths. The use of metal coated fibres would be an alternative that merits evaluation. Table 6.1 lists a selection of metals coatings and their approximate thicknesses required such that the temperature sensitivity of the metal coated fibre is similar to the one of the polyimide coated fibre

used in this work. A market survey may help determining if the specified coatings are available at the suggested thickness.

Coating material	Thermal expansion coefficient, α_c [10^{-6} K^{-1}]	Young's modulus, E_c [GPa]	Coating thickness [μm]
Polyimide	74	2.45	14
Magnesium	8.2	45	8.9
Gold	14.2	78	2.8
Silver	18.9	83	1.9
Copper	16.5	130	1.4
Zinc	35	108	0.8

Table 6.1 Selection of metal coatings and their equivalent thicknesses.

6.2 Packaging

We have mentioned that the PTFE sensor packaging delays the sensor response substantially. Investigations on alternative packaging forms which are more vapour permeable are required if the sensor is used in an environment in which humidity changes rapidly, or at low temperatures.

During the material measurement experiments, an offset of the sensor response from the values, which were obtained during calibration, has in some cases been observed. As the calibration was in general performed with the unpackaged sensor, this offset may be due to parasitic strains induced into the fibre due to friction with the packaging. Further investigation into the fibre-packaging interaction may clarify this issue.

6.3 Applications

The most important future task is to use the sensor for full-scale monitoring applications in construction materials. In a first step, materials should be tested in laboratory conditions, while in a second stage, in-situ applications should be carried out. The feedback gained from these applications will help resolve remaining weaknesses and could improve the sensor in terms of sensitivity, temperature compensation, response time and stability. Such efforts would lead to a reliable and

versatile sensing tool for non-destructive and minimally invasive in-depth moisture monitoring of construction materials.

7. Conclusions

The successful development and testing of a short and of a long gauge fibre optic humidity sensor based on absorption hygrometry leads to the following principal conclusions:

- The proposed fibre optic sensors generally satisfy the set of requirements. They are thus suitable to be applied to non-destructive in-depth moisture monitoring of construction materials.
- The high model fidelity of the experimental results in the controlled environment confirms the aptness of the proposed models to describe accurately the sensor behaviour.
- Humidity measurements in construction material samples indicate that the sensor is able to monitor accurately the humidity evolution when embedded. Measurements with a point multiplexed fibre Bragg grating sensor chain have demonstrated that the sensor can be applied to assess moisture profiles.

In addition, the following secondary conclusions emerged from this work:

- The 1-D and 3-D models which are used to describe the mechanical behaviour of the coated fibre show a significant discrepancy. For an accurate description of the fibre deformation the 3-D model should thus be used.
- The theoretical sensor response time depends significantly on whether a plane layer or a tubular layer diffusion model is used. The appropriate layer geometry for the fibre coating is the tubular one.
- The RH- and T-sensitivities and response times of FBG sensors can be adapted by varying the recoating thickness. The ideal recoating thickness depends on the intended application.
- All-fibre temperature compensation works well. The SOFO humidity sensor exhibits low temperature cross-sensitivity because it is able to auto-compensate temperature effects.
- The sensors being based on fibre optic sensor techniques that are already established in structural monitoring, multi-point and multi-parameter (strain, pressure, temperature and moisture) sensor networks may readily be implemented.

References

- [1] Smith IFC, The impact of new measurement systems on structural engineering, Trends in Optical Non-Destructive Testing and Inspection (P. Rastogi and D. Inaudi, eds.), 2000, 1-14.
- [2] Culshaw B, Michie C, Gardiner P, McGown A, Smart Structures and Applications in Civil Engineering, Proceeding IEEE, 84 (1) (1996), 78-86.
- [3] Nilsson L-O, Hygroscopic moisture in concrete – drying, measurement & related material properties, Lund Institute of Technology, Report TVBM-1003 (1980).
- [4] Hunkeler F, Grundlagen der Korrosion und der Potentialmessung bei Stahlbetonbauten, EVED/ASB, VSS Bericht Nr. 510 (1994).
- [5] Yan RL, Hilsdorf HK, Kesler, Effect of temperature on the drying of concrete, University of Illinois, Urbana, TAM report no. 316 (1986).
- [6] Sørensen EV, Radjy F, Permeability of hardened cement paste in relation to pore structure, Aalborg Portland, Karlstrup, internal report (1976).
- [7] Bray WH, Diffusion of water in hardened Portland cement paste, University of Stanford, Tech. report no. 112 (1996).
- [8] Saouma VE, Numerical simulation of concrete deterioration: A multi-physics approach.
- [9] Parrot LJ, Moisture profiles in drying concrete, Advances in Cement Research, 1 (3) (1988), 164-170.
- [10] Patel RG, Killoh DC, Parrott LJ, Gutteridge WA, Influence of curing at different relative humidities upon compound reactions and porosity in Portland cement paste, Materials and Structures, 21 (1988), 192-197.
- [11] Powers TC, A discussion of cement hydration in relation to the curing of concrete, Highway research board (1947).
- [12] Verbeck G, Carbonation of Hydrated Portland Cement, Cement and Concrete, American Society for Testing and Materials, 205 (1958), 17-36.
- [13] Newman K, Common quality in concrete construction, Concrete International, American Concrete Institute, Detroit (1986), 37-49.
- [14] Schiessl P (ed.), Corrosion of steel in concrete, RILEM report, Technical Committee 60-CSC, Chapman & Hall, London, 1988.
- [15] Krogh H, Examination of the water absorption and the viscosity of synthetic alkali-silica gels, Proceedings of Nordic Concrete Research Meeting, Aarhus (1974).
- [16] Götz K-H, Hoor D, Möhler K, Natterer J, Construire en bois, Presses Polytechniques Romandes (1983).
- [17] Leschnik W, Feuchtemessung an Baustoffen – Zwischen Klassik und Moderne, DGZfP-Berichtsband BB 69 (H2), 1999.

- [18] Kaspar I, Feuchtigkeitsmessung von Baumaterialien, Wissenschaftliche Zeitschrift der Technischen Universität Dresden, 27 (2) (1978), 467-470.
- [19] Kupfer C, Materialfeuchtemessung. Beiträge zahlreicher Autoren, Expert-Verlag, 1997.
- [20] Parrott LJ, Measurement of air permeability and relative humidity in cover concrete, British Cement Association (1991).
- [21] Basheer PAM, Nolan E, Near-surface moisture gradients and in-situ permeation tests, Proceedings on technical session "Near-surface Testing for Strength and Durability of Concrete", 5th CANMET/ACI International Conference on Durability of Concrete, Barcelona 2000.
- [22] Paroll H, Measurement of Relative Humidity and Temperature in new Concrete Bridges, VTT Symposium 174 (1997).
- [23] McCarter WJ, Near-Surface Sensors for Condition Monitoring of Cover-Zone Concrete, Proceedings on technical session "Near-surface Testing for Strength and Durability of Concrete", 5th CANMET/ACI International Conference on Durability of Concrete, Barcelona 2000.
- [24] Electrochemical Techniques for Monitoring the Conditions of Concrete Bridge Structures, Schiegg, Elsener and Böhni, IBWK / ETHZ, Switzerland.
- [25] Raupach M, Weydert R, Bestimmung der Feuchteverteilung in Betonböden mit Einbausensoren, 4. Int. Kolloquium Industrieböden '99, Technische Akademie Esslingen / Stuttgart, Tagungsband (P. Seidler, ed.), vol. II, 1999, 605-609.
- [26] Watson A, Measurement of moisture content in some structures and materials by microwave absorption, RILEM/CIB Symposium on moisture problems in buildings, Helsinki, SF 1965, paper 6-8.
- [27] Rudolph M, Schaurich D, Wiggenhauser H, Feuchteprofilmessungen mit Mikrowellen an Mauerwerk, Feuchtetag '93, Berlin, DGZfP-Berichtsband 40, 1993, 44-56.
- [28] Boekwijt WO, Diagnoseverfahren bei der Feuchtigkeitsbekämpfung, Bautenschutz + Bausanierung, 2 (2) (1979), 48-51.
- [29] Schwarz W, Venzmer H, Neue Möglichkeiten und Grenzen der zerstörungsfreien Ultraschallfeuchtemessung an Werkstoffen der Mauerwerks, International Journal for Restoration of Buildings and Monuments, 1 (1) (1995), 21-36.
- [30] Kober A, Mehlhorn L, Radiometrische Feuchtemessung in Bauteilen mit hoher räumlicher Auflösung, Bauphysik, 13 (2) (1991), 43-49.
- [31] McCarter WJ, Watson DW, Chrisp TM, Surface Zone Concrete: Drying, Absorption, and Moisture Distribution, Journal of Materials in Civil Engineering, 13 (1) (2001), 49-57.
- [32] Culshaw B, Smart Structures and Materials, Artech House, 1996.
- [33] Udd E (ed.), Fiber Optic Smart Structures, Wiley Interscience, 1995.
- [34] Michie WC, Thursby G, Johnstone W, Culshaw B, Optical Techniques for Determination of the State of Cure of Epoxy-Resin-Based Systems, SPIE 1798 (1992).

- [35] Lecot C, Lequime M, Vanotti P, Lang D, Windisch A, Davidson R, Turpin M, Chazelas J, Culshaw B, Michie C, Papadopoulos P, An Introduction to the BRITE-EURAM II Osmos Project, SPIE 2075B-43 (1993).
- [36] Culshaw B, Dakin J (eds.), Optical Fiber Sensors: Components and Subsystems, vol. 3, Artech House, 1996.
- [37] Measures RM, Structural Monitoring with Fiber Optic Technology, Academic Press, 2001.
- [38] Hocker GB, Fiber-optic sensing of pressure and temperature, Applied Optics, 18 (9) (1979), 1445-1448.
- [39] Jackson DA, Jones, Interferometers, Optical Fiber Sensors: Systems and Applications, vol. 2 (B. Culshaw and J. Dakin, eds.), Artech House, 1989, 329-380.
- [40] Lee CE, Taylor HF, Interferometer Fiber Optic Sensors using Internal Mirrors, Electronics Letters, 24 (1988), 193-194.
- [41] Morey WW, Meltz G, Glenn WH, Fiber optic Bragg gratings sensors, SPIE 1169 (1989), 98-107.
- [42] Horigushi T, Kurashima T, Tadedo M, A technique to measure distributed strain in optical fibers, IEEE Photonic Technology Letters (2) (1990), 352.
- [43] Inaudi D, Vurpillot S, Casanova N, Bridge Monitoring by Interferometric Deformation Sensors, Laser Optoelectronics and Microphotonics: Fiber Optics Sensors, SPIE, Beijing (1996).
- [44] Habel WR, Hillemeier B, Results in monitoring and assessment of damages in large steel and concrete structures by means of fiber optic sensors, Smart Structures and Materials, SPIE 2446 (1995), 25-36.
- [45] Kersey AD, Davis MA, Patrick HJ, LeBlanc M, Koo KP, Askins CG, Putnam MA, Friebele EJ, Fiber Grating Sensors, Journal of Lightwave Technology, 15 (8) (1997), 1442-1463.
- [46] Alavie AT, Karr SE, Othonos A, Measures RM, A multiplexed Bragg grating fiber laser system, IEEE Photonics Technology Letters, 5 (1993), 1112-1114.
- [47] Maaskant R, Alavie AT, Measures RM, A recent experience in bridge strain monitoring with fibre grating sensors, Fibre Optic Sensors for Constructional Materials and Bridges (F. Ansari, ed.), 1998.
- [48] Thévenaz L, Distributed deformation sensors, Trends in Optical non-destructive testing and inspection, ed. P. Rastogi and D. Inaudi, Elsevier (2000).
- [49] Russell AP, Fletcher KS, Optical sensor for the determination of moisture, Analytica Chimica Acta, 170 (1985), 209-216.
- [50] Shahriari MR, Sigel GH, Zhou Q, Porous Fibre Optic for a High Sensitivity Humidity Sensor, Digest on Optical Fiber Sensors, OSA, Washington D.C. (1988), 373-381.
- [51] Kharaz A, Jones BE, A distributed optical-fibre sensing system for multiplexed humidity measurement, Sensors and Actuators A 46-47 (1995), 491-496.

- [52] Zhu C, Bright FV, Wyatt WA, Hieftje GM, A New Fluorescence Sensor for Quantification of Atmospheric Humidity, *Journal of the Electrochemical Society*, 136 (2) (1989), 567-570.
- [53] Stuart AD, Grazier PE, A fibre-optic relative humidity sensor, *International Journal of Optoelectronics*, 3 (2) (1988), 177-186.
- [54] Mitschke F, Fiber-optic sensor for humidity, *Optics Letters*, 14 (17) (1989), 967-969.
- [55] Arregui FJ, Liu Y, Matias IR, Claus RO, Optical fiber humidity sensor using a nano Fabry-Perot cavity formed by the ionic self-assembly method, *Sensors and Actuators B*, 59 (1999), 54-59.
- [56] Bariáin C, Matías IR, Arregui FJ, López-Amo M, Optical fiber humidity sensor based on a tapered fiber coated with agarose gel, *Sensors and Actuators B*, 69 (2000), 127-131.
- [57] McMurtry S, Wright JD, Jackson DA, A multiplexed low coherence interferometric system for humidity sensing, *Sensors and Actuators B*, 67 (2000), 52-56.
- [58] Michie WC, Culshaw B, Konstantaki M, McKenzie I, Kelly S, Graham NB, Moran C, Distributed pH and water detection using fiber-optic sensors and hydrogels, *Journal of Lightwave Technology*, 13 (7) (1995), 1415-1420.
- [59] Michie WC, Culshaw B, McLean A, Konstantaki M, Hadjiloucas S, Distributed Water Ingress and Water Potential Measurements using Fibre Optics, *Cement and Concrete Composites*, 19 (1997), 35-44.
- [60] Kronenberg P, Culshaw B, Pierce G, Development of a novel fibre optic sensor for humidity monitoring, *Smart Structures and Materials*, SPIE 3670 (66) (1999), Newport Beach.
- [61] Frocht MM, *Photoelasticity*, Wiley, 1948.
- [62] Takahashi S, Shibata S, Thermal Variation of Attenuation for Optical Fibers, *Journal of Non-Crystalline Solids*, 30 (1979), 359-370.
- [63] Yariv A, Yeh P, *Optical waves in crystals*, John Wiley & Sons, New York, 1984.
- [64] Alavie AT, Maaskant R, Stubbe R, Othonos A, Ohn M, Sahlgren B, Measures RM, Characteristics of fiber grating sensors and their relation to manufacturing techniques, *SPIE 2444* (1995), 528-535.
- [65] Sacher E, Susko JR, Water Permeation of Polymer Films. III. High-Temperature Polyimides, *Journal of Applied Polymer Science*, 26 (1981), 679-686.
- [66] Timoshenko SP, *Strength of Materials*, 3rd edn. (1958), Krieger Publishing Company, New York.
- [67] Mallinder FP, Proctor BA, Elastic constants of fused silica as a function of large tensile strain, *Physics of Chemistry of Glasses*, 5 (4) (1964), 91-103.
- [68] Pyralin Product Information, HD Microsystems (2001).

-
- [69] Sager K, Schroth A, Nakladal A, Gerlach, G, Humidity-dependent mechanical properties of polyimide films and their use for IC-compatible humidity sensors, *Sensors and Actuators A*, 53 (1996), 330-334.
- [70] Crank J, *The mathematics of diffusion*, Oxford Univ. Press, London (1970).
- [71] Coumans JW, *Power-law diffusion in drying processes*, Ph.D. Thesis, Technical University of Eindhoven, The Netherlands, 1987.
- [72] Vergnaud JM, *Liquid Transport Processes in Polymeric Materials, Modelling and industrial applications*, Prentice-Hall, New York (1991).
- [73] Mrotek JL, Matthewson MJ, Kurkjian CR, Diffusion of Moisture Through Optical Fibre Coatings, *Journal of Lightwave Technology*, 19 (7) (2001), 988-993.
- [74] Kashyap R, *Fiber Bragg Gratings*, Academic Press, 1st edition (1999).
- [75] Habel WR, Schulz E, Hillemeier B, Bismarck A, Springer J, How to achieve the desired strain transfer to measure microdeformation in cementitious building materials at early ages by using fibre-optic sensors? (Poster).
- [76] Morey WW, Dunphy JR, Meltz G, Multiplexing fibre bragg grating sensors, *SPIE 1586* (1991), 216-224.
- [77] Inaudi D, *Fiber Optic Sensor Network for the Monitoring of Civil Engineering Structures*, Thesis 1612 (1997), EPFL Switzerland.
- [78] Kronenberg P, Rastogi PK, Giaccari Ph, Limberger HG, Relative humidity sensor with optical fiber Bragg gratings, *Optics Letters*, 27 (16) (2002), 1385-1387.
- [79] Schlotter NE, Diffusion of small molecules in glassy polymer thin films studied by waveguide Raman techniques, *Journal of Physical Chemistry*, 94 (1992), 1692-1699.
- [80] Smartec SA, Switzerland (www.smartec.ch).

Annexe

The analytical expressions of α_{cf} , $C_{1,f}$, $C_{2,f}$, $C_{1,c}$ and $C_{2,c}$ in the 3-D model presented in 3.3.2.2 are

$$\alpha_{cf} = \frac{\alpha_f E_f a^2 + \alpha_c E_c (b^2 - a^2)}{E_f a^2 + E_c (b^2 - a^2)} \dots$$

$$\frac{+\nu_f^2 E_c^2 \alpha_c (a^2 - b^2)^2 F + \nu_c^2 E_f^2 \alpha_f a^4 F + \nu_f \nu_c E_f E_c (\alpha_f + \alpha_c) (a^2 b^2 - a^4) F}{+\nu_f^2 E_c^2 (a^2 - b^2)^2 F + \nu_c^2 E_f^2 a^4 F + \nu_f \nu_c E_f E_c 2(a^2 b^2 - a^4) F} \dots$$

$$\frac{+\nu_f E_c \left(\left(\frac{1}{2} \alpha_c E_c + \frac{1}{2} \alpha_f E_f - \alpha_c E_f \right) a^4 + \left(\left(\alpha_c - \frac{1}{2} \alpha_f \right) E_f - \alpha_c E_c \right) a^2 b^2 + \frac{1}{2} \alpha_c E_c b^4 \right) F}{+\nu_f E_c \left(\frac{1}{2} (E_c - E_f) a^4 + \left(\frac{1}{2} E_f - E_c \right) a^2 b^2 + \frac{1}{2} E_c b^4 \right) F} \dots$$

$$\frac{+\nu_c E_f \left(\left(\frac{1}{2} \alpha_f E_f + \frac{1}{2} \alpha_c E_c - \alpha_f E_c \right) a^4 + \alpha_f \left(E_c - \frac{1}{2} E_f \right) a^2 b^2 - \frac{1}{2} \alpha_c E_c b^4 \right) F}{+\nu_c E_f \left(\frac{1}{2} (E_f - E_c) a^4 + \left(E_c - \frac{1}{2} E_f \right) a^2 b^2 - \frac{1}{2} E_c b^4 \right) F}$$

where $F = \frac{2}{E_c (a^2 - b^2) - E_f (a^2 + b^2)}$

$$C_{1,f} = \frac{\alpha_f (1 + \nu_c) \left(\left(\nu_c - \frac{1}{2} \right) a^2 - \frac{1}{2} b^2 \right) a^2 E_f^2}{(1 + \nu_c) \left(\left(\nu_c - \frac{1}{2} \right) a^2 - \frac{1}{2} b^2 \right) a^2 E_f^2} \dots$$

$$\frac{-E_c E_f (a^2 - b^2) \left(\left(\left(\alpha_c + \alpha_f \right) \nu_c - \frac{1}{2} \alpha_f + \alpha_c \right) \nu_f + \left(\alpha_f - \frac{1}{2} \alpha_c \right) \nu_c \right)}{-2E_c E_f (a^2 - b^2) \left(\left(\left(\frac{1}{4} + \nu_c \right) \nu_f + \frac{1}{4} \nu_c - \frac{1}{2} \right) a^2 \right)} \dots$$

$$\frac{-\frac{1}{2} \alpha_c - \frac{1}{2} \alpha_f \left) a^2 \frac{1}{2} (1 + \nu_c) b^2 \left(\left(\alpha_f - \alpha_c \right) \nu_f + \alpha_f \right) \right)}{-\frac{1}{4} b^2 (1 + \nu_c)} \dots$$

$$\frac{+\alpha_c (1 + \nu_f) \left(\nu_f - \frac{1}{2} \right) (a + b)^2 E_c^2 (a - b)^2}{+(1 + \nu_f) \left(\nu_f - \frac{1}{2} \right) (a + b)^2 E_c^2 (a - b)^2}$$

$$C_{2,f} = 0$$

$$\begin{aligned}
C_{1,c} &= \frac{\left((1+\nu_c)E_f + (-1-\nu_f)E_c\right)\left(\left(\nu_c - \frac{1}{2}\right)\alpha_f E_f - \left(\nu_f - \frac{1}{2}\right)\alpha_c E_c\right)a^4}{\left((1+\nu_c)E_f + (-1-\nu_f)E_c\right)\left(\left(\nu_c - \frac{1}{2}\right)E_f + \left(-\nu_f + \frac{1}{2}\right)E_c\right)a^4} \dots \\
&+ \frac{\frac{1}{2}\left((1+\nu_c)\left((\alpha_f - \alpha_c)\nu_c - \alpha_c\right)E_f^2 + 2\left(\left(\alpha_c + \alpha_f\right)\nu_c - \frac{1}{2}\alpha_f + \alpha_c\right)\nu_f\right)}{-\frac{1}{2}b^2\left(\left(1+\nu_c\right)E_f^2 - 4\left(\frac{1}{4} + \nu_c\right)\nu_f - \frac{1}{4} + \frac{1}{2}\nu_c\right)E_c E_f} \dots \\
&+ \frac{\left(\nu_c - \frac{1}{2}\right)\alpha_f E_c E_f - 4\left(\nu_f - \frac{1}{2}\right)\left(1+\nu_f\right)\alpha_c E_c^2 b^2 a^2}{+4\left(\nu_f - \frac{1}{2}\right)\left(1+\nu_f\right)E_c^2 a^2} \dots \\
&\frac{-\frac{1}{2}\alpha_c E_c \left(\left(1+\nu_c\right)E_f + \left(-\nu_f - 2\nu_f^2 + 1\right)E_c\right)b^4}{-\frac{1}{2}E_c \left(\left(1+\nu_c\right)E_f + \left(-\nu_f - 2\nu_f^2 + 1\right)E_c\right)b^4} \\
C_{2,c} &= \frac{\frac{1}{2}\left(\alpha_c - \alpha_f\right)\left(\left(-\nu_f E_c + \nu_c E_f - E_c + E_f\right)a^2 + b^2 E_c \left(1+\nu_f\right)\right)a^2 E_f b^2 \left(1+\nu_c\right)}{\left(\left(-\nu_c + \frac{1}{2}\right)E_f + E_c \left(\nu_f - \frac{1}{2}\right)\right)\left(\left(-1-\nu_c\right)E_f + E_c \left(1+\nu_f\right)\right)a^4} \dots \\
&\frac{-2\left(\left(-\frac{1}{2} + \nu_f^2 + \frac{1}{2}\nu_f\right)E_c^2 - \left(\frac{1}{4} + \nu_c\right)\nu_f - \frac{1}{4} + \frac{1}{2}\nu_c\right)E_c E_f + \frac{1}{4}E_f^2 \left(1+\nu_c\right)}{+\left(\left(-\frac{1}{2} + \nu_f^2 + \frac{1}{2}\nu_f\right)E_c - \frac{1}{2}E_f \left(1+\nu_c\right)\right)E_c b^4} \dots
\end{aligned}$$

Notations

Latin upper case	Description	SI units
A	Cross-section area	$[\text{m}^2]$
C_1, C_2	Integration constants	$[\text{K}^{-1}], [\text{m}^2 \text{K}^{-1}]$
D	Diffusivity	$[\text{m}^2 \text{s}^{-1}]$
D_0	Frequency factor	$[\text{m}^2 \text{s}^{-1}]$
D_0	Coefficient (power-law)	$[\text{m}^5 \text{s}^{-1} \text{mol}^{-1}]$
E	Young's modulus	$[\text{N m}^{-2}]$
E_A	Activation energy	$[\text{J mol}^{-1}]$
L	Fibre length	$[\text{m}]$
L	Layer thickness	$[\text{m}]$
M_t	Accumulated mass of diffusant after time t	$[\text{mol}]$
P	Permeability	$[\text{mol m N}^{-1} \text{s}^{-1}]$
R	Universal gas constant	$[\text{J mol}^{-1} \text{K}^{-1}]$
RH	Relative humidity	$[\%RH]$
S	Solubility	$[\text{mol m}^{-1} \text{N}^{-1}]$
S_{RH}	RH-sensitivity of (coated) fibre	$[\%RH^{-1}]$
S_T	T-sensitivity of (coated) fibre	$[\text{K}^{-1}]$
$S_{RH,FBG}$	RH-sensitivity of FBG sensor	$[\%RH^{-1}]$
$S_{T,FBG}$	T-sensitivity of FBG sensor	$[\text{K}^{-1}]$
$S_{RH,SOFO}$	RH-sensitivity of SOFO sensor	$[\%RH^{-1}]$
$S_{T,SOFO}$	T-sensitivity of SOFO sensor	$[\text{K}^{-1}]$
T	Temperature	$[\text{°C}]$
T_D	Dew point temperature	$[\text{°C}]$
T_g	Glass transition temperature	$[\text{°C}]$
Latin lower case	Description	SI units
a	Fibre outer radius	$[\text{m}]$
b	Coating outer radius	$[\text{m}]$
c	Light speed	$[\text{m s}^{-1}]$
c	Concentration	$[\text{mol m}^{-3}]$
c_0	Initial concentration	$[\text{mol m}^{-3}]$
c_{ext}	Surface concentration	$[\text{mol m}^{-3}]$
k	Stiffness proportion	
n	Index of refraction	
n_g	Group index of refraction	
n_{eff}	Effective index of refraction	
p	Partial vapour pressure	$[\text{N m}^{-2}]$
p_0	Saturation pressure of water	$[\text{N m}^{-2}]$
p_{11}, p_{12}	Coefficients of the strain-optic tensor	
\hat{p}_e	Effective photoelastic coefficient	
r	Radius	$[\text{m}]$
t	Time	$[\text{s}]$
t_{90}	Time to reach 90% saturation	$[\text{s}]$
u	Radial displacement of cylindrical surface	$[\text{m}]$

Greek upper case	Description	SI units
Λ	Period of index modulation (FBG)	[m]

Greek lower case	Description	SI units
α	Thermal expansion coefficient	[K ⁻¹]
β	Hygroscopic expansion coefficient	[%RH ⁻¹]
ε	Strain (elastic)	
ζ_L	Sensor optical path length	[m]
ζ_M	Sensor optical path length unbalance (SOFO)	[m]
λ	Wavelength	[m]
λ_B	Bragg wavelength	[m]
ν	Poisson's ratio	
ξ	Thermo-optic coefficient	[K ⁻¹]
σ	Normal stress	[N m ⁻²]

Subscripts	Description
${}_f$	Fibre
${}_c$	Coating
${}_{cf}$	Coated fibre
${}_z$	Axial
${}_r$	Radial
${}_\theta$	Tangential
${}_l$	Long sensor arm (SOFO)
${}_s$	Short sensor arm (SOFO)

Superscripts	Description
${}^{1-D}$	Based on one-dimensional model
${}^{3-D}$	Based on three-dimensional model
min	Minimum
max	Maximum
${}^-$	

Curriculum Vitae

Pascal Kronenberg
Dipl. Civ. Eng. ETH / SIA

e-mail: pascal.kronenberg@a3.epfl.ch

D.o.B.: 13/12/1971 in Lucerne, Switzerland
Nationality: Swiss

Career summary

1999 – 2002	Doctoral student at IMAC, EPFL
Oct. 1997 – Oct. 1998	Visiting scholar at Optoelectronics Division, EEE, University of Strathclyde, Glasgow, Scotland
April 1996 – Sept. 1997	Research engineer at IMAC, EPFL Student supervisor in structural analysis
July – Sept. 1994	Internship at Van Wyk & Louw Inc., Consulting Engineers, Durban, South Africa
1991 – 1996	Studies in Civil Engineering at the Swiss Federal Institute of Technology, Lausanne (EPFL)

Distinctions

- **AEA Technology Award** for research work in experimental mechanics (1998).
- **ZSCHOKKE Award** for a multidisciplinary diploma work aiming optimisation (1996).

Commissions

- Member of the EU network for Applications of Smart Structures in Engineering and Technology (ASSET).

Publications

Peer reviewed journal papers

- P. Kronenberg, P.K. Rastogi, Ph. Giaccari, H.G. Limberger; Relative humidity sensor with optical fiber Bragg gratings; Optics Letters 27 (16) (2002), 1385-1387.

- D. Inaudi, N. Casanova, S. Vurpillot, B. Glisic, P. Kronenberg, S. LLoret; Lessons Learned in the Use of Fiber Optic Sensor for Civil Structural Monitoring; *International Journal for Restoration of Buildings and Monuments* 7 (2001), 301.
- D. Inaudi, S. Vurpillot, N. Casanova, P. Kronenberg; Structural monitoring by curvature analysis using interferometric fiber optic sensors; *Smart Materials and Structures* 7 (2) (1998), 199-208.

Journal papers

- P. Kronenberg, N. Casanova; Sofo: Bauwerksüberwachung mit Glasfaser-sensoren; *Schweizer Ingenieur und Architekt* 47 (1997).

Peer reviewed conference papers

- P. Kronenberg, D. Inaudi, P.K. Rastogi; Fiber Optic Relative Humidity Sensors for Structural Monitoring; 3rd World Conference on Structural Control, Como (I), April 2002.
- Ph. Giaccari, H.G. Limberger, P. Kronenberg; Influence of humidity and temperature on polyimide-coated fiber Bragg gratings; *OSA / BGPP, Stresa (I), 2001, BFB2.*
- B. Glisic, D. Inaudi, P. Kronenberg, S. Vurpillot; Dam monitoring using long SOFO sensor; *Hydropower Conference, Aqua Media International, Gmunden (A), Oct. 1999, 709-717.*

Conference papers

- S. Vurpillot, P. Kronenberg, D. Inaudi; Bridge Spatial Displacement Monitoring with Fiber Optic Deformations Sensors; *ACI / KCI 2000 International Conference – Repair, Rehabilitation and Maintenance of Concrete Structures, and Innovations in Design and Construction, Seoul, Korea, Sept. 2000, SP193-54.*
- P. Kronenberg, D. Inaudi, I.F.C. Smith; Development of an „optical hair“-hygrometer: A novel way to measure humidity using fibre optics; *International Conference on Trends in Optical Nondestructive Testing, Lugano (CH), May 2000.*
- D. Inaudi, N. Casanova, S. Vurpillot, B. Glisic, P. Kronenberg, S. LLoret; Deformation monitoring during bridge refurbishment under traffic; *16th IABSE Congress, Lucerne (CH), 2000.*
- S. LLoret, D. Inaudi, B. Glisic, P. Kronenberg, S. Vurpillot; Optical set-up development for the monitoring of structural dynamic behavior using SOFO sensors; *Smart Structures and Materials Conference, SPIE, Newport Beach (US), 2000, Vol. 3986, 199-205.*
- D. Inaudi, P. Kronenberg, S. Vurpillot, B. Glisic, S. LLoret; Long-term monitoring of a concrete bridge with 100+ fiber optic long-gage sensors; *Nondestructive Evaluation of Bridges and Highways III, SPIE, Newport Beach (US), 1999, Vol. 3587, 50-59.*

- B. Glisic, D. Inaudi, P. Kronenberg, S. Lloret, S. Vurpillot; Special sensors for deformation measurements of different construction materials and structures; 6th International Symposium on Smart Structures and Materials, SPIE, Newport Beach (US), 1999, Vol. 3670, 505-513.
- P. Kronenberg, B. Culshaw, G. Pierce; Development of a novel fiber optic sensor for humidity monitoring; Smart Structures and Materials Conference, SPIE, Newport Beach (US), 1999, Vol. 3670, 480-485.
- D. Inaudi, N. Casanova, S. Vurpillot, P. Kronenberg; Structural Analysis of Bridges and Beams Using Long-gage Fiber Optic Sensors; International conference on applied optical metrology, SPIE, Balatonfüred, 1998, Vol. 3407, 382-385.
- D. Inaudi, N. Casanova, P. Kronenberg, S. Vurpillot; SOFO: Monitoring of Concrete Structures with Fiber Optic Sensors; 5th Int. Workshop on Material Properties and Design, Weimar, October 1998, Aedificatio Publishers, 495–514.
- D. Inaudi, J. Conte, S. Vurpillot, P. Kronenberg, S. Lloret; Statistical analysis of under-sampled dynamic displacement measurement; Smart Structures and Materials Conference, SPIE, San Diego (US), 1998, Vol. 3325, 105-110.
- D. Inaudi, N. Casanova, P. Kronenberg, S. Marazzi, S. Vurpillot; Embedded and surface mounted fiber optic sensors for civil structural monitoring; Smart Structures and Materials Conference, SPIE, San Diego (US), 1997, Vol. 3044, 236-243.
- D. Inaudi, N. Casanova, P. Kronenberg, S. Vurpillot; Railway bridge monitoring during construction and sliding; Smart Structures and Materials Conference, SPIE, San Diego (US), 1997, Vol. 3043, 58-64.
- S. Vurpillot, N. Casanova, D. Inaudi, P. Kronenberg; Bridge spatial displacement monitoring with 100 fiber optic sensors deformations – sensors network and preliminary results; Smart Structures and Materials Conference, SPIE, San Diego (US), 1997, Vol. 3043, 51-57.
- P. Kronenberg, N. Casanova, D. Inaudi, S. Vurpillot; Dam monitoring with fiber optics deformation sensors; Smart Structures and Materials Conference, SPIE, San Diego (US), 1997, Vol. 3043, 2-11.

Project reports

- S. Vurpillot, L. Pflug, P. Kronenberg ; Pont sur la Versoix - N1 - autoroute du Léman, Equipement de l'ouvrage en capteurs à fibre optiques; IMAC-DGC-EPFL, 24 novembre 1997, ISS-IMAC IM-01-1997-FO-SV 001, 25.11.1997, 1-22 + appendix 1-6.
- B. Glisic, P. Kronenberg, D. Inaudi; Long sensor: Installation of two SOFO long sensors in "Emosson" dam; IMAC-DGC-EPFL, January (September) 1999, 1-11 + appendix 1-6.

Research proposals

- CTI project: Development of a sensor for monitoring of chloride contamination of reinforced concrete using fibre optics; CTI Project-No. 5105.1, November 2000.